

1           20170727: DARK MATTER SEARCH AND ELECTRON BACKGROUND  
2                                 EVALUATION  
3                                 TESTING OF TPC GRID DESIGNING

4                                 A DISSERTATION  
5                                 SUBMITTED TO THE DEPARTMENT OF PHYSICS  
6                                 AND THE COMMITTEE ON GRADUATE STUDIES  
7                                 OF STANFORD UNIVERSITY  
8                                 IN PARTIAL FULFILLMENT OF THE REQUIREMENTS  
9                                 FOR THE DEGREE OF  
10                                 DOCTOR OF PHILOSOPHY

11                                 Wei Ji  
12                                 August 2018

<sup>13</sup>

© Copyright by Wei Ji 2018  
All Rights Reserved

<sup>14</sup>

I certify that I have read this dissertation and that, in my opinion, it is fully adequate in scope and quality as a dissertation for the degree of Doctor of Philosophy.

15

---

(Tom Shutt) Principal Adviser

I certify that I have read this dissertation and that, in my opinion, it is fully adequate in scope and quality as a dissertation for the degree of Doctor of Philosophy.

16

---

(Dan Akerib)

I certify that I have read this dissertation and that, in my opinion, it is fully adequate in scope and quality as a dissertation for the degree of Doctor of Philosophy.

17

---

(Peter Graham)

I certify that I have read this dissertation and that, in my opinion, it is fully adequate in scope and quality as a dissertation for the degree of Doctor of Philosophy.

18

---

(Giorgio Gratta)

I certify that I have read this dissertation and that, in my opinion, it is fully adequate in scope and quality as a dissertation for the degree of Doctor of Philosophy.

19

---

()

Approved for the Stanford University Committee on Graduate Studies

20

# <sup>21</sup> Preface

<sup>22</sup> This thesis is discussing about the design and validation of liquid xenon LZ Dark Matter experiment  
<sup>23</sup> and results from LUX Dark Matter experiment.

<sup>24</sup> **Acknowledgments**

<sup>25</sup> I would like to thank you Dan, for everything.

# <sup>26</sup> Contents

<sup>27</sup> <b>Preface</b>	<b>iv</b>
<sup>28</sup> <b>Acknowledgments</b>	<b>v</b>
<sup>29</sup> <b>List of Tables</b>	<b>viii</b>
<sup>30</sup> <b>List of Figures</b>	<b>ix</b>
<sup>31</sup> <b>1 Gas Test descriptions</b>	<b>1</b>
<sup>32</sup> 1.1 The gaseous detector . . . . .	2
<sup>33</sup> 1.2 Data Acquisition . . . . .	7
<sup>34</sup> 1.3 Operation . . . . .	11
<sup>35</sup> 1.4 Data processing . . . . .	14
<sup>36</sup> 1.5 PMT Calibration . . . . .	17
<sup>37</sup> 1.6 Light Collection . . . . .	22
<sup>38</sup> 1.7 Light production . . . . .	25
<sup>39</sup> 1.8 Signals . . . . .	32
<sup>40</sup> 1.8.1 Electron emission . . . . .	32
<sup>41</sup> 1.8.2 Particle radiation . . . . .	36
<sup>42</sup> 1.8.3 Cosmic ray . . . . .	52
<sup>43</sup> 1.8.4 Other miscellaneous sources . . . . .	54
<sup>44</sup> 1.9 Signal selections . . . . .	72
<sup>45</sup> 1.9.1 Signal selections based on signal shape . . . . .	72
<sup>46</sup> 1.9.2 Signal selections based on previous signals . . . . .	79
<sup>47</sup> 1.9.3 Signal selections varying $\Delta V_{T,B}$ and operating gas density . . . . .	85
<sup>48</sup> 1.10 Evaluation . . . . .	91
<sup>49</sup> 1.10.1 Simulations . . . . .	91
<sup>50</sup> 1.10.2 Summary . . . . .	91

51	<b>A Gas Test RQ documentation</b>	<b>93</b>
52	<b>B Abbreviations</b>	<b>100</b>
53	<b>Bibliography</b>	<b>102</b>

# <sup>54</sup> List of Tables

<sup>55</sup> 1.1	Spectral response of PMTs tested at Hamamatsu Photonics . . . . .	5
<sup>56</sup> 1.2	Data Acquisition system parameters. . . . .	8
<sup>57</sup> 1.3	PMT dead time duration . . . . .	11
<sup>58</sup> 1.4	PMT calibration. . . . .	20
<sup>59</sup> 1.5	Light collection simulation geometry parameters. . . . .	24
<sup>60</sup> 1.6	Light collection simulation material parameters. . . . .	24
<sup>61</sup> A.1	<i>Gas Test</i> RQ documentation . . . . .	99

# <sup>62</sup> List of Figures

63      1.1	<i>Gas Test</i> apparatus physical layout. . . . .	4
64      1.2	<i>Gas Test</i> electroluminescence detector. . . . .	6
65      1.3	<i>Gas Test</i> signal: example waveforms during dead time. . . . .	10
66      1.4	Distribution of PMT time differences between pulses in one PMT. . . . .	12
67      1.5	<i>Gas Test</i> good and bad voltage configurations. . . . .	15
68      1.6	PMT pulse amplitude distribution. . . . .	19
69      1.7	PMT SPHE pulse amplitude vs. pulse area distribution. . . . .	21
70      1.8	Light collection efficiency of (r, z) cross section in the ELD from simulation. . . . .	26
71      1.9	Light collection efficiency and TBA in the EL region in different grid configurations from simulation. . . . .	27
72      1.10	Light collection efficiency in the EL region with different PTFE reflectivity from simulation. . . . .	27
73      1.11	The reduced first Townsend ionization coefficient $\eta \equiv \alpha/E$ for neon, argon, krypton, and xenon. . . . .	31
74      1.12	<i>Gas Test</i> electron emission event from grid wires . . . . .	34
75      1.13	<i>Gas Test</i> detector electric field. . . . .	35
76      1.14	A 3D simulation of an electron drifting in an axially symmetric electric field in xenon gas. . . . .	37
77      1.15	Simulated cathodic electron gas gain vs. reduced surface electric field. . . . .	38
78      1.16	Simulated signal areas vs. $\Delta V_{T-B}$ . . . . .	39
79      1.17	Attenuation length of photon in xenon. . . . .	40
80      1.18	CSDA range of electrons in xenon. . . . .	41
81      1.19	<i>Gas Test</i> signal: anode cone event. . . . .	43
82      1.19	<i>Gas Test</i> signal: anode cone event (cont.). . . . .	44
83      1.20	<i>Gas Test</i> signal: cathode cone event. . . . .	45
84      1.21	<i>Gas Test</i> signal: S1 S2 event in the cathode corner. . . . .	47
85      1.22	Electrostatic solution of the <i>Gas Test</i> detector (grid ring region). . . . .	48

90	1.23 <i>Gas Test</i> signal: S1 S2 event in the EL region. . . . .	49
91	1.24 <i>Gas Test</i> signal: grid wire region event. . . . .	50
92	1.25 <i>Gas Test</i> signal: grid ring region event. . . . .	51
93	1.26 <i>Gas Test</i> signal: multiple scattering event. . . . .	53
94	1.27 <i>Gas Test</i> signal: EL region muon event. . . . .	55
95	1.28 <i>Gas Test</i> signal: muon event between the grid rings. . . . .	56
96	1.29 <i>Gas Test</i> signal: anode cone muon event. . . . .	57
97	1.29 <i>Gas Test</i> signal: anode cone muon event (cont.). . . . .	58
98	1.30 <i>Gas Test</i> signal: cathode cone muon event. . . . .	59
99	1.31 <i>Gas Test</i> signal: electronic noise. . . . .	61
100	1.32 <i>Gas Test</i> signal: PMT dark current accidental coincidence. . . . .	61
101	1.33 <i>Gas Test</i> signal: PTFE fluorescence after an event with large photon production. . . . .	63
102	1.33 <i>Gas Test</i> signal: PTFE fluorescence after an event with large photon production (cont.). . . . .	64
103	1.34 Photon fluorescence rate after photon production in the ELD. . . . .	65
104	1.35 The average of scaled waveform in the range of 0 $\mu$ s to 2000 $\mu$ s since source signals. . . . .	67
105	1.36 The ratio of the number of photon in the range of 200 $\mu$ s to 600 $\mu$ s since source signals to the number of photons in the source signal. . . . .	67
106	1.37 <i>Gas Test</i> signal: Cherenkov radiation in PTFE. . . . .	69
108	1.38 <i>Gas Test</i> signal $t_{10-90}$ duration vs. signal area. . . . .	71
109	1.39 <i>Gas Test</i> signal selection (part 1). . . . .	81
110	1.39 <i>Gas Test</i> signal selection (part 2). . . . .	82
111	1.39 <i>Gas Test</i> signal selection (part 3). . . . .	83
112	1.39 <i>Gas Test</i> signal selection (part 4). . . . .	84
113	1.40 <i>Gas Test</i> signal selection with $\Delta V_{T-B}$ at 8 kV, operating gas density at 0.137 mol L $^{-1}$ . . . . .	86
114	1.41 <i>Gas Test</i> signal selection with $\Delta V_{T-B}$ at 10 kV, operating gas density at 0.137 mol L $^{-1}$ . . . . .	87
115	1.42 <i>Gas Test</i> signal selection with $\Delta V_{T-B}$ at 12 kV, operating gas density at 0.137 mol L $^{-1}$ . . . . .	88
116	1.43 <i>Gas Test</i> signal selection with $\Delta V_{T-B}$ at 14 kV, operating gas density at 0.137 mol L $^{-1}$ . . . . .	89
117	1.44 <i>Gas Test</i> signal selection with $\Delta V_{T-B}$ at 16 kV, operating gas density at 0.137 mol L $^{-1}$ . . . . .	90

<sup>118</sup> **Chapter 1**

<sup>119</sup> ***Gas Test descriptions***

<sup>120</sup> In LZ, metallic wire grids under high voltage are used to form electric fields. We apply one field  
<sup>121</sup> in the liquid volume to drift ionization electrons upwards and another in the gas volume to extract  
<sup>122</sup> these electrons from the liquid in order to produce proportional scintillation light (S2). Achieving  
<sup>123</sup> high voltages on such grids is necessary for the operation of the LZ TPC. However, such high voltages  
<sup>124</sup> also increase the rate of electron emission ,which is one of the potential sources of background in  
<sup>125</sup> LZ. Therefore, reduction of the field induced electron emission rate should greatly benefit physics  
<sup>126</sup> studies in the LZ detector.

<sup>127</sup> Electric field induced electron emission from metallic surfaces is a well known phenomenon. The  
<sup>128</sup> electric field lowers the potential energy outside the metallic surface allowing electrons to come out  
<sup>129</sup> from the metallic surface. The rate of electric field induced electron emission increases with the  
<sup>130</sup> electric field on the metallic surface.

<sup>131</sup> The electric field induced electron emission events are potential problems in LZ for three reasons.  
<sup>132</sup> First, these events look like low energy events in the LZ detector. Thus, reduction of electron  
<sup>133</sup> emission background rate from the grid wires improves our sensitivity to low energy events. This  
<sup>134</sup> in turn improves our ability to study low mass WIMPs. Second, the electron emission events may  
<sup>135</sup> accidentally coincide with WIMP signals which we want to study in the LZ detector. Reduction  
<sup>136</sup> of electron emission rate helps to keep the data recording environment in LZ cleaner. This reduces  
<sup>137</sup> the systematic errors for S1 and S2 and improves their quality. From that, we improve our events  
<sup>138</sup> classification and energy reconstruction. This in turn improves all physics studies using the LZ  
<sup>139</sup> detector. Finally, the electron emission events interrupt the desired data recording capability of  
<sup>140</sup> the LZ detector. This may prevent or interrupt recordings of wanted data. Thus, the reduction of  
<sup>141</sup> electron emission rate helps to keep the data recording environment in LZ quieter to allow longer  
<sup>142</sup> detector live times for wanted events. In summary, the reduction of the electron emission event rates  
<sup>143</sup> benefits LZ because of its impact on detector sensitivity, data quality and data acquisition live time.

<sup>144</sup> To achieve these qualities, we are developing a two-stage study on the reduction of the electric

145 field induced electron emission rate using two small detectors, *Gas Test* and *LZ System Test: Phase*

146 *I*. These two detectors are capable of testing a pair of grids which have surface areas  $\sim 1\%$  the

147 area of grids that will be used in LZ. With these small detectors, we can study the effect of rate

148 reduction in a shorter time than if we were to use full-size grids. Thus, we use these detectors to

149 study parameters that may affect the emission rate in a short period of time.

150 At the first stage, a gaseous detector, “*Gas Test*”, is built to study different methods for reducing

151 the electron emission rate. This detector measures electron emission rates with different electric

152 fields before and after various physical and chemical treatments. Once we discover an effect on the

153 reduction of the electric field induced electron emission rate from these treatments, a second stage

154 of study with a liquid xenon detector, *LZ System Test: Phase I*, is undertaken to confirm that

155 reduction persists in a liquid xenon environment, like that of LZ.

156 After confirmation that a treatment produces a rate reduction, this treatment is used to produce

157 full-size LZ grids. A similar two-stage study method is used to test the full-size LZ grids in a gaseous

158 detector, *LZ System Test: Phase II*(details are described in Ref. ??), and the liquid xenon detector

159 LZ. These two detectors measure the performance and assure the quality of LZ grids.

160 This chapter focuses on descriptions of the *Gas Test* detector. I will first introduce the design

161 concepts for each individual component in *Gas Test* . Then I will discuss data acquisition and the

162 data processing framework. **Last, I will discuss the analysis framework ,which includes event selec-**

163 **tions , simulations and validations, as well as characteristic pulse shape and rate of the background**

164 **events.** Results from measurements for different grids in *Gas Test* will be discussed in Chapter.??.

## 165 1.1 The gaseous detector

166 The gaseous detector, *Gas Test*, is designed to study grid behavior under high voltage in LZ. It

167 measures scintillation and electroluminescence (EL) light signals from events in the detector. Pairs

168 of grids are made from the same waving technique, material, wire pitch, and wire diameter as the

169 grids that will be used in LZ. The same pair of grids can also be tested in *LZ System Test: Phase I*

170 to study their performance in liquid xenon. Since these grids are physically similar to the grids in

171 LZ except for the overall surface area, the results from studying these grids are useful for LZ grid

172 design.

173 The main interest of our study is the electron emission process from the grid wires, which

174 is studied by grid electron emission tests via using PMTs to detect the associated photon signals.

175 Before each grid electron emission test, a grid sparking test is carried out to understand the maximum

176 operating voltage and the optimal operating voltage. Grid sparking tests are performed with both

177 gaseous xenon and argon under various pressures in order to uncover discharges in the detector

178 via biasing the grids. It provides the detector operation information for grid emission tests. Grid

179 electron emission tests are usually performed with gaseous xenon, in which photons can be produced

180 for carrying out the electron emission signalmeasurements.

181 Next, I will introduce the design concepts of the components in the *Gas Test* detector.

182 **Detector** *Gas Test* detector is the main tool we used to study the electron emission process from  
183 metallic grid wire surfaces. The *Gas Test* detector operates with xenon gas, argon gas, and vacuum.  
184 The operating pressure for this detector is in the range of  $10^{-5}$  bara to 3.5 bara.

185 A cylindrical vessel, the diameter of which is 10 inch and the height of which is 24 inch, is used to  
186 host a electroluminescence detector(ELD), which detect measurable events. The pressure and the  
187 temperature of the detector are monitored by sensors mounted above the vessel. A gas circulation  
188 system is used to add, remove and purify gas in the detector. Fig. 1.1a and Fig. 1.1b show the  
189 physical layout of the vessel setup and the ELD inside.

190 The electroluminescence detector (ELD) is the major location of active measurable electron  
191 emission events. Its conceptual drawing is illustrated in Fig. 1.2. A pair of grids for measurement  
192 are mounted in the center of the vessel. They are separated apart by 12 PEEK spacers, ,which are  
193 13 mm in height. These two grids are biased to different voltages during the measurement. This  
194 creates a voltage difference between the two grids. It enables electrons between these two grids to  
195 produce EL photons ,which can be measured by the PMTs. The region between these two grids is  
196 called the EL region.

197 These grids are named after their physical location in the detector as top grid and bottom grid.  
198 The grid plane diameters are 140.9 mm for the top grid and 137.4 mm for the bottom grid. Voltages  
199 of the two grids are noted as  $V_T$  for the top grid and  $V_B$  for the bottom grid. The voltage difference  
200 between the top and bottom grids is expressed with  $\Delta V_{T-B}$  ( $dV$ )  $\equiv V_T - V_B$ . These grids also  
201 have another name by their bias voltages; the anodic grid and cathodic grid, and their voltage are  
202 respectively  $V_A$  and  $V_C$ . The top grid is anodic and the bottom grid is cathodic when studying  
203 electron emission from the bottom grid, which is called normal polarity operation. Occasionally, the  
204 top grid is cathodic and the bottom grid is anodic when studying electron emission from the top  
205 grid, which is called reverse polarity operation.

206 Two PTFE reflector cones are used to improve light collection efficiency for the primary scintil-  
207 lation and EL photons. These reflector cones are mounted on the top and bottom of the EL region.  
208 The surface of the PTFE cones overhang 0.1 mm above the grid. The diameters of the opening of  
209 the PTFE cones to the grids are 130 mm. The EL region have the most sensitivity for grid electron  
210 emission signal with regart to light collection. The EL region defines the overall grid surface area  
211 of studying. Two PMTs mounted on the PTFE reflector cones are used to measure the primary  
212 scintillation and EL photons. Distances between the PMTs to the closest grids are 110 mm.

213 The two PMTs used to measure the primary scintillation and EL photons from events happening  
214 in the detector are model R11410-20 PMTs manufactured by Hamamatsu Photonics, as described  
215 in Ref. [1]. The model of PMT has a synthetic quartz window that is mostly transparent to incident  
216 photons of  $\sim 175$  nm (xenon scintillation photons). The PMT window is coated with a bialkali



Figure 1.1: *Gas Test* apparatus physical layout. (a) The *Gas Test* detector: detector vessel (middle), electronic and gas gauge breakouts (top), Genie lift for detector assembly and disassembly (left), vacuum pumps and leak checking system (right). (b) ELD inside the detector vessel. (c) Gas circulation panel. (d) Circulation pump (left), and storage bottles (right).

photocathode material, which absorbs the incident photon and emits electrons by the photoelectric effect. The emitted electron which lands on the effective area of the first dynode is multiplied along the PMT dynode chain in an electron gain process and observed, which is the measured signal. The two PMTs are named after their physical location in the detector as top PMT and bottom(bot) PMT. Their spectral response of is summarized in Table 1.1.

	Top(top) PMT	Bottom(bot) PMT
Serial Number	KB1163	KB1170
Cathode Luminous Sens. [ $\mu\text{A lm}^{-1}$ ]	149.0	148.0
Anode Luminous Sens. [ $\text{A lm}^{-1}$ ]	657.0	1010.0
Anode Dark Current [nA]	1.00	4.60
Cathode Blue Sens. Index	12.60	12.30
Q.E. [%]		
165 nm	22.1	21.2
170 nm	33.3	32.6
175 nm	36.3	36.0
182 nm	37.1	37.0
188 nm	36.1	36.2
194 nm	33.9	34.1
200 nm	32.6	32.9

Table 1.1: Spectral response of PMTs tested at Hamamatsu Photonics.

A CAEN R1470ETD high voltage power supply is used to bias the two grids and the two PMTs. Two custom ceramic feed-throughs are used to deliver high voltage to the two grids in the detector vessel. Each feed-through has a low-pass filter box attached for noise removal. Custom designed cables and cable terminations are used to apply voltages through the feed-throughs to the grids. The cable terminations were a limitation on our ability to bias the grids to high voltage. New design elements have been introduced to solve this problem. Details of iterations of these designs will be discussed in Chapter. ??.

**Gas circulation system** A gas circulation system is used to purify, add, and remove xenon gas in the detector. The circulation system maintains the gas purity condition in the detector, which is essential for the operation for the following reasons. The purity of xenon gas ensures that electrons that are produced in the ELD do not combine with impurity atoms, thus decreasing the production of primary scintillation and EL light. The purity of xenon also has a notable effect on electron drift velocity in xenon gas, which biases our study; that is impure xenon gas tends to have a slower electron drift velocity. The deviation of electron drift velocity between different impurity levels can reach 20 % in certain reduced electric fields (ratio of electric field to gas density), as described in Ref. [Brooks1982]. This deviation biases the electron emission signal selection, which is based on the predicted pulse duration according to electron drift velocity, and introduces systematic error to the electron emission signal study.

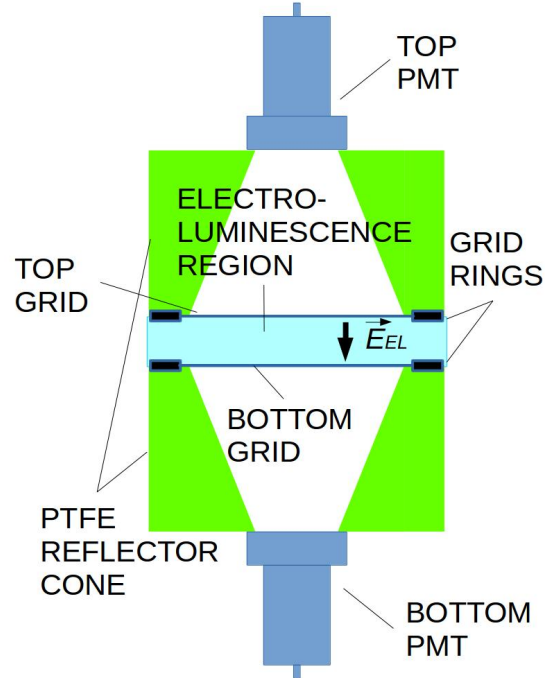


Figure 1.2: Conceptual drawing of *Gas Test* electroluminescence detector (ELD)

Xenon purification is carried out with the following elements in the gas circulation system. A gas circulation panel (Fig. 1.1c) is used to control the flow of xenon gas. A SAES PS3-MT3-R-1 rare gas purifier mounted on the circulation panel is used to purify the gas. The getter element has a sub-ppb efficiency of removing water, nitrogen, oxygen, carbon oxide, carbon dioxide, hydrogen, and hydrocarbons, as described in Ref. [2]. A custom pump (Fig. 1.1d) manufactured by KNF Neuberger, Inc. drives the gas circulation in the system. This pump is a type PM26101-0150.1.2.12 double diaphragm pump, which has company specified 1.5 bar operating pressure, as described in Ref. [3]. During the actual operation, the pump works at pressures of up to 3.7 bar with a leak rate less than  $10^{-7}$  bar L s<sup>-1</sup>. An Alicat MC-5SLPM-D-485 mass flow controller (MFC) on the gas circulation panel controls the circulation flow rate, which allows a maximum flow rate of 5 slpm, as described in Ref. [4]. During the gas purification process, the flow of gas was controlled and driven through the getter for  $\sim$ 20 min to allow the complete absorption of the gas impurities in the detector. This process is frequently conducted between each dataset to ensure the gas purity quality.

The addition and removal of xenon gas are carried out with the same gas panel. Two 4 L bottles (Fig. 1.1d) are used for the storage of xenon gas used in the tests when the gas is not used in the detector. During the xenon gas removal process, these bottles are inserted into two dewars filled with liquid nitrogen. Reducing the temperature of the bottles by using liquid nitrogen allows xenon

257 gas to flow through the gas circulation panel back to the bottles, and to condense inside the bottles.  
258 During the addition of xenon gas process, the bottles are taken out from the dewar and warmed up.  
259 This process raises the gas pressure in the bottle, which drives the gas to fill the detector through  
260 the getter on the gas panel. The gas flow is controlled by the gas regulator and the MFC on the  
261 panel.

## 262 1.2 Data Acquisition

263 A data acquisition(DAQ) system is used for recording PMT pulses for grid emission tests. The  
264 DAQ system is designed and made at SLAC, previously used and tested in *LZ System Test: Phase*  
265 *I* detector. The DAQ system is customized to maximize the probability for capturing single photon  
266 electron (SPHE) pulses from the PMTs. This also enables the DAQ system to record electron  
267 emission signals, which are collections of multiple SPHE pulses. The DAQ system contains three  
268 parts: (1) amplification and digitization, (2) recording, and (3) transfer and storage. The DAQ  
269 system works continuously, except when interrupted by the data transfer process. This interruption  
270 is called dead time of the DAQ system. The dead time issue is addressed by the subtraction of live  
271 times after each recorded pulses. Aspects of the DAQ system are described below.

272 **Amplification and digitization** This process amplifies and digitizes PMT pulse signals. The  
273 amplification and digitization of the PMT signals are carried out by two separate custom made  
274 boards. The amplification of signals improves signal to noise ratio. However, this amplification may  
275 also cause distortion of the waveform if the pulse signal amplitude exceeds the maximum capability  
276 of the electronic circuits in the amplification and digitization boards. Two amplifier gain settings  
277 are implemented: low gain ( $\times 12$ ), and high gain ( $\times 100$ ). For electron emission tests, the low  
278 gain setting is used to obtain a satisfactory signal to noise ratio. The low gain setting allows 40 to  
279 60 SPHEs to be recorded simultaneously without distortion, when the high gain setting is not used  
280 because its without distortion SPHE recording range is only 5 to 7 SPHEs, which is too small for the  
281 counts of simultaneous SPHEs in electron emission signals. An optical fiber connecting these two  
282 boards transfers the amplified PMT signals to the digitizer board. The digitizer board is capable of  
283 doing a 16 bit digitization in a dynamic range of 2.5 V ( $\sim -1.26$  V to 1.24 V). The digitizer reverses  
284 the polarity of signals, which changes SPHE pulses from negative spikes to positive spikes. The  
285 digitizing sampling frequency is every 4 ns. Digitized data are written to a buffer memory in the  
286 digitizer board. The amplification and digitization system sets the precision of SPHE measurement  
287 and signal to noise ratio, and digitizes PMT pulse signals to be handled numerically later.

288 **Recording** The recording system for DAQ makes decisions for data recording. The decision  
289 making algorithm is controlled by customized DAQ XML parameters in an XML file. The pulse  
290 recording is undertaken in a pending mode without a conventional trigger, which is explained below.

291 First, the continuous digitized pulse amplitude data are compared to a pre-threshold voltage (trigger  
 292 voltage), which is called the pre-threshold value, until a threshold crossing is reached. The time of  
 293 this threshold crossing is the pulse recording reference time (trigger time). Pulse recording also  
 294 includes a preceding segment of samples, which is called the pre-delay. The start time of the  
 295 pre-delay period is the pulse recording start time. Next, digitized data are compared to a post-  
 296 threshold voltage, which is called the post-threshold value, until a threshold crossing is reached.  
 297 Then, the pulse recording continues for a succeeding segment of samples, which is called the post-  
 298 delay. During the post-delay period, the digitized data are compared to the pre-threshold value  
 299 again. If no pre-threshold crossing is reached, the pulse recording ends when the post-delay period  
 300 ends. Otherwise, the DAQ system keeps recording until after a post-threshold crossing is reached,  
 301 no other pre-threshold crossing is reached in the next post-delay period. The end time of the last  
 302 post-delay period is the pulse recording stop time. The pre-threshold values are chosen so that the  
 303 SPHE recording efficiency, also called the trigger efficiency, of both PMTs are larger than 95 %. The  
 304 trigger efficiency is estimated by fitting SPHE amplitude distributions to Gaussian distributions, as  
 305 described in Section 1.5. Results of these evaluations show that at normal PMT operating voltage  
 306 ( $-1.5\text{ kV}$ ) the top PMT and the bottom PMT have good trigger efficiency of 99.6 % and >99.9 %.  
 307 The recorded pulses are called pulses of digitization (PODs), which are one of the fundamental  
 308 elements for the next step; coincidence event building, as described in Section 1.4.

309 The used DAQ XML parameters during the tests are summarized in Table 1.2.

name	XML parameter name	value	explanation
post-delay	‘PostDelay’	500 sample	counts of samples to keep after crossing post-trigger threshold (‘PostThreshold’).
pre-delay	‘PreDelay’	30 sample	counts of samples to keep before crossing pre-trigger threshold (‘PreThreshold’).
post-threshold	‘PostThreshold’	0x7D80 or as needed	crossing this threshold value determines the stop time of pulse recording.
pre-threshold	‘PreThreshold’	0x7D61 or as needed	crossing this threshold value determines the start time of pulse recording.

Table 1.2: DAQ system parameters. (1 sample is 4 ns.)

310 **Transfer and storage** The transfer and storage system transfers data from the digitizer board  
 311 and stores data in binary format in the main computer system. The buffer memory data that pass  
 312 the selection of trigger algorithm are transferred through an optical fiber and written to files stored  
 313 in the main computer. The data transfer speed is  $250\text{ MB s}^{-1}$ . For an average pulse duration of

314  $2\ \mu\text{s}$  (500 sample), the DAQ allows approximately 30 thousand pulses to be recorded per second.  
315 The continuously recorded data are separately saved to series of files; each with a maximum size of  
316 1.1 GB. The process of data transfer interrupts the process of buffer memory writing of the incoming  
317 digitized data, which raises the dead time issue.

318 **Dead time** The dead time of DAQ is the segment of time that the DAQ system stops working  
319 after the end of each pulse recording. The reason for the dead time is because the process of buffer  
320 writing and the process of data transfer in the DAQ system cannot happen simultaneously. Dead  
321 time issue brings challenges in measuring electron emission rates. The duration of dead time shows  
322 a dependence on the preceding pulse duration. However, the quantitative relationship between the  
323 two is unclear. We address this issue by subtracting a segment of time succeeding each recorded  
324 pulse from the live time of study.

325 We studied the dead time issue by using two methods. The first method is finding problematic  
326 pulses that might be a result of dead time. We found there exist a population of pulses that when  
327 one PMT detects large quantities of photons, the other PMT detects no photon simultaneously.  
328 Since the two PMTs are observing the same space in the ELD, we expect to see similar magnitude of  
329 photons in both PMTs. The most likely reason for this to happen is that the other PMT channel is  
330 suffering from dead time. The other possible causes of these problematic pulses, such as misbehavior  
331 of one PMT, are less dominant. The time difference between the recording time of large quantities  
332 of photons in one PMT and the first preceding pulse in the dead time problematic PMT is the  
333 potential duration of dead time, as shown in Fig. 1.3. More than 400 dead time problematic pulses  
334 are examined. From the examinations, we found that for a particular pulse with a duration of  $2\ \mu\text{s}$ ,  
335 the duration of dead time is in the range of  $0.3\ \mu\text{s}$  to  $15\ \mu\text{s}$ . For longer pulses, we observe the duration  
336 of dead time for as long as  $80\ \mu\text{s}$ .

337 To estimate the systematic error, we employ a second method based on the idea that the presence  
338 of dead time will shift the distribution of time intervals between pulses in one PMT. In the absence  
339 of dead time, the time distribution should be an exponential characterized by the average rate.  
340 The impact of dead time is to shift time difference probability an exponential curve, which is from  
341 assuming uniform distribution:

$$\text{probability} = \frac{1}{\tau} \exp\left(-\frac{t}{\tau}\right) \quad (1.1)$$

342 where  $\tau$  is the time constant, which is the inverse of average rate.

343 Results of this shift is shown in Fig. 1.4. The figure includes studies of pulses categorized by their  
344 durations. These studies confirm the previous conclusion on the dead time issue dominant period,  
345 and further show that such period has a dependence on the preceding pulse duration. The clear low  
346 statistics at the small time interval range, e.g. range  $0\ \text{ns}$  to  $10^5\ \text{ns}$  for pulse length in the range of  
347 larger than  $30\ \mu\text{s}$ , clearly showed the shift from expected exponential curve. The low statistic region

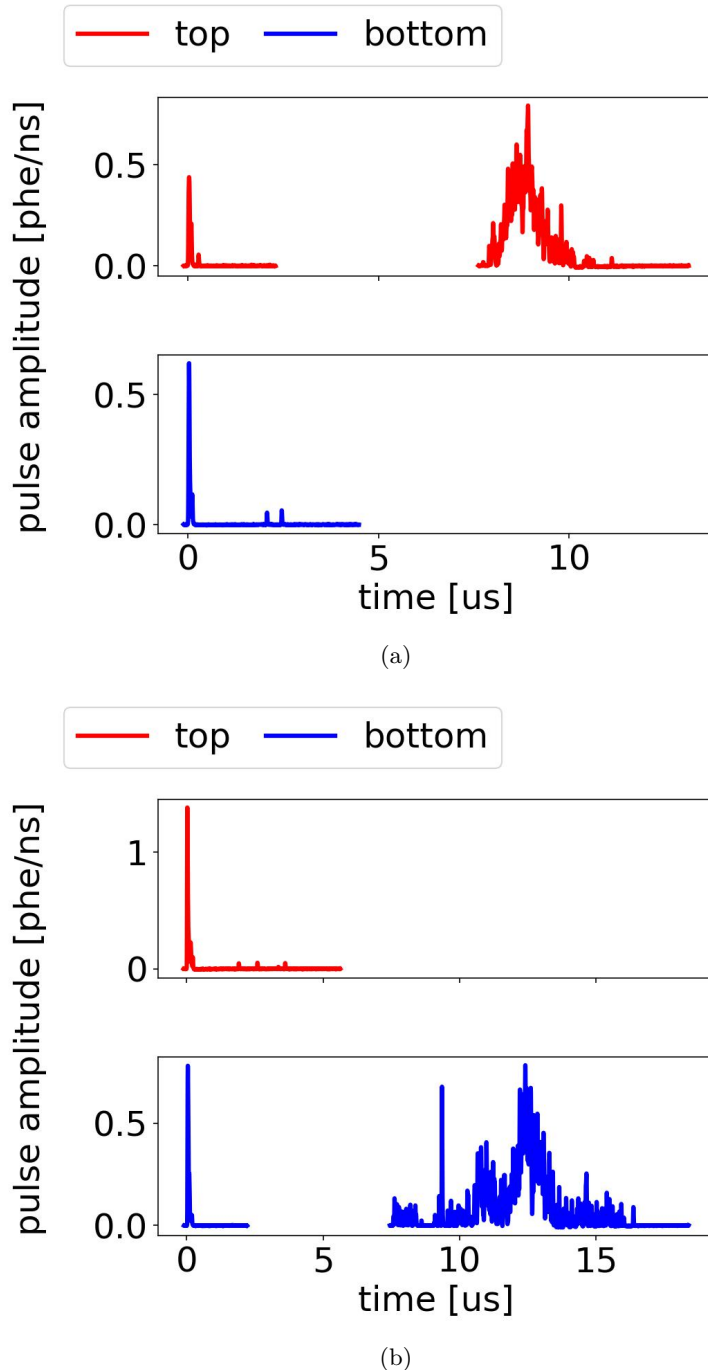


Figure 1.3: *Gas Test* signal: example waveforms during dead time. (a) The top PMT channel is suffering from dead time. (b) The bottom PMT channel is suffering from dead time.

348 changes with preceding pulse duration, as summarized in Table 1.3. The difference on the slopes  
 349 of these curves is due to PTFE fluorescence subsequent to each pulse, which is more obvious for  
 350 larger area (long duration) pulses, and increases the succeeding average rate, as will be discussed in  
 351 Section 1.8.

pulse duration [μs]	dead time duration (low statistics region) [μs]	dead time duration (maximum observed) [μs]
all	7	80
[0, 3)	7	15
[3, 10)	10	15
[10, 30)	50	80
[30, ∞)	100	80

Table 1.3: PMT dead time duration. Data were taken at 2017-12-8 14:02, with grid voltages  $V_T$  and  $V_B$  at +6 kV and -6 kV, operating gas density at  $0.137 \text{ mol L}^{-1}$ .

352 Thus, to resolve the dead time issue, we subtract a segment of time after each recorded pulse  
 353 from the live time of study and eliminate all pulses that is recorded in this time period, as described  
 354 in Section 1.9. The remained pulses that have quiet preceding are used to study the absolute rate  
 355 of signals of interest, electron emission signals. The rate of signals of interest is close to such rate  
 356 without the dead time issue from the view of DAQ behavior.

### 357 1.3 Operation

358 think about where to put run selection section. I want to take about , what is sparking test, what  
 359 is normal operation before electron emission tests. This is the reason this section is here. however,  
 360 put it just in front of cut might also be good.

361 The run selections are to make sure that we have stabilized run conditions to analysis electron  
 362 emission process from grids we are studying.

363 **Operating conditions** The normal run of *Gas Test* electron emission test is operated with (1)  
 364 the detector filled with xenon gas, (2) two PMTs stably running, and (3) two grids bias to proper  
 365 voltages.

366 The typical operating xenon gas density for electron emission tests is  $0.137 \text{ mol L}^{-1}$  ( $\sim 3.3 \text{ bara}$  at  
 367 temperature 295 K, or equivalent to the xenon gas density at 177 K on xenon liquid-vapor saturation  
 368 curve). This choice minimizes the probability of discharges between two grid electrodes. It also  
 369 makes the grids operates under the gas density closest to LZ operating gas density. These discharges  
 370 may cause potential damages to grids, and also prevent stable run.

371 The gas operating condition at density  $0.137 \text{ mol L}^{-1}$  allows us having sensitivities measuring  
 372 electron emission from  $\Delta V_{T-B}$  in the range of 8 kV to 16 kV. For a plain woven grid with wire pitch

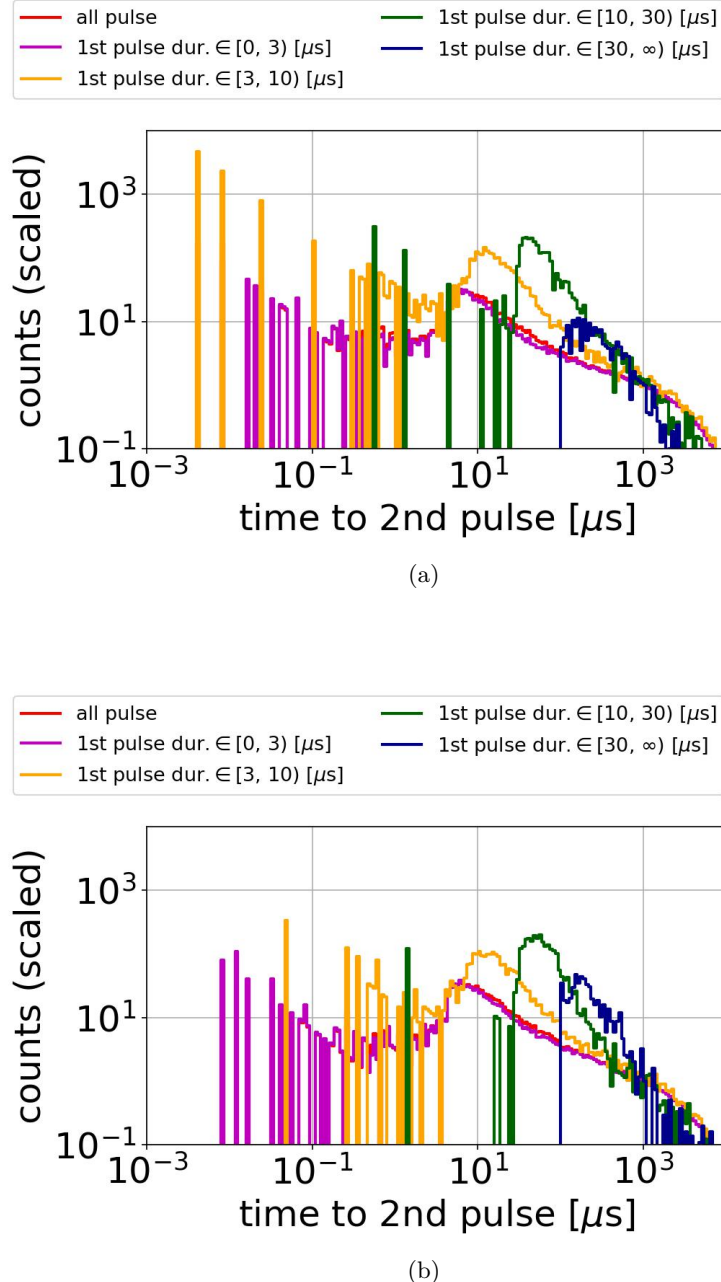


Figure 1.4: Distribution of PMT time differences between pulses in one PMT: (a) top PMT; (b) bottom PMT.

373 5 mm and wire diameter  $75 \mu\text{m}$ , this correspond to an average wire surface electric field in the range  
 374 of  $65 \text{ kV cm}^{-1}$  to  $110 \text{ kV cm}^{-1}$ . However, since EL yield decreases as the reduced electric field (ratio  
 375 of electric field to gas density) in the EL region decreases, the photon yield per electron emission  
 376 is smaller for a lower  $\Delta V_{T-B}$ . This prevents us to have enough sensitivities for electron emission  
 377 for a lower operating voltage and wire surface electric field . So electron emission rate for a lower  
 378 wire surface electric field is measured at a lower gas density to get an increasing on the reduced  
 379 electric field, which leads to a higher the EL photon production in gas. The dependence of EL light  
 380 production on reduced electric field is described in Section 1.8.

381 Two PMTs normally operate at  $-1.5 \text{ kV}$ . This guarantees both PMTs having enough gain and  
 382 signal to noise ratio. Before safely turning on the PMTs to measure the light emission from the  
 383 grids, a series of sparking tests are done to figure out the high voltage behavior and high voltage  
 384 weak points in the system. Improvements are done to improve the maximum grid voltages  $V_T$  and  
 385  $V_B$ . These improvements include cleaning the surface of discharging spots, increasing the smooth-  
 386 ness and rounding radius on the corner of metal surfaces, and increasing the discharge distance  
 387 between electrodes and the ground. Touching grid wires are avoided during these improvements.  
 388 The maximum grid voltages  $V_T$  and  $V_B$  that these grids can hold are measured with different gas  
 389 and different pressures. Dark current of both PMTs in stable running condition are approximately  
 390 500 Hz to 1000 Hz. Runs with any PMT dark current rate above 2500 Hz are excluded.

391 The high voltage power supply is capable to bias both grids separately in the range of  $-8 \text{ kV}$  to  
 392  $8 \text{ kV}$ . The current between the power supply and the grid is monitored to guarantee stable operation  
 393 of grid bias voltages. An unstable grid biasing usually shows as a spike in the monitored current,  
 394 and a spike on PMT recording rates. Segments of time with this monitored current unstable are  
 395 excluded.

396 **Operating data taking** The most common operating voltage pairs we choose for electron emission  
 397 measurement at xenon gas density  $0.137 \text{ mol L}^{-1}$  are  $V_T = -V_B$  at  $\pm 4 \text{ kV}$ ,  $\pm 4.5 \text{ kV}$ ,  $\pm 5 \text{ kV}$ ,  $\pm 5.5 \text{ kV}$ ,  
 398  $\pm 6 \text{ kV}$ ,  $\pm 6.5 \text{ kV}$ ,  $\pm 7 \text{ kV}$ ,  $\pm 7.5 \text{ kV}$ , and  $\pm 8 \text{ kV}$ . This allows us to measure electron emission rate vs.  
 399  $\Delta V_{T-B}$  curves for most grids we study. Measurements in other conditions are also performed to  
 400 understand the detector better. However, their results usually are not included for the electron  
 401 emission studies.

402 The typical duration of data taking is three minutes. An increasing trend of light production is  
 403 seen during the operations when data taking is longer than three minutes. This is probably from  
 404 the increasing of EL light production from the more ionized chamber environment and increasing  
 405 of fluorescence light emission from PTFE reflector cones in the detector. Usually, after each 3 min  
 406 dataset, high voltage power for both grids are set back to 0 kV and rest for at least 30 s before the  
 407 next measurement. Data taking at each voltage configuration is handled by using scripts in Ignition  
 408 slow control software, as described in Ref. [Ignition2018]. This is to make sure data taking is done  
 409 in a consistent reproducible way.

410 Datasets with the cathodic grid bias voltage  $> -2.5$  kV are explicitly excluded for electron emis-  
 411 sion measurements. The reason is because this configuration allows electrons created by external  
 412 particle in the cone region drifting to the EL region. These electrons will produce EL light in the  
 413 EL region. This could introduce a background for electron emission rate study. The process is  
 414 illustrated in Fig. 1.5.

## 415 1.4 Data processing

416 Data processing is to save the useful information of data by reducing the amount of extraneous  
 417 information. This reduces size of analysis works. The useful information of a pulse are characterized  
 418 by Reduce Quantities (RQs) of a pulse.

419 The data processing framework include three parts: (1) single pulse processing, (2) coincidence  
 420 event building and coincidence pulse processing, and (3) random segment sampling of the dataset.

421 This section explains the main part of data processing framework. It does not mean to explain  
 422 all the RQs that have been computed. A full documentation of the RQs used in *Gas Test* analysis  
 423 is summarized in Appendix. A.

424 **Single pulse processing** A single pulse of digitization, POD, is defined to be the individual pulse  
 425 recorded by DAQ system in only one PMT channel. Two steps are done for this processing: (1)  
 426 waveform reconstruction, and (2) pulse shape characterization.

427 The waveform is reconstructed with the following method. First, the baseline voltage of the pulse  
 428 (RQ name: ‘baselines’) is found from the average DC voltages of the pulse of the first 10 samples.  
 429 The baseline voltage represents the voltage at the time when the pulse is recorded assuming no pulse  
 430 occurs. Samples used for baseline finding are 80 ns ahead the trigger time of the pulse. Therefore,  
 431 these samples provide a reliable measure of the baseline since they are close in time with the rest  
 432 of the pulse and unaffected by the rest of the pulse. There are some smaller fluctuation of baseline  
 433 voltages for both PMTs. The amplitude of fluctuation  $\sim 0.36$  mV is very small comparing to SPHE  
 434 pulse amplitude, which is 15 mV to 35 mV. After baseline finding, the baseline value was subtracted  
 435 from the digitized data to get the waveform for the pulse. The waveform is then scaled back from  
 436 ADC counts to mV to get the reconstructed waveforms. Along this process, RQs for the voltage of  
 437 the trigger sample (RQ name: ‘trigvals’), the voltage of the first sample (RQ name: ‘firstvals’) are  
 438 also calculated.

439 From the reconstructed waveform, the maximum positive amplitudes(RQ name: ‘waveampli-  
 440 tudes’) and the pulse area (RQ name: ‘waveareas’), which is the time integral of the pulse amplitude  
 441 are calculated. However, because of the long post-delay duration ( $2 \mu\text{s}$ , 500 sample) from the DAQ  
 442 pulse recording, baseline fluctuation during the post-delay era is included in the total time integral  
 443 of the pulse area. This biases our understanding of pulse area. Thus, another revised pulse area RQ

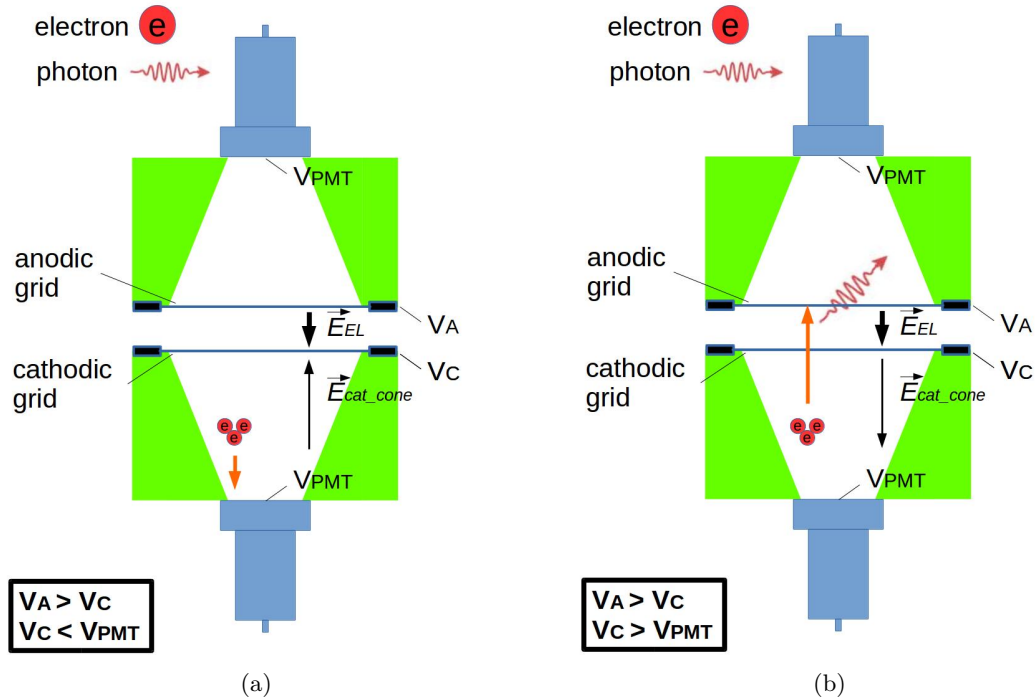


Figure 1.5: (a) Good configuration ( $V_C < V_{PMT}$ ): drift fields pointing from PMT to the grids. Electrons created in the cone region will drift to PMT. This process does not create numerous photons as electron emission signal. (b) Bad configuration ( $V_C > V_{PMT}$ ): drift fields pointing from grids to the PMT. Electrons created in the cone region will drift to EL region. This process creates plenty of EL photons which could look like an electron emission signal.

444 (RQ name: ‘waveareas.trim.end’) is calculated from integrating the waveform with removing the  
 445 last  $1.8\ \mu\text{s}$ , 450 sample from the end of the waveform. This revised pulse area RQ is used in main  
 446 analysis instead for PMT pulse area calibrations.

447 Series of pulse shaping parameters are also calculated. Time weighted integral of waveform (RQ  
 448 name: ‘wtimeN’) is used to study the skew and kurtosis of the pulse. Also, time difference between  
 449 the start time of the pulse and time that the 90th percentile of the pulse waveform are calculated.  
 450 They are the characteristic time differences of the pulse (RQ name: aft\_tXX). They are very useful  
 451 for understanding the pulse shape, pulse duration, and pulse center of mass. These help pulse  
 452 selection and classification discussed in the following sections.

453 **Coincidence event building and coincidence pulse processing** The DAQ system records  
 454 pulses in each PMT channel independently. A true electron emission signal usually can produce  
 455 enough quantity of photons to be recorded by both PMTs. RQs of coincidence pulses between two  
 456 PMTs contain more useful information for electron emission signals. So, for each dataset we take,  
 457 we do a coincidence event building and a coincidence event processing to help us separating electron  
 458 emission signals from other background events, such as dark currents in one PMT.

459 The coincidence event building is done with the following method, requiring records in both  
 460 PMTs within a short period of time. The PODs are grouped in a pending searching, which is not  
 461 just two but all PODs that are recorded close in time are grouped together.

462 First, a POD time subtraction is done to preserve only the useful part of the POD signal. For all  
 463 single PODs, two segments of time were subtracted from the beginning and end of a POD to reduce  
 464 the influence from the baseline fluctuation in the PMT. The default values for post-POD subtraction  
 465 and pre-POD subtraction is 1800 ns (450 sample) and 0 ns (0 sample). The time subtraction preserves  
 466 120 ns before the first pre-threshold crossing time, and 200 ns after the last post-threshold crossing  
 467 time, where between the two crossing time is the signal dominant time period. Now, this beginning  
 468 and ending time of the remained part of the POD is called the start ( $t_{start}$ ) and the stop time ( $t_{stop}$ )  
 469 of the POD.

470 Second, a POD searching is performed between a certain segment of time before the start of  
 471 a single POD and the same amount of time after the stop time of the POD. The value of ad-  
 472 ditional segments of time looking for coincidence is coincidence window width (CWW, RQ name  
 473 ‘window\_width’). The value of CWW for this analysis is  $1.7\ \mu\text{s}$ , if not otherwise specified. If no  
 474 other pulse is found in this time region, no coincidence is found for this particular single POD. If  
 475 another pulse is found in this time region, we say these two pulses are connected.

476 Third, we group all connected pulses to form undividable coincidence pulse groups. A coincidence  
 477 pulse group contains all pulses that are connected to any element in the group, and cannot be divided  
 478 to subgroups that match the same criterion.

479 Then, we check whether the coincidence pulse group contains PODs from both PMTs. If so, we  
 480 determine a coincidence event building is successful.

481     Last, we characterize coincidence pulse RQs from forming coincidence pulse waveforms. A co-  
 482     incidence pulse waveform is defined as the addition of normalized pulse waveforms in each channel.  
 483     The normalization is done by dividing the pulse waveform amplitude by the SPHE pulse area in  
 484     that channel. A similar pulse characterization is performed for the coincidence pulses as in single  
 485     POD processing.

486     Coincidence pulse RQs are the fundamental parameters for electron emission signal analysis  
 487     framework, which will be described later. Some commonly used coincidence pulse RQs are listed  
 488     below. They are

- 489       • coincidence pulse area: RQ name ‘coin\_pulse\_areas\_norm’, pulse area of coincidence pulse,  
 490       measured in phe.
- 491       •  $t_{XX}$ : RQ name ‘coin\_pulse\_areas\_tXX’, time difference between the start of the coincidence  
 492       pulse and integrated pulse area reach XX % of the total coincidence pulse area, measured in  
 493       ns. XX = 01, 05, 10, 15, 25, 50, 75, 85, 90, 95, 99.
- 494       • signal  $t_{01-99}$  duration ( $t_{01-99}$ ):  $t_{99} - t_{01}$ .
- 495       • signal  $t_{10-90}$  duration ( $t_{10-90}$ ):  $t_{90} - t_{10}$ .
- 496       • signal  $t_{25-75}$  width ( $t_{25-75}$ ):  $t_{75} - t_{25}$ .
- 497       • signal  $t_{50}$  width ( $t_{50}$ ).
- 498       • top-bottom asymmetry (TBA): TBA  $\equiv (T-B)/(T+B)$ , where T is the pulse area in the top  
 499       PMT; and B is the pulse area in the bottom PMT.

500     **Random segment sampling** The event rates are checked by looking at pulses around a random  
 501     sample of times during the operation. In each dataset, 10,000 random times are chosen. From each  
 502     random time, total pulse area in the preceding and the succeeding 10  $\mu$ s, 20  $\mu$ s, 50  $\mu$ s, and 100  $\mu$ s  
 503     windows are calculated. These values of random sampling represent the average photon density  
 504     in the detector in this dataset. They are compared to other segments of time of interest to study  
 505     correlation light production.

## 506     1.5 PMT Calibration

507     PMT calibrations are performed for understanding the trigger efficiency, pulse amplitude, and pulse  
 508     area of a SPHE for each PMT. SPHE trigger efficiency of a PMT, the probability of SPHE signal  
 509     recording, determines the event recording efficiency. SPHE pulse amplitude of a PMT determines  
 510     the capability of DAQ to record the full height of a sized pulse. SPHE pulse area of a PMT is the

511 fraction denominator we use to calculate the counts of photon electrons in each pulse. Counts of  
512 photoelectrons in each pulse are roughly estimated by,

$$\# \text{ photoelectrons in a pulse [phe]} \sim \frac{\text{total pulse area}}{\text{single photon electron pulse area}} \quad (1.2)$$

513 Datasets that are used in the calibration are taken at vacuum and grid voltages  $V_T$  and  $V_B$  at  
514 0 kV. The detector in this condition will have the minimum influence from events from internal and  
515 external sources. Thus, a cleaner population of SPHE can be selected.

516 **PMT trigger efficiency** PMT trigger efficiency is estimated by comparing its trigger voltage  
517 (pre-threshold voltage) to its SPHE amplitude distribution. A simple Gaussian distribution is used  
518 to represent the distribution of SPHE amplitude. A fit range in the pulse amplitude of is chosen to  
519 avoid the influence from noise and overlapping of multiple photo electrons. The fit range is 12 mV to  
520 28 mV for the top PMT, and 22 mV to 38 mV for the bottom PMT. The range choices are  $\sim \pm 8$  mV  
521 from the center peak values of the SPHE pulse amplitude. The trigger voltage of each PMT is  
522 compared to the survival function (complementary cumulative distribution function) of the fitted  
523 Gaussian distribution to get the trigger efficiency. Results of curve fittings are shown in Fig. 1.6.  
524 The figures show a close to unity trigger efficiency of both PMTs.

525 **PMT SPHE pulse area** PMT SPHE pulse area is calibrated with fitting the pulse amplitude  
526 and integrated area to a two dimensional Gaussian distribution. A fit range in the pulse amplitude  
527 and area is chosen to avoid the influence from noise and overlapping of multiple photo electrons  
528 this time. The fit ranges are 12 mV to 28 mV, 0 mV ns to 800 mV ns for the top PMT, and 22 mV to  
529 38 mV, 0 mV ns to 1000 mV ns for the bottom PMT. These chosen ranges contain the SPHE peaks  
530 of particular PMTs ,which is identified as the brightest feature above the noise and attributed to  
531 dark current. The used fitting function is,

$$z = A \exp \left( - \left( \frac{1}{2\sigma_x^2} ((x - \mu_x) \cos \theta - (y - \mu_y) \sin \theta)^2 + \frac{1}{2\sigma_y^2} ((x - \mu_x) \sin \theta + (y - \mu_y) \cos \theta)^2 \right) \right) \quad (1.3)$$

532 where x is the pulse area;  
533 y is the pulse amplitude;  
534 z is the total counts at each pulse area and amplitude, represented in the color scale;  
535 A is the amplitude of the fit;  
536  $\mu_x$  is the position of the center of the peak on x axis;  
537  $\sigma_x$  is the standard deviation on rotated x axis;  
538  $\mu_y$  is the position of the center of the peak on y axis;  
539  $\sigma_y$  is the standard deviation on rotated y axis;

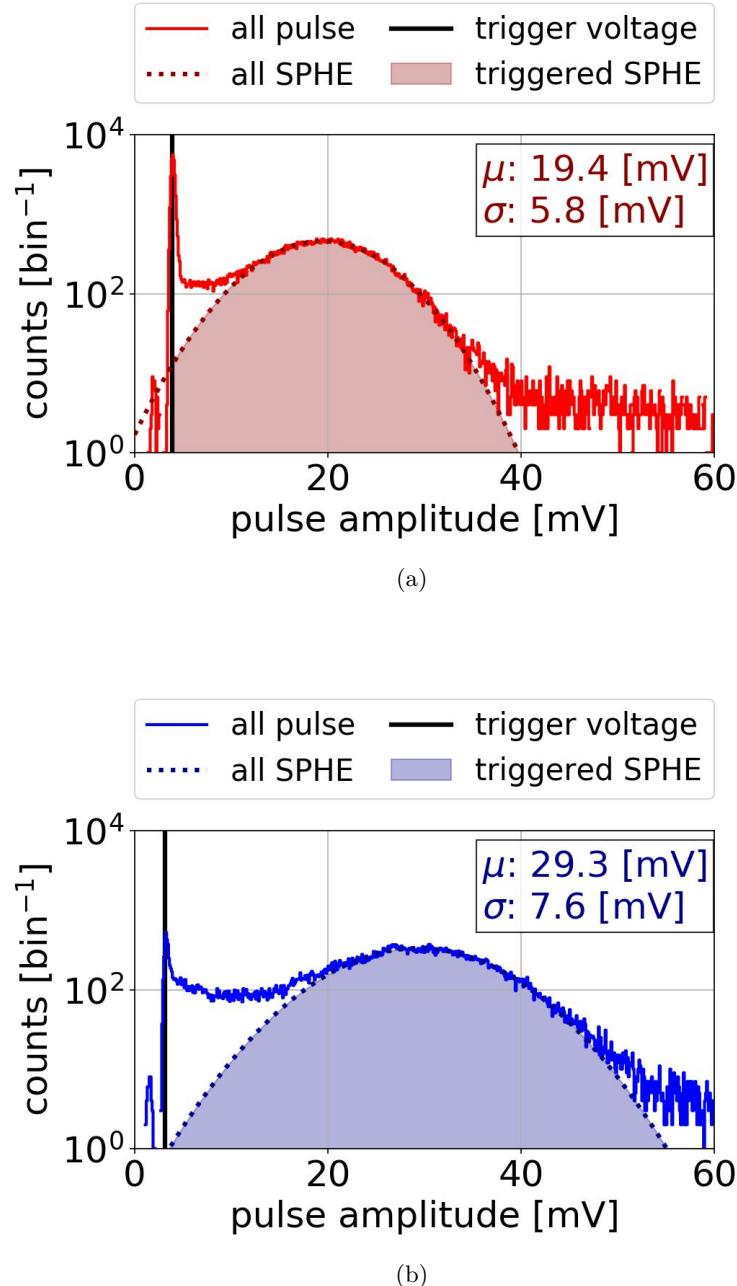


Figure 1.6: PMT pulse amplitude distribution: (a) top PMT (b) bottom PMT. Data were taken at 2018-03-12 11:41.

540 and  $\theta$  is the rotated angle.

541 The mean values for pulse area and pulse amplitude are  $\mu_x$  and  $\mu_y$ . The standard deviation  
 542 values for pulse area and pulse amplitude are  $\sigma_x \cos \theta - \sigma_y \sin \theta$  and  $\sigma_x \sin \theta + \sigma_y \cos \theta$ . Results of  
 543 these fits are shown in Fig. 1.7. Results from PMT calibrations are summarized in Table 1.4. Fitting  
 544 values of different dataset show an agreement within 1 % on the mean PMT single photon electron  
 545 pulse area and pulse amplitude.

546 The values of SPHE pulse amplitudes are approximately 20 mV for the top PMT and 30 mV for  
 547 the bottom. Thus, a naive estimation based on the dynamic range 1260 mV noted previously shows  
 548 the DAQ system allows approximately 60 SPHEs to be simultaneously recorded by the top PMT  
 549 without distortion of pulse shape, and 40 for the bottom PMT. This dynamic simultaneous photon  
 550 recording range is large enough for record electron emission signal without pulse shape distortion in  
 551 most situations.

552 Degrading of PMTs is not noticed during the run, even though the possibility of degrading of  
 553 PMTs is discussed in their manual (Ref. [1]). However, since this effect is not observed during the  
 554 tests. For consistency of studying, the same value for PMT SPHE pulse area is used through all the  
 555 studies.

556 There are two revisions of these values of SPHE pulse area. In revision 1 (Rev1), the values used  
 557 are 426 mV ns for the top PMT and 638 mV ns for the bottom PMT. This is from analyzing pulse  
 558 area on datasets taken with the detector filled with xenon gas and grid voltages  $V_T$  and  $V_B$  higher  
 559 than 0 kV. These datasets contains more multiple photon electron pulses and biased the estimation.  
 560 In revision 2 (Rev2), data taken at vacuum condition with grid voltages  $V_T$  and  $V_B$  at 0 kV are used.  
 561 The values used are 413 mV ns for the top PMT and 610 mV ns for the bottom PMT. Rev2 gives a  
 562 better estimation on SPHE pulse area. SPHE pulse area is noted as PHE below.

time	PMT name	trigger voltage [mV]	trigger efficiency	pulse amplitude [mV]	pulse area [mV ns]
2018-02-3 13:21	top	3.762	0.997	$19.4 \pm 3.3$	$413 \pm 132$
	bottom	3.103	1.000	$27.9 \pm 4.6$	$607 \pm 161$
2018-03-12 11:41	top	3.853	0.996	$19.3 \pm 3.5$	$411 \pm 130$
	bottom	3.130	1.000	$29.2 \pm 5.1$	$607 \pm 161$
2018-05-15 12:03	top	3.713	0.997	$19.4 \pm 3.5$	$413 \pm 131$
	bottom	3.091	1.000	$29.5 \pm 5.4$	$615 \pm 167$
adopted value (Rev1)	top	-	1	-	426
	bottom	-	1	-	638
adopted value (Rev2)	top	-	1	-	413
	bottom	-	1	-	610

Table 1.4: PMT SPHE calibration.

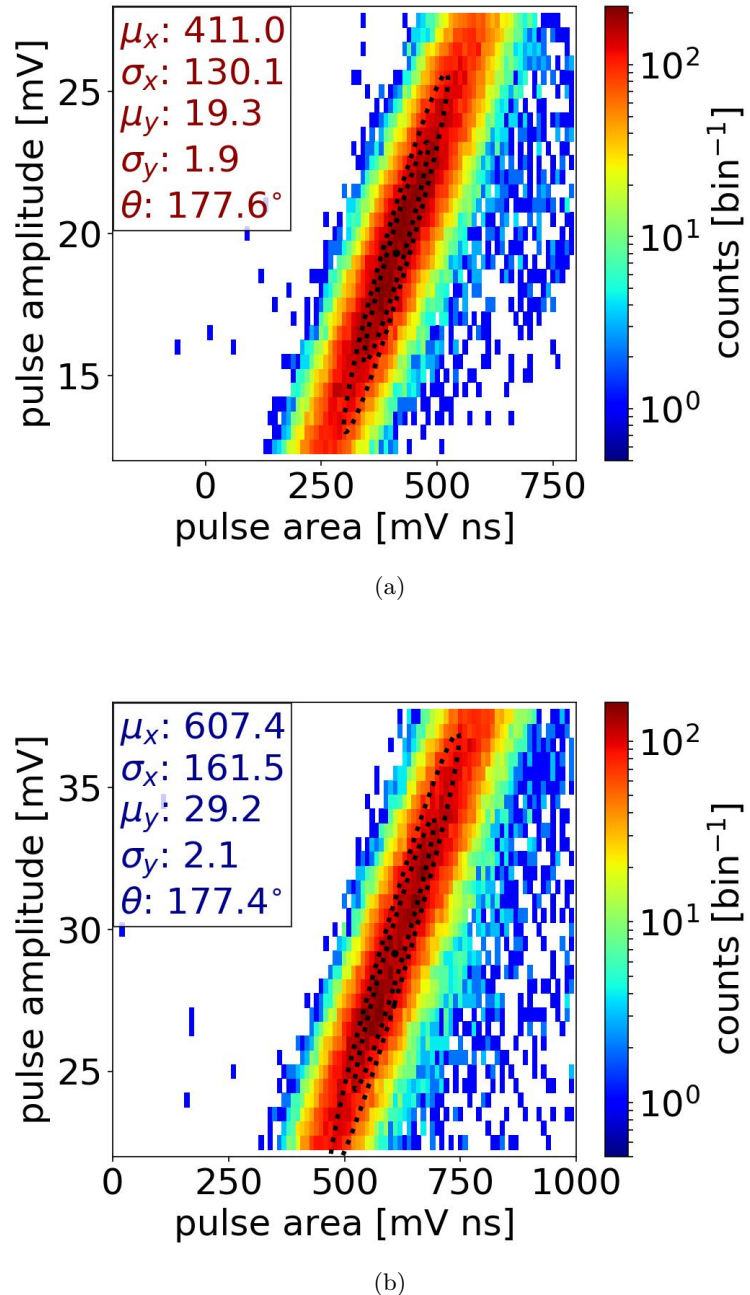


Figure 1.7: PMT SPHE pulse amplitude vs. pulse area distribution: (a) top PMT (b) bottom PMT. The black dot, and the dashed line are mean, 68 %, and 95 % contours of the Gaussian fits. Data were taken at 2018-03-12 11:41.

## 563 1.6 Light Collection

564 *Gas Test* studies event-based primary scintillation light and EL light. Light collection efficiency is  
 565 important to understand the overall sensitivity of the detector.

$$\text{light collection efficiency} = \frac{\# \text{ photoelectrons observed for an event}}{\# \text{ photon created during an event}} \quad (1.4)$$

566 Light collection efficiency includes geometric collection efficiency and PMT overall quantum effi-  
 567 ciency. Geometric collection efficiency describes the efficiency of photon propagation to reach PMT  
 568 photocathode surfaces, which includes photon propagation in the gas medium, photon reflection by  
 569 the detector material surfaces, and photon propagation in PMT window materials. PMT overall  
 570 quantum efficiency describes the efficiency of how many photons are absorbed by the photocathode  
 571 surfaces and turn into measurable current or voltage signals.

572 **Geometric collection efficiency** Geometric collection efficiency is studied by photon propaga-  
 573 tion simulation software Light Guide, as described in Ref. [5]. In the simulation software, a simplified  
 574 *Gas Test* detector boundary with cylindrical symmetry is drawn to represent the real detector ma-  
 575 terial surfaces. This simplified geometry includes the photocathode surfaces of PMTs, inner surfaces  
 576 of the PTFE cones, and surfaces of the grid rings. In addition, each grid is represented by two  
 577 planes of parallel wires with the same diameter and the same pitch distance as in the real detector.  
 578 The two planes are parallel to each other and close in distance to represent two distinct sets of  
 579 wires interlacing each other. Photon absorption and reflection, which takes into account the proba-  
 580 bility of specular reflection and Lambertian diffusion reflection, are simulated at material surfaces.  
 581 The empty space inside the simplified detector geometry is filled with a transparent or translu-  
 582 cent medium. The simulation of photon propagation through the medium includes scattering and  
 583 absorption effects.

584 The uncertainty of the reflectivity of detector surface materials has a major influence on the total  
 585 light collection. Among these materials, PTFE reflectivity has the largest uncertainty reported, the  
 586 value of which for xenon scintillation photons at room temperature are in the range of 0.4 to 0.75.  
 587 This difference in reflectivity may be a result of different fabrication processes or different material  
 588 density, as discussed in Ref. [6].

589 The geometric collection efficiency is evaluated as a function of  $(r, z)$  in the detector. To under-  
 590 stand geometric collection efficiency at one specific location,  $10^5$  to  $10^7$  simulations of single photons  
 591 are generated from this specific location. Each simulated photon is stepped either to transport  
 592 through the detector medium or to interact with the detector surface materials. Each simulation  
 593 ends when the simulated photon is absorbed by either the detector medium or detector surface ma-  
 594 terials. The counts of photons reaching PMT photocathode surfaces are used to estimate geometric

595 collection efficiency,

$$\text{Geometric collection efficiency} = \frac{\# \text{ photons reaching PMT photocathode surfaces}}{\# \text{ photons simulated}} \quad (1.5)$$

596 **PMT overall quantum efficiency** The overall quantum efficiency of a PMT includes (1) the  
 597 PMT photocathode quantum efficiency (QE), (2) the PMT electron collection efficiency, and (3) the  
 598 PMT electron gain.

599 The PMT photocathode QE is the probability per incident photon to produce a photoelectron.  
 600 For 175 nm xenon scintillation light, there is a ~20 % probability for 2 photoelectrons to be produced  
 601 rather one, so called the double photoelectron effect. We use the term photons detected (PHD) to  
 602 refer to the number of photons that produced at least one photoelectron. The term PHE refers to  
 603 the number of photoelectrons produced at the photocathode. The photocathode quantum efficiency  
 604 for the top and bottom PMTs, as quoted by Hamamatsu, are 36.3 % and 36.0 %, respectively, for  
 605 175 nm light, see Table 1.1. The Hamamatsu QE does not account for the double photoelectron  
 606 effect; that is, it is the average number of photoelectrons produced per incident photon, different  
 607 from the average number of photons that produce a measurable signal per incident photon.

608 PMT electron collection efficiency is the probability that these output photoelectrons land on the  
 609 effective area of the first dynode; the mechanism of how the PMT works is described in Section 1.1.  
 610 PMT electron collection efficiency depends on the mechanical design of a PMT and the voltage  
 611 difference between the PMT photocathode and the PMT first dynode. The exact value of electron  
 612 collection efficiency of the PMTs used in *Gas Test* at their operating voltage are not measured. We  
 613 estimate PMT electron collection efficiency to be 90 % based on measurement of other PMTs of the  
 614 same model at a higher PMT operating voltage, as described in Ref. [Lung2012 ].

615 PMT electron gain describes the multiplication process of the output photoelectrons in dynode  
 616 stages. The current that results from this multiplication process is translated to voltage using a  
 617  $50\Omega$  load resistor. The multiplication process amplifies the useful signal and eases the signal noise  
 618 selection. The voltage then is digitized by the DAQ, as described in Section 1.2. The digitized  
 619 voltage is the measured PMT signals. Observed signals are translated to units of PHE by dividing  
 620 out the mean SPHE area for each PMT. The coefficient of variation (CV, the ratio of the standard  
 621 deviation to the mean value) of PHE is ~30 %, as described in Section 1.5.

622 Therefore, to understand the spatial dependence of light collection efficiency in the ELD, we  
 623 start with 500 000 simulations of single photons every 5 mm in r and z dimension in the ELD, and  
 624 record the geometric collection efficiency of each location. This number is then multiplied by PMT  
 625 overall QE to obtain the total light collection efficiency. There are two light collection efficiency  
 626 estimation of two different grid wire configurations that we used for grid emission tests, labeled  
 627 grid configuration 1 (grid config. 1) and grid configuration 2 (grid config. 2). Run 4 to Run 9 use  
 628 grid configuration 1, and Run 10 to Run 17 use grid configuration 2. These two configurations are

629 identical everywhere else in the ELD except for the top grid wire pitches and diameters. Table 1.5  
630 and Table 1.6 summarize the parameters in the simulation.

parameter	grid config. 1 Run 4-9	grid config. 2 Run 10-17
top grid	wire pitch [mm] wire diameter [ $\mu\text{m}$ ]	2.5 100
bottom grid	wire pitch [mm] wire diameter [ $\mu\text{m}$ ]	2.5 75
top/bottom cone (PTFE reflector)	cylinder 1 height [mm] cylinder 1 radius (frustum larger radius) [mm] frustum height [mm] cylinder 2 radius (frustum smaller radius) [mm] cylinder 2 height [mm]	1.17 65 98.8 32 10
top/bottom PMT	photocathode radius [mm]	32

Table 1.5: Light collection simulation geometry parameters

parameter	value
Xe (gas)	refraction index
	Rayleigh scatter length [m]
	absorption length [m]
Quartz (synthetic quartz)	refraction index
PTFE	reflectivity
	specular reflection ratio
	Lambretian diffusion reflection ratio
SS (SS304)	reflectivity
	specular reflection ratio
	Lambretian diffusion reflection ratio

Table 1.6: Light collection simulation material parameters

631 As expected, the geometric collection efficiency varies at different locations in the ELD, which  
632 causes the light collection efficiency to vary, accordingly. The light distribution between the top  
633 and bottom PMT also varies across the ELD. This light distribution helps discriminate the location  
634 where events happened. We use top-bottom asymmetry (TBA) to describe this light distribution,  
635 which is defined as:

$$\text{TBA} = \frac{\text{Top PMT light collection} - \text{Bottom PMT light collection}}{\text{Top PMT light collection} + \text{Bottom PMT light collection}}. \quad (1.6)$$

636 Results in Fig. 1.8 show the light collection efficiency and the TBA in the ELD. Locations that  
637 are in the top cone region usually have a positive TBA, and locations that are in the bottom cone

638 usually have a negative TBA. TBA is close to zero in the EL region.

639 Among all different classes of events, our primary pulse of interest is electron emission events,  
640 which happen in the EL region. We estimate the light collection in this region with the same method  
641 mentioned before and finer binning. We start with 500 000 simulations of single photons every 2 mm  
642 in  $r$  dimension in the middle of the EL region. Results of the simulations are shown in Fig. 1.9.  
643 Light collection efficiency in the EL region falls away at  $r > 65$  mm, which is the inner radius of the  
644 PTFE reflector cones. The average top and bottom PMT light collection efficiencies in the EL region  
645 are  $\sim 0.0085$ . The average TBA in the EL region is  $\sim 0$ . The average total PMT light collection  
646 efficiency in the EL region is  $\sim 0.017$ . For most electron emission events in which photon production  
647 is larger than 300, an average number of  $\sim 5$  photoelectrons would be observed. Therefore, this light  
648 collection efficiency is sufficient to allow us to detect electron emission events.

649 The uncertainty of PTFE reflectivity has a large influence on the total light collection, which is  
650 shown in Fig. 1.10. Higher PTFE reflectivity results in a higher total light collection efficiency. The  
651 actual value of reflectivity of the PTFE reflector cones has not been measured directly. We estimate  
652 the actual PTFE reflectivity of xenon scintillation photons to be 0.4, according to the material  
653 density .

## 654 1.7 Light production

655 The ELD measures primary scintillation photons and electroluminescence photons in gas. First, I  
656 will introduce these two light production processes. Next, I will discuss the light production in noble  
657 gas, e.g. xenon, which is the medium that the ELD normally operates in.

658 **Primary scintillation** Primary scintillation is the process in which photons are created directly by  
659 energy deposition of external particle events. These photons have two sources: direct excitation, and  
660 excitation from recombination after ionization. An external particle travels through the medium in  
661 the ELD, transferring its energy to atoms in the medium, e.g. xenon, through exciting and ionizing  
662 these atoms. The excited atoms will return to their ground states by emitting photons of series  
663 energies corresponding to the energy level of the atoms, which is called relaxation of the excited  
664 atom. These photons from direct excitation from external particles are the first source of primary  
665 scintillation photons. The ionized atoms are not able to produce photons by themselves. However,  
666 they can recombine with the electrons around them and form excited atoms, which deexcite in a  
667 similar process as direct excited atoms, and emit photons simultaneously. These photons are the  
668 second source of primary scintillation photons. The quantity of second source of primary scintillation  
669 photons is dependent on the recombination process, which depends on properties of the atoms, and is  
670 influenced by the detector environment, especially the electric field (or reduced electric field) on the  
671 recombination site. A strong electric field forces electrons to quickly drift away from the ionization

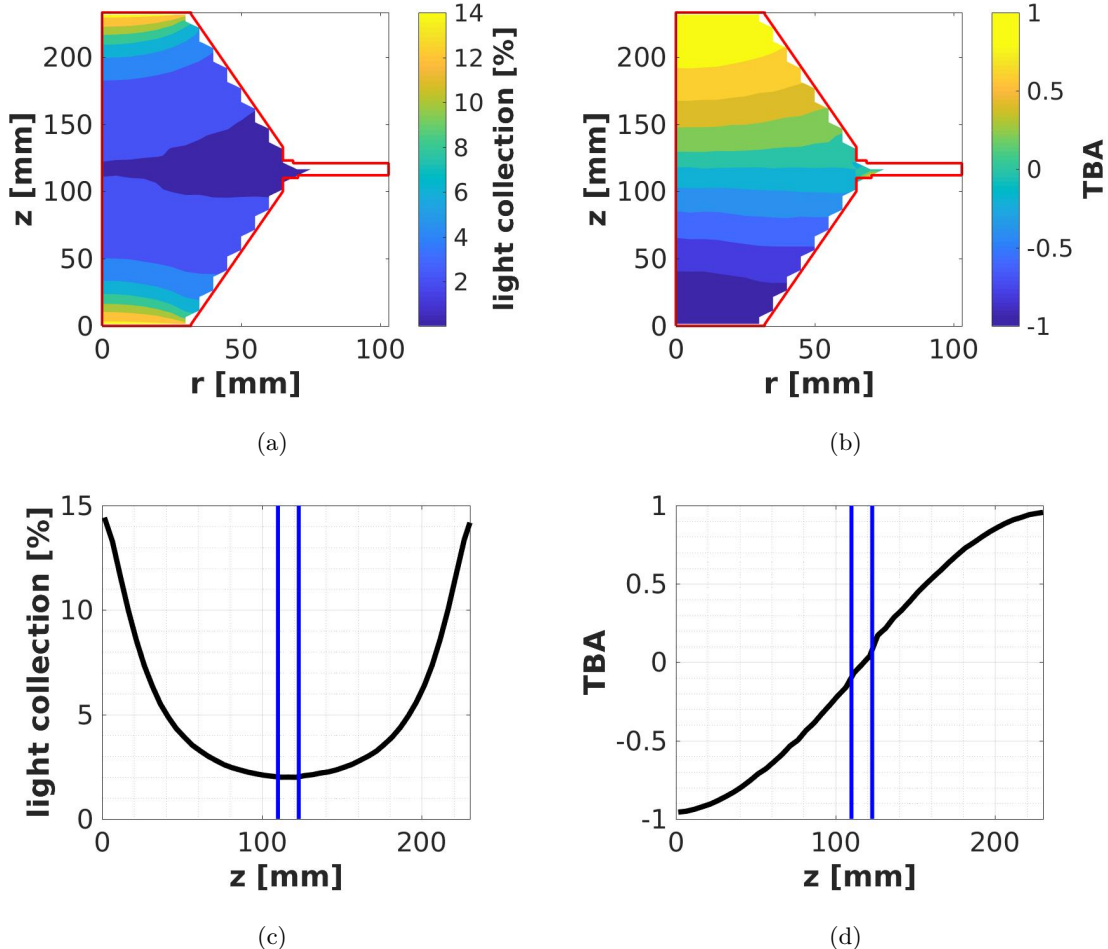


Figure 1.8: Light collection efficiency of  $(r, z)$  cross section in the ELD from simulation. (a) Total light collection efficiency. (b) Top-bottom asymmetry (TBA). (c) Total light collection efficiency at  $r=0$ . (d) TBA at  $r=0$ . The red solid curve is the edge of the active volume of the ELD. The blue solid curve is the edges of the EL region. This result uses configuration 1, PTFE reflectivity 0.40.  $z=0$  is at the bottom PMT photocathode surface.

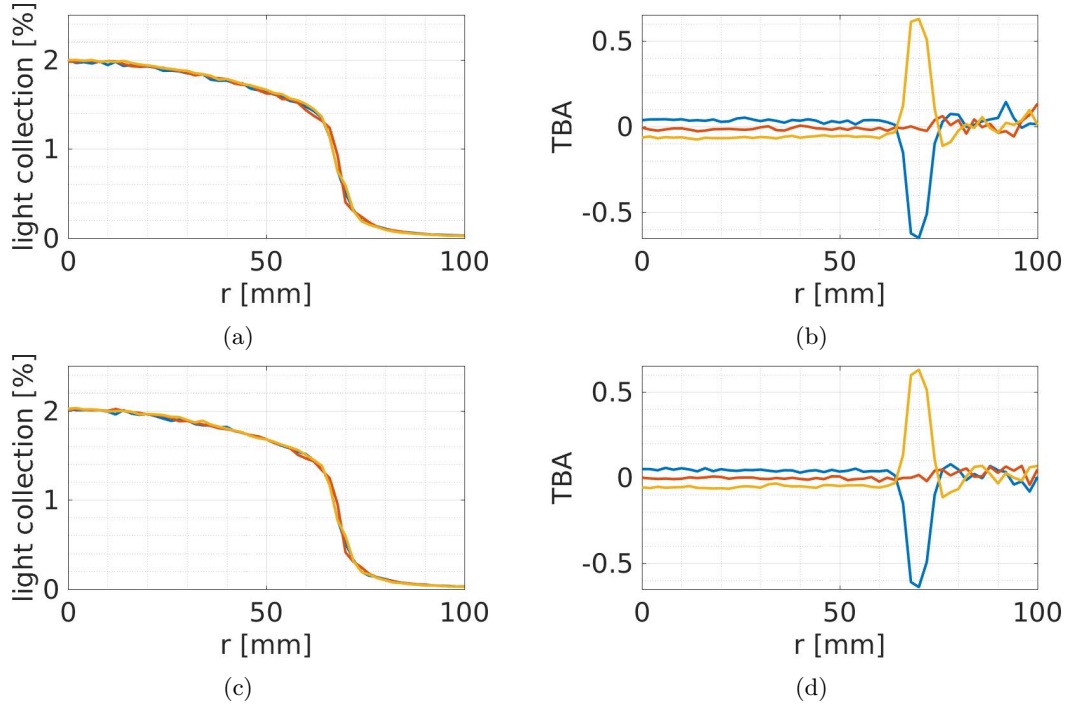


Figure 1.9: Light collection efficiency and TBA in the EL region in different grid configurations from simulation. (a) Total light collection efficiency in grid configuration 1. (b) TBA in grid configuration 1. (c) Total light collection efficiency in grid configuration 2. (d) TBA in grid configuration 2. The blue curve shows the value (light collection efficiency or TBA) as a function of  $r$  for fixed 2.09 mm below the top grid. The yellow curve shows the value as a function of  $r$  for fixed 2.09 mm above the bottom grid. The red curve shows the value as a function of  $r$  at the midpoint between the top and bottom grids. Light collection efficiency decreases and TBA has a sharp feature at  $r=65$  mm, which is the inner diameter of the PTFE reflector cones. This result uses PTFE reflectivity 0.40.

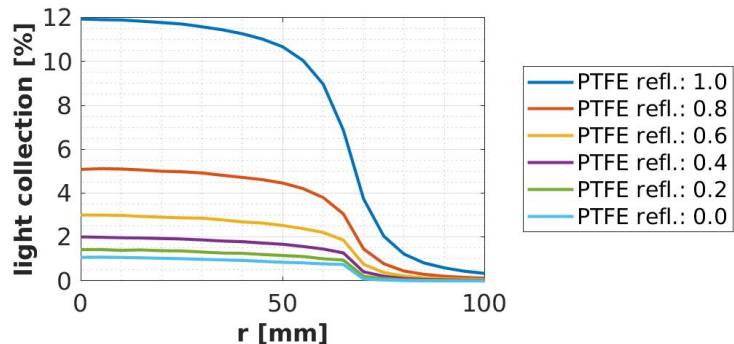


Figure 1.10: Light collection efficiency in the EL region with different PTFE reflectivity from simulation. Light collection efficiency decreases at  $r = 65$  mm, which is the inner diameter of the PTFE reflector cones. This result uses grid configuration 1.

672 site and reduce the probability of recombination, thus reducing the quantity of primary scintillation  
 673 light production.

674 **Electroluminescence** Electroluminescence (EL) is a phenomenon in which an electron drifts  
 675 through a strong electric field in a medium, collides with atoms in the medium, excites them which  
 676 will afterwards emit scintillation light. Since EL process is related to electrons in the medium, we  
 677 measure EL photons to study the electron production in the detector. The mechanism of EL is  
 678 similar to primary scintillation; the electron gains energy from drifting through the strong electric  
 679 field and simultaneously loses energy though exciting and ionizing medium atoms. Moreover, the  
 680 ionization process are usually associated with electron multiplication (gas gain), which creates more  
 681 electrons in the strong electric field region, and produces more EL scintillation light. The quantity of  
 682 EL scintillation photons and the probability of electron multiplication, are related to the strength of  
 683 reduced electric field of the medium. With proper strength of reduced electric field, EL can produce  
 684 more photons than primary scintillation. Because of its association with electrons and its production  
 685 quantity, EL photons are the most important signals measured in the ELD.

686 The primary scintillation photons are called S1, and the EL scintillation photons are called S2,  
 687 because the primary scintillation photons are produced earlier than the other photons created by  
 688 electroluminescence process of uncombined electrons. The same concepts of primary scintillation,  
 689 as well as S1 and S2, are also used in liquid noble detectors, as described in Chapter. ??.

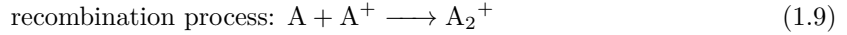
690 **Noble gas scintillation** For most noble gas atoms (A), e.g. neon, argon, krypton, and xenon, the  
 691 scintillation process usually forms an intermediate excited excimer state ( $A_2^*$ ). The emitted photons  
 692 from the intermediate excimer state are almost monoenergetic, e.g. 7.1 eV ( $\sim 175$  nm) in xenon, which  
 693 the medium is transparent to. Because of the existence of the intermediated excited excimer states, it  
 694 creates appreciable quantity of monoenergetic photons from the deexcitation of these states. These  
 695 features allow us to efficiently collect these monoenergetic photons with specialized devices, e.g.  
 696 PMTs, and use these photons to study reactions between external particles and medium atoms.

697 The chemical processes of scintillation are:



698 where A is the noble gas atom;  $A^*$  is the noble gas excited state;  $A_2^*$  is the excimer state;  $\gamma$  is  
 699 the monoenergetic photons from deexcitation of the excimers; and the low energy photons produced  
 700 during the process are not shown.

701 The chemical processes of recombination are:



702 where  $A^+$  is the noble gas ionized state;  $A_2^+$  is the ionized dimer state; and the low energy photons  
 703 produced during the process are not shown. The recombination process then leads to same channels  
 704 as the primary scintillation, with monoenergetic photons as the output signals. These photons,  
 705 combined with photons from direct excitations, make primary scintillation light. The quantity of  
 706 the monoenergetic photons is related to the reaction energy between external particles and medium  
 707 atoms, and properties and physical environment of the medium (especially medium density and  
 708 electric field).

709 These two primary scintillation processes happen fast in xenon, the duration of which is dom-  
 710 inated by the excimers decay time. The excimers can be separated to two types, the singlet state  
 711 ( ${}^1\sigma_u^+$ ,  ${}^3\sigma_u^+$ ) and triplet state ( ${}^3\sigma_u^+$ ,  ${}^1_u$ ), with separate decay times. The singlet state and the  
 712 triplet state are known to be created from a three-body deconstruction of noble gas atom excited  
 713 state  ${}^2P_{1/2}$  state and  ${}^2P_{3/2}$  state, which has a different initial quantity from the event. Because  
 714 these creation processes are three body reactions, the creation rate of the these two states have  
 715 strong dependence on the gas density of atoms. The decay time of both of these two states have  
 716 a dependence on the gas density, as described in Ref. [8]. Some other materials also show that the  
 717 decay time is very different between liquid noble gas and very dense noble gas. The decay time for  
 718 the singlet state and the triplet state in liquid xenon are 4.3(6) ns and 22.0(20) ns, as measured in  
 719 Ref. [9]. For dense xenon with pressure in the range of 2.7 atm to 32 atm, the decay time for singlet  
 720 states varies from 15(3) ns to 5.5(10) ns. The decay time for triplet state is 96(5) ns in the same  
 721 pressure range.

722 **think about should I take about ionization/scintillation ratio here?**

723 EL photons in gaseous xenon from the energy-loss of fast-moving electrons are one of the most  
 724 important signals that we measure. This EL process is driven by the electrons gaining energy in the  
 725 electric field. This chemical process is,



726 in which a electron directly excite a xenon atom. These excited-state atoms ( $A^*$ ) then deexcite  
 727 through the same chemical process as Eqn.1.7, Eqn.1.8 and emitted EL photons at a similar energy  
 728 as scintillation photons.

729 The EL reduce photon production quantity (ratio of photon production quantity to gas density)  
 730 per electron trajectory length of direct excitation is found to have a linear dependence on the reduced

<sup>731</sup> electric field ( $E_s/N$ ), as described and summarized in Ref. [Santos1994, Fonseca2004, 10, 11]:

$$\frac{dL_s}{dx} = a \frac{E_s}{N} + b, \quad (1.13)$$

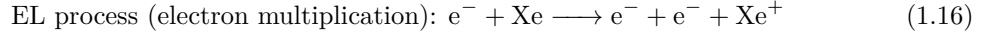
<sup>732</sup> where  $L_s$  is the reduced photon production quantity;  $x$  is the electron trajectory length;  $E_s$  is  
<sup>733</sup> the electric field strength (at the scintillation site);  $N$  is the density of gas;  $a$  and  $b$  are constant  
<sup>734</sup> parameters, which are measured in Ref. [Fonseca2004, 11] to be:

$$a = 0.137(2) \text{ photon electron}^{-1} \text{ V}^{-1}, \quad (1.14)$$

$$b = -4.7(1) \times 10^{-18} \text{ photon cm}^2 \text{ electron}^{-1} \text{ atom}^{-1}. \quad (1.15)$$

<sup>735</sup> The measurement also suggests that EL light is typically not produced below 3.4 Td<sup>1</sup>, which is  
<sup>736</sup> referred as the EL threshold.

<sup>737</sup> The EL process is usually associated with simultaneous electron multiplication. This process  
<sup>738</sup> describes an electric accelerated by electric field, collides with gas molecules, ionize them generating  
<sup>739</sup> additional free electrons. The chemical process is,



<sup>740</sup> The probability of electron multiplication per electron per unit length is also quoted as the first  
<sup>741</sup> Townsend ionization coefficient ( $\alpha$ ), which depends on the strength of reduced electric field, as mea-  
<sup>742</sup> sured in Ref. [Kruithof1940, Derenzo1974]. Conventionally, reduced first Townsend ionization  
<sup>743</sup> coefficient is measured with  $E/p_0$  instead of reduced electric field, where  $E$  is the electric field;  $p_0$  is  
<sup>744</sup> pressure of the gas reduced to 0 °C. The reduced first Townsend ionization coefficient  $\eta \equiv \alpha/E$  is also  
<sup>745</sup> frequently used. The measured reduced first Townsend ionization coefficient is shown in Fig. 1.11.

<sup>746</sup> The duration of EL process is related electron drift velocity ( $v$ ), which also depends on reduced  
<sup>747</sup> electric field ( $E/n$ ), as measured in Ref. [English1953, Pack1962, Brooks1982, Berghofer2004,  
<sup>748</sup> 12]. In the range of 5 Td to 25 Td, a naive linear fit from Ref.[Brooks1982] shows in xenon,

$$v [\text{mm } \mu\text{s}^{-1}] \approx 0.556E/n [\text{Td}] \quad (1.17)$$

<sup>749</sup> Therefore, xenon is a good scintillation medium for its quantity of photon production and its  
<sup>750</sup> transparency to these photons. With its well characterized quantities, we chose it as the major  
<sup>751</sup> operating medium for the ELD.

---

<sup>1</sup>A Townsend, or Td, is defined as 1 Td =  $10^{-21} \text{ V m}^2 = 10^{-17} \text{ V cm}^2$ .

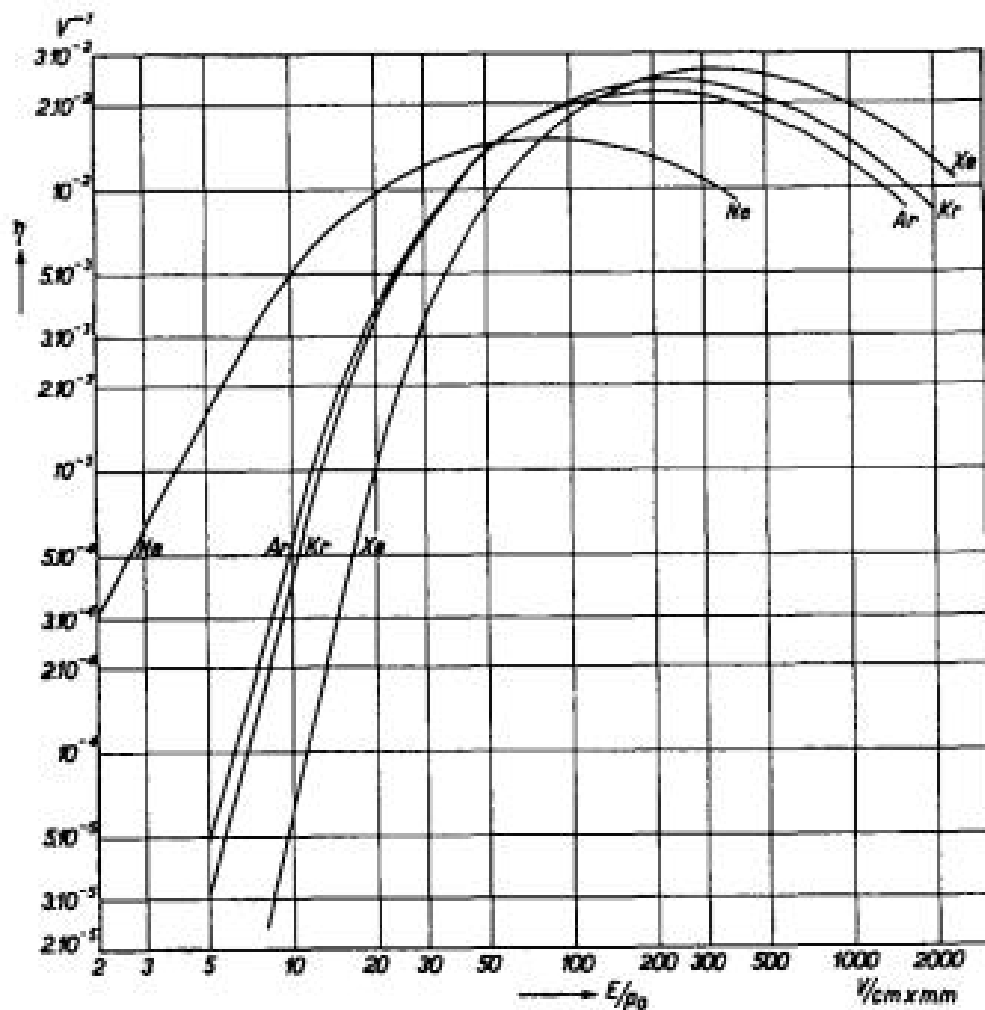


Figure 1.11: The reduced first Townsend ionization coefficient  $\eta \equiv \alpha/E$  for neon, argon, krypton, and xenon, from Ref. [Kruithof1940].

## 752 1.8 Signals

753 Signals, PMT photon pulses that we record, are the fundamental elements of to understand detector  
754 activities. A variety of process can give rise to signals in the detector. Based on their source origin,  
755 signals are separated to four different categories:

- 756 • electron emission (from both the grid wires and grid rings)
- 757 • particle radiation from radioactive materials (both inside and outside the ELD),
- 758 • cosmic ray,
- 759 • and other miscellaneous sources, which includes:
  - 760 – electronic noise (from the electrical ground of the building and other powered devices,  
761 e.g. the KNF circulation pump.)
  - 762 – PMT dark current,
  - 763 – PMT afterpulsing,
  - 764 – PTFE cone reflector fluorescence,
  - 765 – Cherenkov radiation (created in the PTFE cone reflectors and the PMT windows when  
766 a charge particle, most likely an electron or a muon, passes through),
  - 767 – discharge, as in a short-lived plasma in the medium, i.e., breakdown.

### 768 1.8.1 Electron emission

769 Electron emission signals, especially those from the grid wires, are our signals of interest. A cartoon  
770 for the physical process and an example waveform of electron emission signal are shown in Fig. 1.12.  
771 An electron leaves the cathodic electrode from various types of emission processes. After the elec-  
772 tron left the wire surface, the high electric field around the cathodic wire will quickly energize the  
773 electrons. The high energy electron ionizes and excites the atoms around it. This process in which  
774 more drifted electrons are produced is called electron multiplication; since in this particular case, it  
775 happens near the cathodic electrode, it is also called cathodic gas gain. In this region, more EL light  
776 is produced per unit time compared to a lower electric field region. This is the cause of the “peak”  
777 at the beginning of the electron emission signal. Then, these electrons drift to the anodic electrode  
778 because of the operation voltage difference between the two grids. EL light is produced along this  
779 drift. This correspond to the majority of EL light seen in the electron emission signal. There is a  
780 clear start and stop time for the electron emission signal. Duration of the electron emission signal is  
781 roughly the duration of this drift. After this, drifted electrons get close to the anodic electrode. Since  
782 the electric field around the anodic wires are also high, drifted electrons also go through a similar  
783 electron multiplication process, which is also called anodic gas gain. This process also creates more

784 electrons and a higher production rate of EL light. This is the cause of the “peak” at the ending of  
 785 electron emission signal. The peak at the end of the signal is lower than the peak at the beginning of  
 786 the signal. This is because of dispersion of the arrival times of drifted electrons on anodic electrode.  
 787 This dispersion is because of the different microscopic trajectory each drifted electron takes to reach  
 788 the anodic electrode. Different arrival times of the drifted electrons cause the final increment of EL  
 789 light production from different electrons do not happen coincidentally. This lowers the height of the  
 790 peak at the ending of the electron emission signal. Another reason for the different height of the  
 791 peak is because the electric field on the anodic wire is smaller than cathodic wire with regard to the  
 792 wire diameter of the anodic wire are larger, thus resulting in a smaller production of EL light.

793 Of the features described above, the most important features of the electron emission signal is  
 794 the EL duration. The other signal shape features including the early and late gas gain peaks are not  
 795 apparent because the light collection efficiency is not high enough. The EL duration is approximately  
 796 equal to the duration of electron drift between the two electrodes. The deviation of electric field  
 797 between the two electrode is much smaller than the average value of it. So the drift duration can be  
 798 roughly estimated by,

$$\text{drift duration} = \frac{\text{distance between two electrodes}}{\text{drift velocity at the average electric field between two electrodes}} \quad (1.18)$$

799 The other important feature of the electron emission signal is the quantity of its EL production.  
 800 EL light production in the majority part of electron emission signal is uniform, except for the  
 801 beginning and the ending of the signal. Since the electron multiplication around the cathodic wires  
 802 happens early in the process before the major era of EL light production, the total counts of photons  
 803 created in an electron emission signal can be estimated as,

$$\# \text{ EL photons} \approx \# \text{ EL photons per drifted electron} \times \text{cathodic gas gain}. \quad (1.19)$$

804 We will estimate the number of EL photons per drifted electron and the cathodic gas gain below.

805 The number of EL photons per drifted electron and the cathodic gas gain are related to the  
 806 reduced electric field in the EL region and surface reduced electric field on the cathodic wire. The  
 807 value of both reduced electric field can be derived from the gas density and the electric field, which  
 808 can be estimated from the operation voltage, wire diameter and wire pitch of the two grid. The  
 809 electrostatic solution of the electric field in the ELD is solved by COMSOL, as described in Ap-  
 810 pendix ???. The results of the electric fields in the EL region (drift fields) and the average surface  
 811 electric fields vs.  $\Delta V_{T-B}$  are shown in Fig. 1.13a. Because of the grid has a woven pattern, the  
 812 surface electric field in the middle of the wire between two woven knots are higher than average  
 813 by  $\sim 16\%$ , which is also discussed in Appendix ???. The average photon yield per EL distance is a  
 814 known function of reduced electric field, as discussed in Section 1.7.

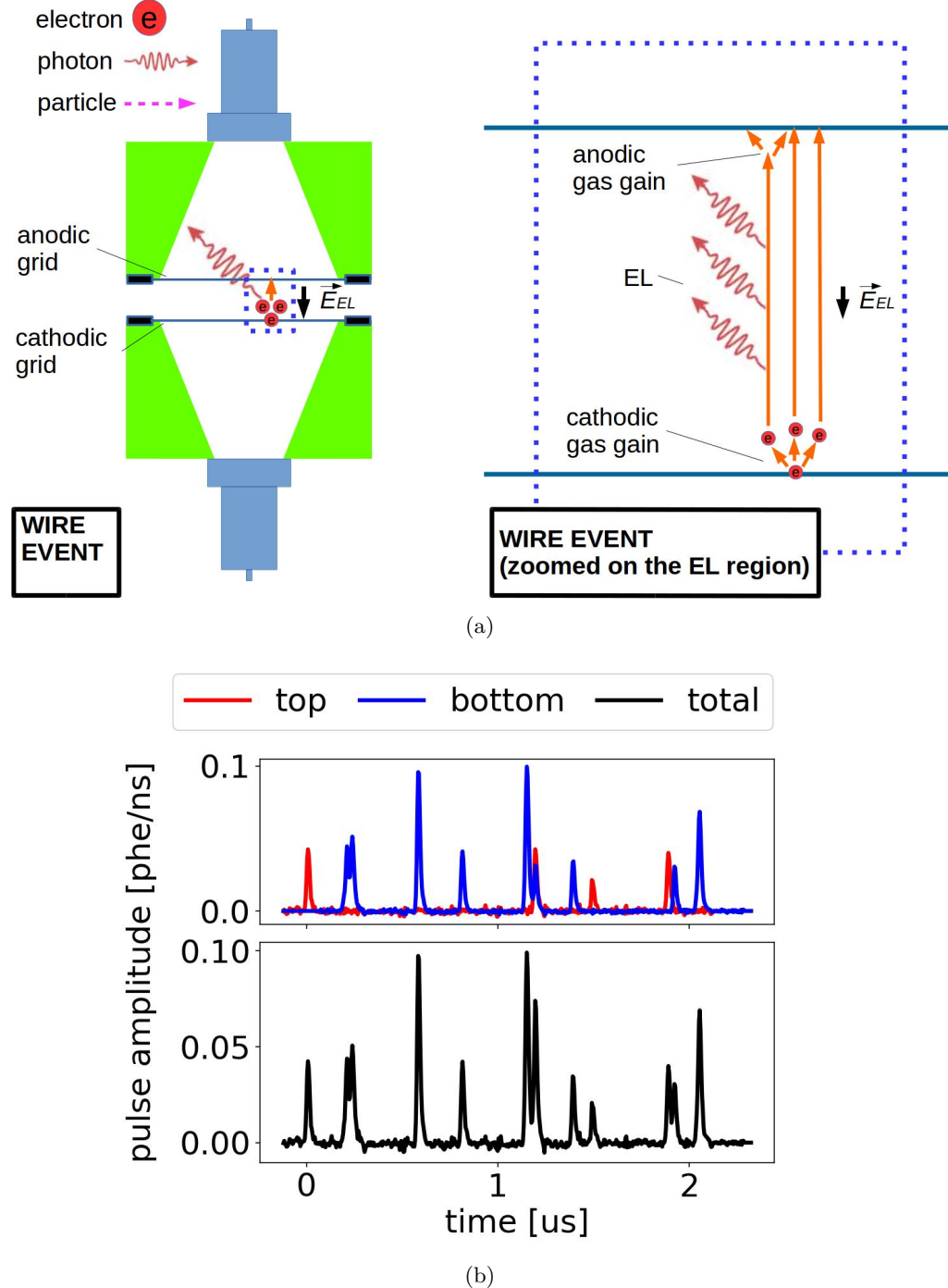


Figure 1.12: *Gas Test* electron emission event from grid wires. (a) Cartoon of the process. (b) An example waveform. Data were taken at 2017-12-8 14:02, with grid voltages  $V_T$  and  $V_B$  at +6 kV and -6 kV, operating gas density at  $0.137 \text{ mol L}^{-1}$ . See text for details.

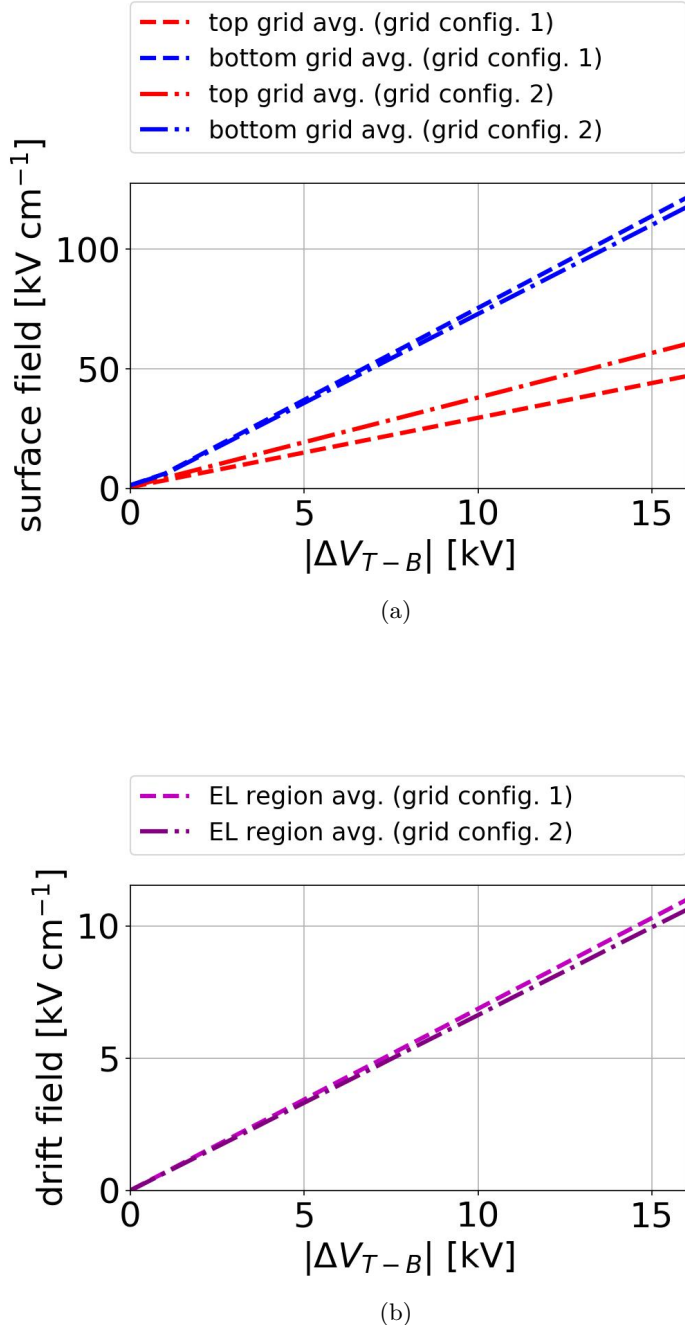


Figure 1.13: *Gas Test* detector electric field. (a) *Gas Test* wire surface electric field vs.  $\Delta V_{T-B}$  for the top and bottom grid in different grid configurations. (b) *Gas Test* EL region drift electric field vs.  $\Delta V_{T-B}$  in different grid configurations.

With the known surface reduced electric field, electron multiplication (cathodic gas gain) is studied using gas simulation softwares. A simple geometry is build and meshed in GMSH, as described in Ref. [13]. This software is capable of defining 3D finite element mesh, which interfaces with softwares like ElmerSolver and Garfield++ to solve the electric field in a defined geometry. Fig. 1.14a shows the defined geometry. This geometry includes a thin cylinder surface in the center representing the grid wire as the electron emission surface, and a thick cylinder surface outside representing the cut off distance of electron multiplication. The cut off distance is chosen to be sufficiently long so that the electric field beyond this distance is too small to allow significant electron multiplication. The diameter of the two cylinders are  $75\text{ }\mu\text{m}$  and 1 cm. Voltages are assigned to two cylinders to create a chosen electric field on the surface of the wire. Then, the electric field map in this full geometry is solved by Elmer, as described in Ref. [14, 15]. The gas simulation under such electric field map is done with Magboltz in Garfield++ interface, as described in Ref. [16, 17]. These softwares implement light yield and charge yield, aka the photon and electron production, for electrons moving in gas medium as a function of reduced electron field. By including the electric field map, choosing the corrects gas density, these softwares simulate the photon and electron production with an electron that initiate from the wire surface.

An example of electron multiplication simulation in the simple geometry is shown in Fig: 1.14b. As the electron moves further away from the wire surface, both light production and electron production reduce. Results of the counts of electron multiplication vs. surface electric field at different gas density is shown in Fig. 1.15. The number of collected EL photons of the electron emission signal signals are shown in Fig. 1.16. Together with the EL duration, the number of collected EL photons are the important features of electron emission signal signals that we used in the signal classification.

Therefore, electron emission signals have a known EL duration, and EL photons production dependence on the detector operating gas density and  $\Delta V_{T-B}$ . We use these two important appearance to distinguish electron emission signals in the future signal classification.

### 1.8.2 Particle radiation

Particle radiation is the high energy particle originating from radioactive decay of unstable atoms in materials inside and outside the detector. The high energy particle enter the detector and deposit energy there through different processes. A high energy photon (gamma radiation) loses energy through thermal elastic scattering, photoelectric process, Compton scattering, and other particle energy loss processes; A high energy charged particle, e.g. electron (beta radiation),  ${}^4_2\text{He}$  (alpha radiation), predominately loses it energy through ionizing atoms in detector materials, as described in Ref. [18]. These processes produce excited xenon atoms and free electrons thus producing primary scintillation and EL photons. The primary scintillation photons (S1) are collected and seen immediately. The free electrons, on the other hand, drift according to the electric field in the detector,

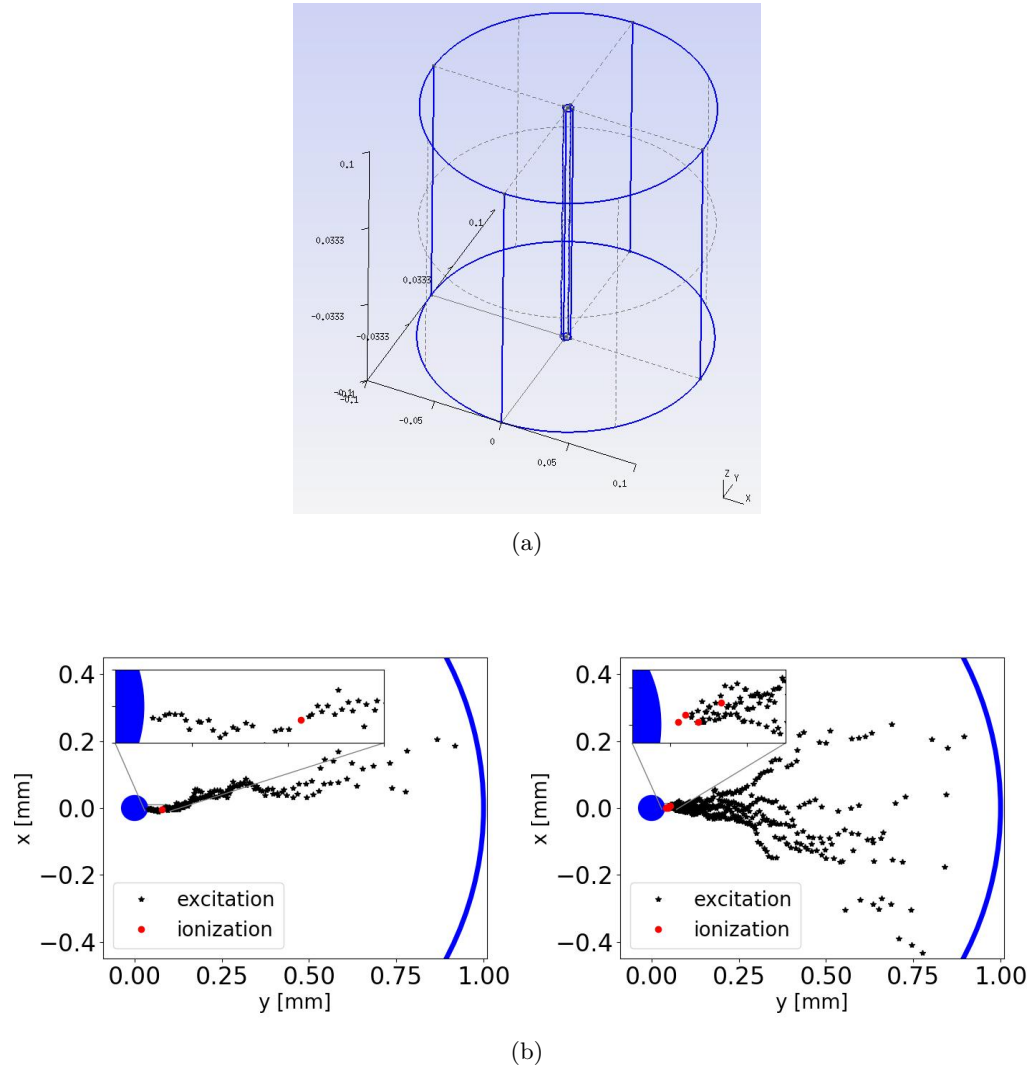


Figure 1.14: A 3D simulation of an electron drifting in an axial symmetric electric field in xenon gas. (a) Geometry defined in GMSH (unit in cm) [13]. Electrons are emitted at one point from the wire in the center. (b) Example simulation results, which is taken at operating gas density  $0.137 \text{ mol L}^{-1}$  ( $T = 295 \text{ K}$ ,  $P = 3.3 \text{ bara}$ ), showing the excitation and ionization sites. The blue curves are the boundary of the outer edge of simulation (diameter : 2 mm) and the wire surface (diameter:  $75 \times 10^{-3}$  mm). Left: a simulated event with a single ionization site. Right: a simulated event with four ionization sites. This simulation is conducted with Elmer and Garfield++, as described in Ref. [14–17].

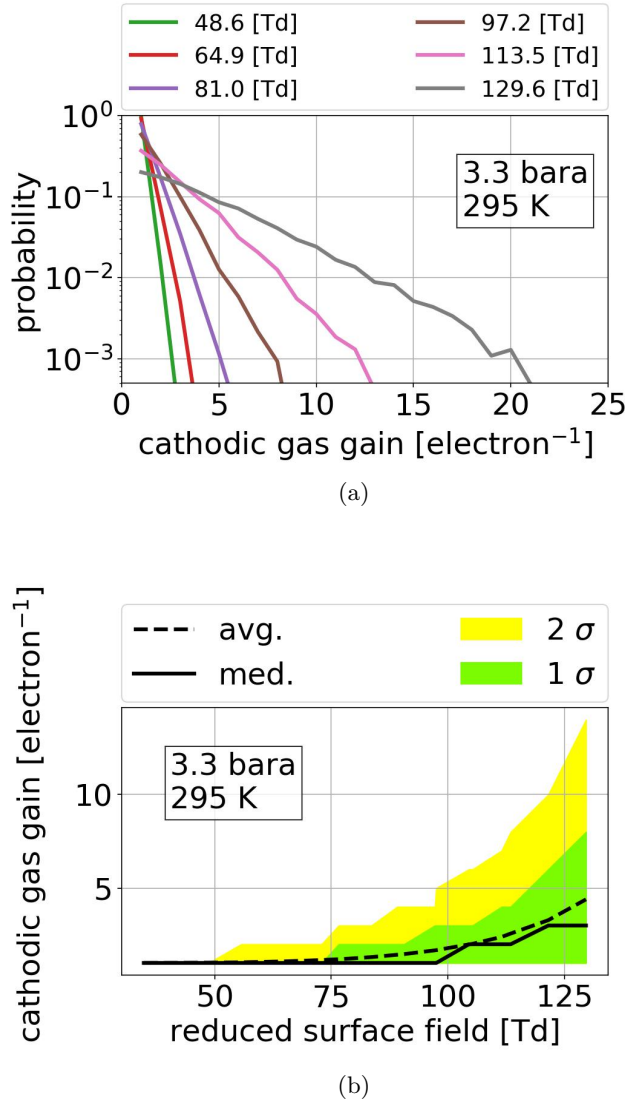


Figure 1.15: Simulated cathodic electron gas gain vs. reduced surface electric field. (a) Simulated cathodic gas gain probability distribution in different reduced surface electric fields. (b) The average, median,  $1\sigma$  band (15.9 % to 84.1 %), and  $2\sigma$  band (2.3 % to 97.7 %) of cathodic gas gain vs. the reduced surface electric field. Simulation is taken at operating gas density  $0.137 \text{ mol L}^{-1}$  ( $T = 295 \text{ K}$ ,  $P = 3.3 \text{ bara}$ ).

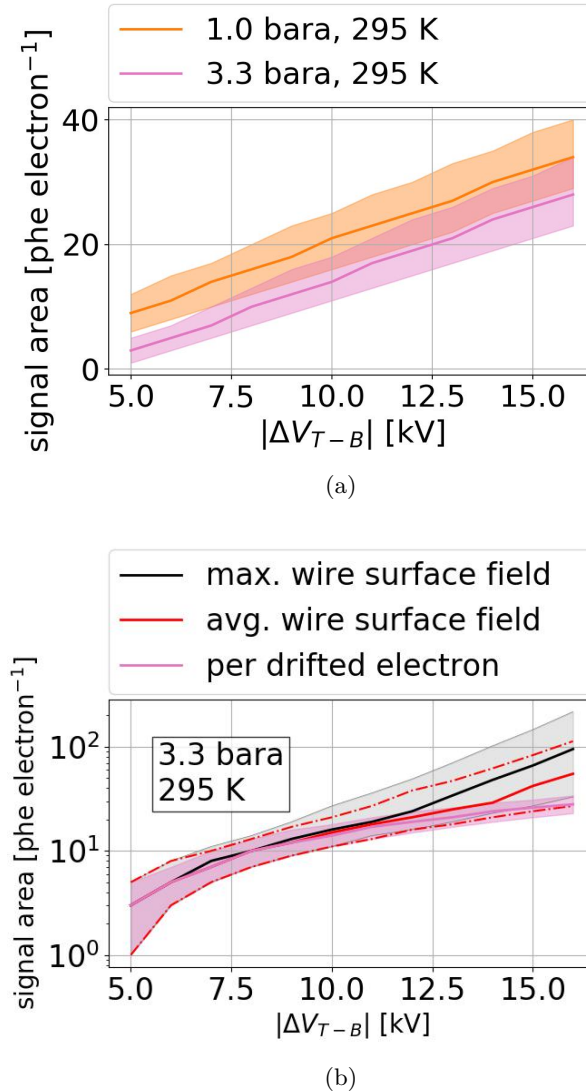


Figure 1.16: Simulated signal areas vs.  $\Delta V_{T-B}$ . (a) Simulated signal area of a single drifted electron from the bottom grid at different gas densities. (b) Simulated signal area of an electron generated at different locations on the bottom grid. The black line corresponds to locations with maximum electric field on the grid. The red line corresponds to locations with average electric field on the grid. The green line shows the simulated signal area of a single drifted electron. Simulation is taken at operating gas density  $0.137 \text{ mol L}^{-1}$  ( $T = 295 \text{ K}$ ,  $P = 3.3 \text{ bara}$ ). The solid lines are the medians. The dashed lines, color shaded bands are  $1\sigma$  bands (15.9 % to 84.1 %), respectively.

851 produce different signals.

852 A high energy gamma event can enter the ELD since its energy loss in detector skin materials is  
 853 small. The photon attenuation length, which characterizes how far a photon can go, usually decrease  
 854 as we have denser materials, higher average atomic mass in the materials, and lower incident particle  
 855 energy. The photon attenuation length in xenon is shown in Fig. 1.17. Along photon attenuation,  
 856 high energy electrons can be produced from gamma radiation through some kind of energy loss  
 857 process, like Compton scattering, Auger electron emission. These high energy electrons can be  
 858 produced inside the ELD, deposit its energy, and raise signals in the detector. The energy deposition  
 859 length depends on the material, especially its density and its average atomic mass, and the energy  
 860 of the incident particle. Similar to the photon attenuation process, denser material, higher average  
 861 atomic mass, and lower incident particle energy usually results in smaller energy deposition length.  
 862 The energy deposition length in xenon is shown in Fig. 1.18. For an electron with energy in the range  
 863 of 10 keV to 1000 keV, which is the common energy for beta radiation, the continuous slowing down  
 864 approximation range (CSDA range), also known as the average path length traveled by the charged  
 865 particle (electron), is in the range of  $6 \times 10^{-4} \text{ g cm}^{-2}$  to  $1 \text{ g cm}^{-2}$ , corresponding to  $1 \times 10^{-5} \text{ cm}$  to  
 866  $2.0 \times 10^{-2} \text{ cm}$  with xenon gas density at  $0.137 \text{ mol L}^{-1}$  ( $18.0 \times 10^{-3} \text{ g cm}^{-3}$ ). The number of free  
 867 ionization electrons in this event is associated with the energy-loss of the incident particle. During  
 868 the measurement, a population associated with xenon K shell X-ray ( $K_\alpha$ : 29.8 keV,  $K_\beta$ : 33.6 keV,  
 869 from Ref. [Dulieu2007, TabRadv8]) is observed to be one of the byproduct of particle radiation  
 870 energy loss process, confirming that this type of signal is associated with external radiation.

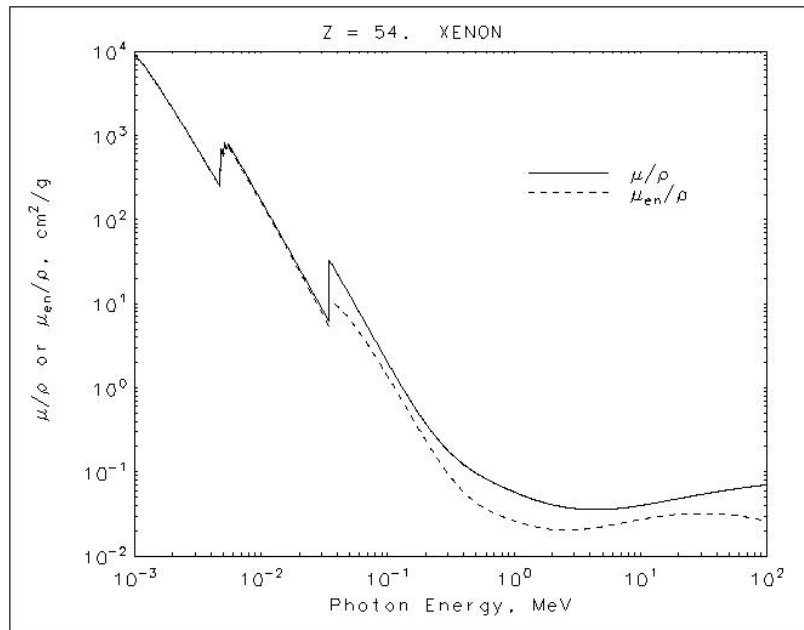


Figure 1.17: Attenuation length of photon in xenon, from Ref. ??.

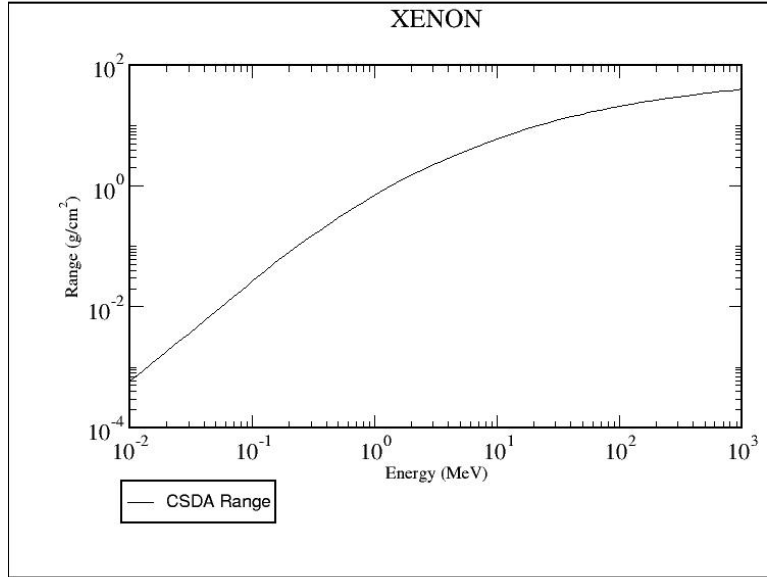


Figure 1.18: CSDA range of electrons in xenon, from Ref. ??.

871        A high energy external beta radiation, however, is less likely to enter the ELD compared to high  
 872        energy gamma radiation because the beta radiation penetration length (approximate to the material  
 873        CDSA range) is shorter than gamma radiation. Since the electron CDSA range is small compared  
 874        to the thickness of xenon gas skin outside the ELD, with addition stopping power from dense PTFE  
 875        reflector cone, the beta radiation would be stopped before it enters the ELD.

876        According to the location of energy deposition site, the high energy particle from radiation  
 877        produce different look of signals, which will be discussed separately.

878        **Anode cone event** Anode cone events are the particle radiation events which have energy de-  
 879        position location in the PTFE reflector cone close to the anodic grid side (anode cone). A cartoon  
 880        of the physical process and an example waveform of anode cone event, as well as two zoomed plots  
 881        of the waveform in different parts of the process, are shown in Fig. 1.19. The cartoon part A in  
 882        Fig. ?? shows an external particle entering the anode cone region and deposit energy there. This  
 883        process produce scintillation photons, the signal of which are collected and seen immediately, shown  
 884        in Fig. 1.19c. The primary scintillation signal normally has a TBA (top-bottom asymmetry) heavier  
 885        in the anode side PMT than the cathode side, indicating this photon signal is produced in the anode  
 886        cone (top cone in this case). The free electrons drift to the anodic grid according to the electric  
 887        field in the anode cone . Even though the electric field in the cone region is too small to produce  
 888        large quantity of EL light during electron drift, when these electrons get close to the anodic grid  
 889        wire, the electric field around the anodic grid wires are big enough to produce EL light. This is the

890 source of the secondary photon signal, which follows the preceding signal after the amount of time  
 891 that it took electron to drift. The cartoon part B in Fig. 1.19a shows this process, and Fig. 1.19d  
 892 shows the corresponding part of the signal. The pulse shape of the secondary photon signals has a  
 893 comparably slower rising and falling edge at the beginning and the ending of it. It also has a higher  
 894 TBA because EL around the anode wire primarily happens above the anodic wire. The bottom  
 895 PMT is in the shadow of grid wires when the top PMT is not. This difference causes a ratio of  $\sim 2$   
 896 increment on light collection ratio between the top PMT and the bottom PMT. These characteristic  
 897 signatures are useful for veto large-area anode cone events. However, when their signal area get  
 898 smaller (probably because of a lower energy deposition of external particles), it becomes difficult to  
 899 find these signals by their shape. Therefore, a signal selection based on preceding signal is conducted  
 900 to find the secondary signal from the primary scintillation signal. The time separation between these  
 901 two signal is estimated by the known measured electron drift velocity in gaseous xenon, as described  
 902 in Ref. ???. Electron drift velocity in gaseous xenon is approximately  $0.556 \text{ mm } \mu\text{s}^{-1} \text{ Td}^{-1} \text{ E/N}$  for  
 903 reduced electric field (E/N) in the range of 5 Td to 25 Td. The maximum separation time for this  
 904 detector at xenon gas density  $0.137 \text{ mol L}^{-1}$ , top grid voltage  $V_T$  in the range of +4 kV to +8 kV is  
 905 approximately  $85 \mu\text{s}$  to  $75 \mu\text{s}$ . The value of this maximum separation time decreases as decreasing  
 906 the operation pressure in the detector. The value of maximum separation time drives the choice of  
 907  $100 \mu\text{s}$  preceding signal selections of this type of signals.

908 **Cathodic cone event** Cathode cone events are the particle radiation events which have energy  
 909 deposition location in the PTFE reflector cone close to the cathodic grid side (cathode cone). A  
 910 cartoon of the physical process and an example waveform of cathode cone event are shown in  
 911 Fig. 1.20. Similar to anode cone events, this process produce scintillation photons. However, the  
 912 ionization electrons produced drift to cathode PMT. Therefore, EL light typically is produced during  
 913 along their trajectories because the electric field in such region is much lower than the EL threshold.  
 914 The primary scintillation signal normally has a TBA heavier in the cathode side PMT than the  
 915 anode side PMT, indicating this photon signal is produced in the cathode cone (bottom cone in this  
 916 case), as expected.

917 **S1 S2 event in the cathode corner** S1 S2 events in the cathode corner (cathode corner events)  
 918 are the particle radiation events which have energy deposition location either outside EL region and  
 919 very close to the cathodic grid or in the corner between the cathodic grid and the cathodic cone.  
 920 A cartoon of the physical process and an example waveform of cathode corner event are shown in  
 921 Fig. 1.21. Similar to anode cone events, this process produce scintillation photons, which is shown  
 922 in Fig. 1.21a (left) and the waveform of which is shown in the first  $0.3 \mu\text{s}$  in Fig. 1.21b. Since the  
 923 free electrons produced in this event is really close to the cathode grid, according to electrostatic  
 924 study using COMSOL software described in Ref. [19], these electrons drift to cathodic grid, pass  
 925 it, then drift in the EL region, the process of which produces EL photons along the trajectories of

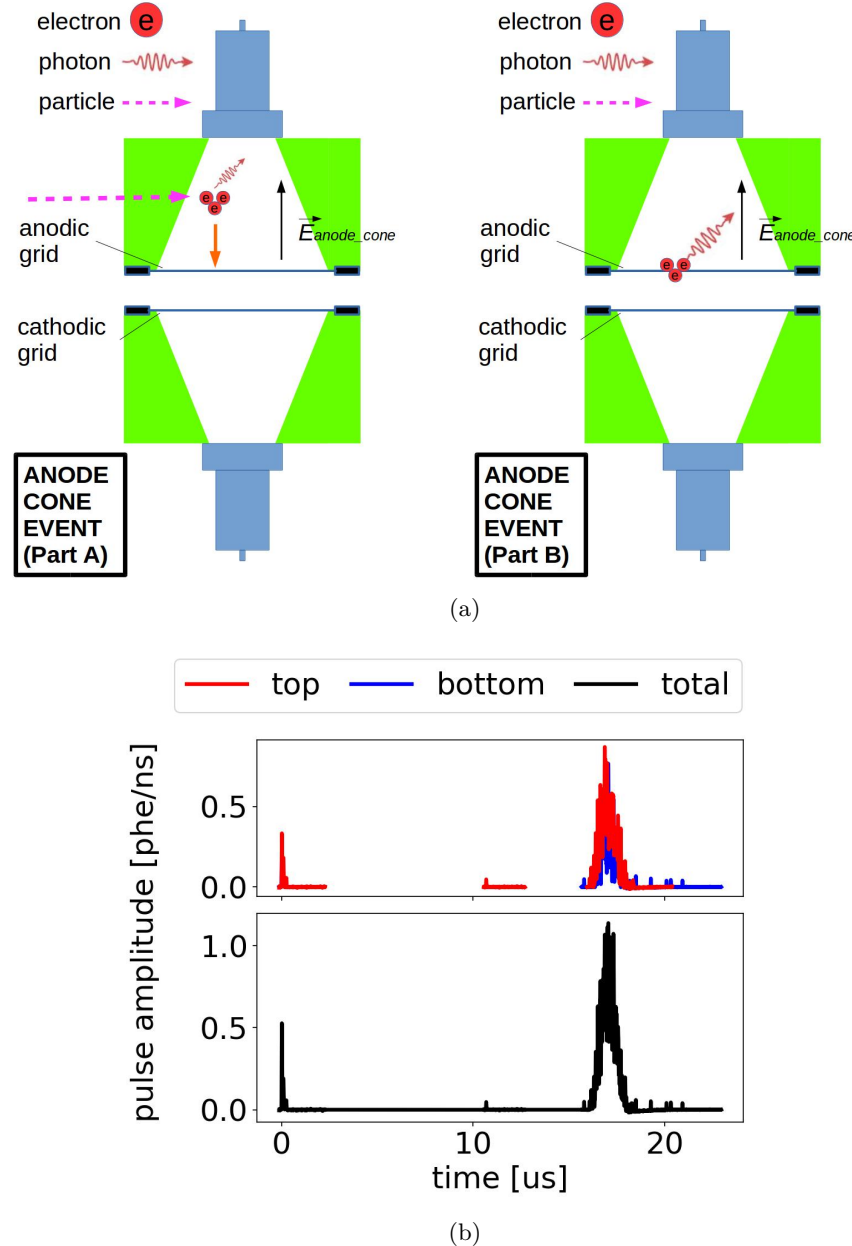


Figure 1.19: *Gas Test* signal: anode cone event. (a) Cartoon of the process. Left: Primary scintillation light ionization electrons are produced from the particle interaction, and the ionization electrons drift to the anodic grid (part A). Right: EL light is produced in the high electric field region around the anodic grid wires (part B). (b) An example waveform of an anode cone event. Data were taken at 2017-12-8 14:02, with grid voltages  $V_T$  and  $V_B$  at +6 kV and -6 kV, operating gas density at  $0.137 \text{ mol L}^{-1}$ .

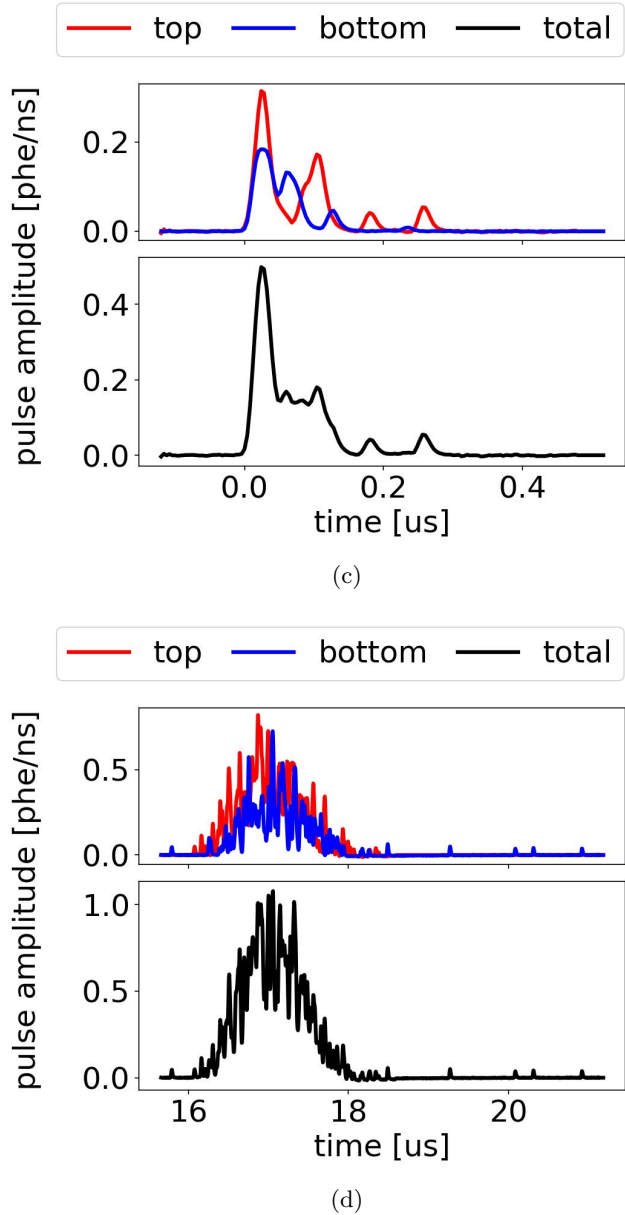


Figure 1.19: *Gas Test* signal: anode cone event (cont.). (c) An example waveform of an anode cone event, zoomed in the range of  $0 \mu\text{s}$  to  $0.5 \mu\text{s}$ , which shows the primary scintillation light (cartoon part A). (d) An example waveform of an anode cone event, zoomed in the range of  $15 \mu\text{s}$  to  $21 \mu\text{s}$ , which shows the EL light produced around the anodic grid wires (cartoon part B).

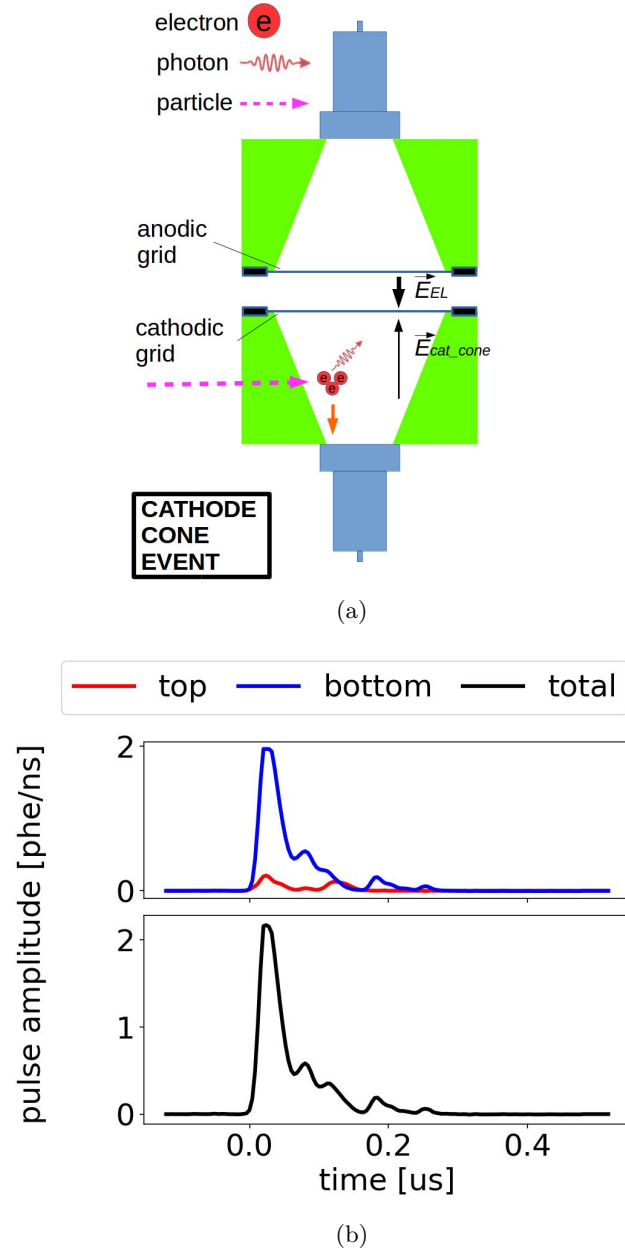


Figure 1.20: *Gas Test* signal: cathode cone event. (a) Cartoon of the process. Primary scintillation light ionization electrons are produced from the particle interaction, and the ionization electrons drift toward the bottom PMT. EL light is typically not produced along the trajectories of the electrons because the electric field in such region is lower than the EL threshold. (b) An example waveform of a cathode cone event. Data were taken at 2017-12-8 14:02, with grid voltages  $V_T$  and  $V_B$  at +6 kV and -6 kV, operating gas density at  $0.137 \text{ mol L}^{-1}$ .

the electrons, and finally land on the anodic grid. This EL light production process is illustrated in Fig. 1.21a (right), which corresponds to the waveform after  $0.5\ \mu\text{s}$  in Fig. 1.21b. The static electric field from COMSOL solution is shown in Fig. 1.22. Both the primary scintillation signal and the secondary EL signal has a balanced TBA, indicating these photon signals are produced either in or really close to the EL region.

**S1 S2 event in the EL region** S1 S2 events in the EL region (EL region events) are the particle radiation events which have energy deposition location either in EL region. The process and an example waveforms is shown in Fig. 1.23. Since the electrons are produced in the energy deposition location in the EL region, these electrons drift in the EL region toward the anodic grid, producing EL photons. The duration of these signals are shorter compared to the electron emission signals because of the shorter drift length. The total quantity of photon production in this type of events is usually higher than that of an electron emission event, an anode cone event, and a cathode cone event, because of the free drifted electrons inside the EL region.

**High photon count events** High photon count events are those particle radiation events that are extremely high on energy, therefore producing plenty primary scintillation photon, free drifted electrons, and EL photons during the events. The photon production rate is so high that it exceeds the digitizing ability of the DAQ system (also called saturate the DAQ), causing distortion on waveform recording thus resulting in difficulty of signal classification. These signals may have various origins. Some of these signals have comparable or shorter duration than electron emission signals, two example waveforms are shown in Fig. 1.24 and Fig. 1.25. These events might be related to the EL region events, described in Section 1.8.2, or grid wire radiation and ring radiation, which are the particle radiation events originated from radioactive elements in grid wire and ring materials.

The radioactive elements in the ring material can be both from the impurities in the material, e.g.  $^{238}\text{U}$ ,  $^{232}\text{Th}$ , and  $^{235}\text{U}$  and from the absorption of air on the material surfaces, e.g.  $^{222}\text{Rn}$ . Among these sources, air radon absorption draw the most concern because of its abundance. The decay activity of radon induced radiation plating per unit of surface area per unit of time ( $RA_{\text{Rn-rad}}$ ) is estimated as,

$$RA_{\text{Rn-rad}} = RV_{\text{Rn}} h_{\text{eff}} T_{\text{exposure}} \frac{1}{\tau_{\text{eff}}} \quad (1.20)$$

where  $RV_{\text{Rn}}$  is the radon decay activity in the air per unit of volume per unit of time;  $h_{\text{eff}}$  is the effective height of radiation plating, in which the radon decay daughter nuclei will plate on material surface;  $T_{\text{exposure}}$  is the exposure time of plating; and  $\tau_{\text{eff}}$  is the effect decay time constant of radon decay daughter nuclei. With regard to  $RV_{\text{Rn}} 48\ \text{Bq m}^{-3}$ , from Ref. [20],  $h_{\text{eff}} \sim 1\ \text{m}$ ,  $\tau_{\text{eff}} \sim 32\ \text{yr}$ , from the decay time constant of  $^{210}\text{Pb}$ , the typical daughter nucleus from the radon decay, in Ref. [Dulieu2008], and  $T_{\text{exposure}} 1\ \text{d}$ ,  $RA_{\text{Rn-rad}}$  is  $\sim 4 \times 10^{-3}\ \text{Bq m}^{-2}$ . For a  $\sim 40\ \text{cm}^2$  grid wire

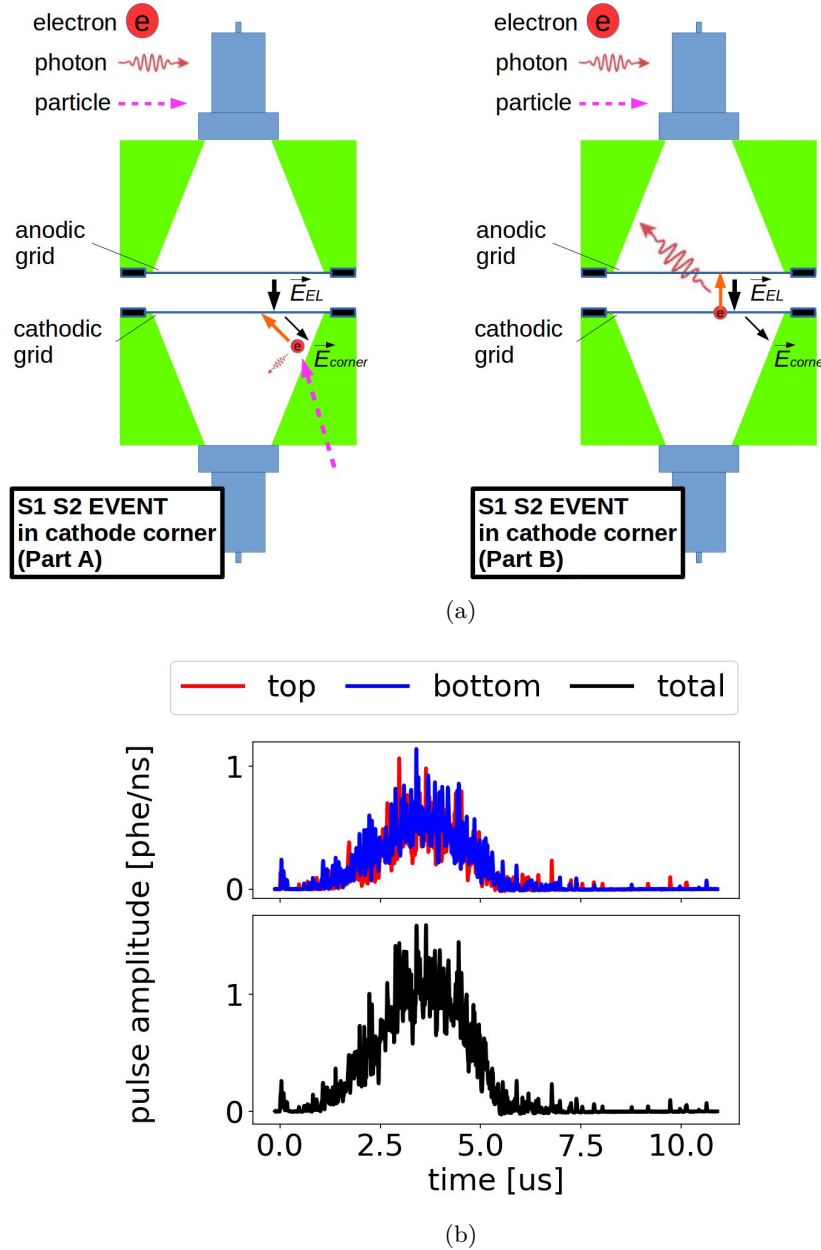


Figure 1.21: *Gas Test* signal: S1 S2 event in the cathode corner. (a) Cartoon of the process. Left: Primary scintillation light and ionization electrons are produced from the particle interaction, and the ionization electrons drift to the cathodic grid (part A). Right: EL light is produced in the EL region during electrons drifting to the anodic grid (part B). (b) An example waveform of an S1 S2 event in the cathode corner. Data were taken at 2017-12-8 14:02, with grid voltages  $V_T$  and  $V_B$  at +6 kV and -6 kV, operating gas density at  $0.137 \text{ mol L}^{-1}$ .

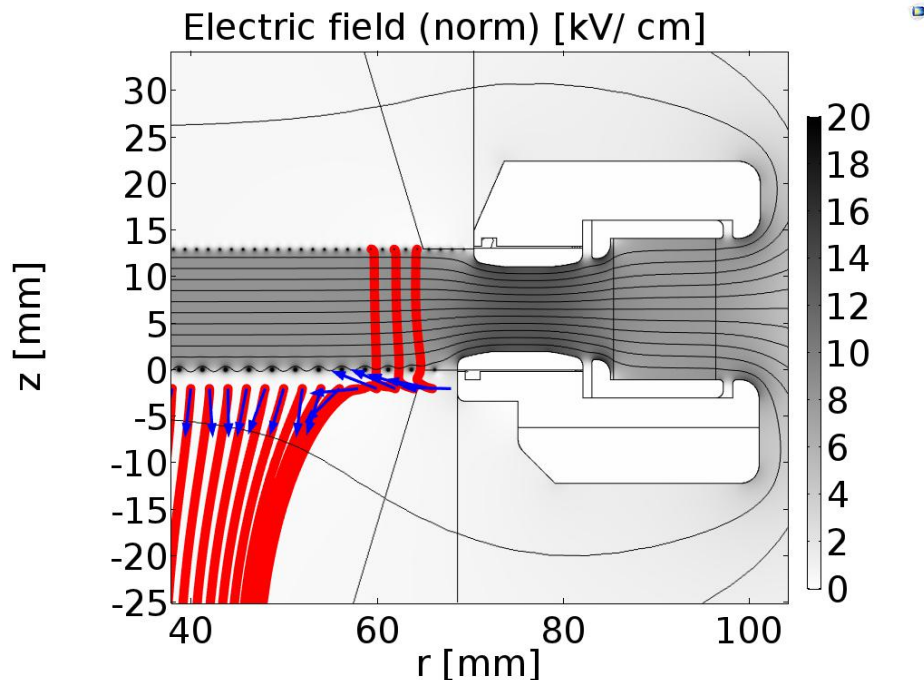


Figure 1.22: Electrostatic solution of the *Gas Test* detector (grid ring region). This result is solved with grid voltages  $V_T$  and  $V_B$  at +6 kV and -6 kV using COMSOL. The white metal structures in the middle of the figure are the cross sections of the grid rings. The contours show the electric potential; the color scales show the norm of electric field; the blue arrows shows the directions of the initial electron drift; the red lines shows the trajectory of electrons that start drifting at 2 mm below the bottom grid: electrons starting at  $r < 60$  mm drift downward, when electrons starting at  $r > 60$  mm drift into the EL region (cathode corner event).

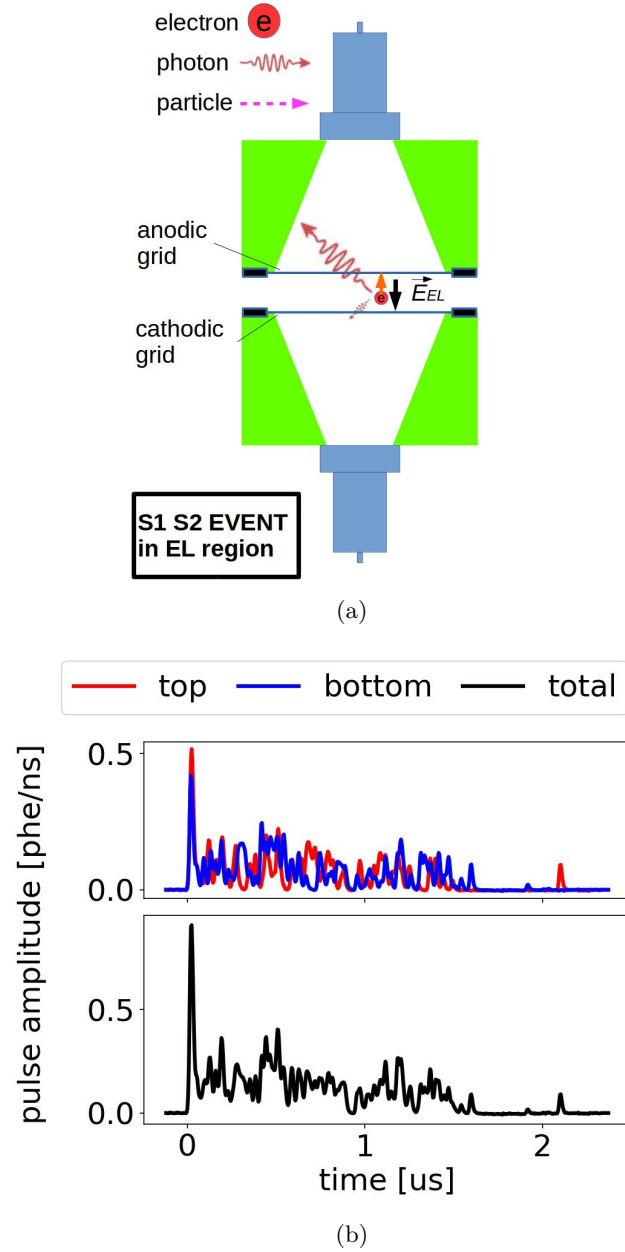


Figure 1.23: *Gas Test* signal: S1 S2 event in the EL region. (a) Cartoon of the process. Primary scintillation light and ionization electrons are produced from the particle interaction. The primary scintillation light and the EL light start to be produced simultaneously. (b) An example waveform of an S1 S2 event in the EL region. The primary scintillation light lies on top of the EL light. Data were taken at 2017-12-8 14:02, with grid voltages  $V_T$  and  $V_B$  at +6 kV and -6 kV, operating gas density at  $0.137 \text{ mol L}^{-1}$ .

<sup>959</sup> and grid ring total surface area, The total decay activity of radon induced radiation from the ring surface is  $\sim 10^{-5}$  Bq. These event rates should be relatively rare compared to other processes.

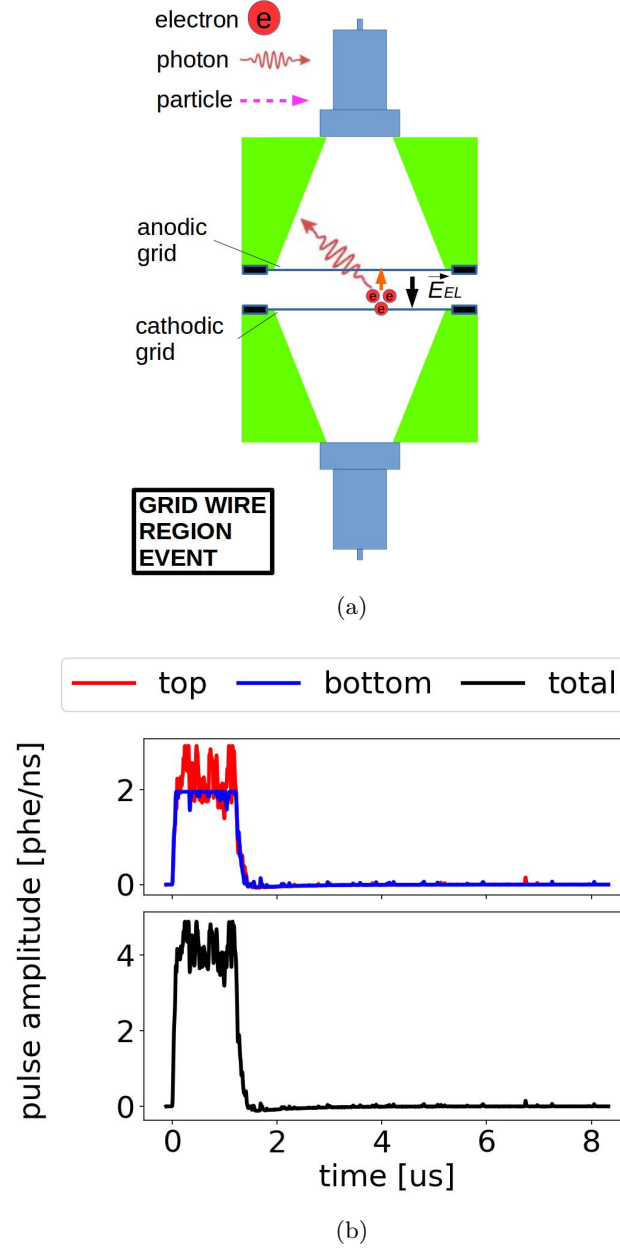


Figure 1.24: *Gas Test* signal: grid wire region event. (a) Cartoon of the process. (b) An example waveform. This might be an S1 S2 event in the EL region between the grid wires, when the primary scintillation light is clipped off because the signal amplitude exceeds DAQ dynamic range (PMT saturation). Data were taken at 2017-12-8 14:02, with grid voltages  $V_T$  and  $V_B$  at +6 kV and -6 kV, operating gas density at  $0.137 \text{ mol L}^{-1}$ .

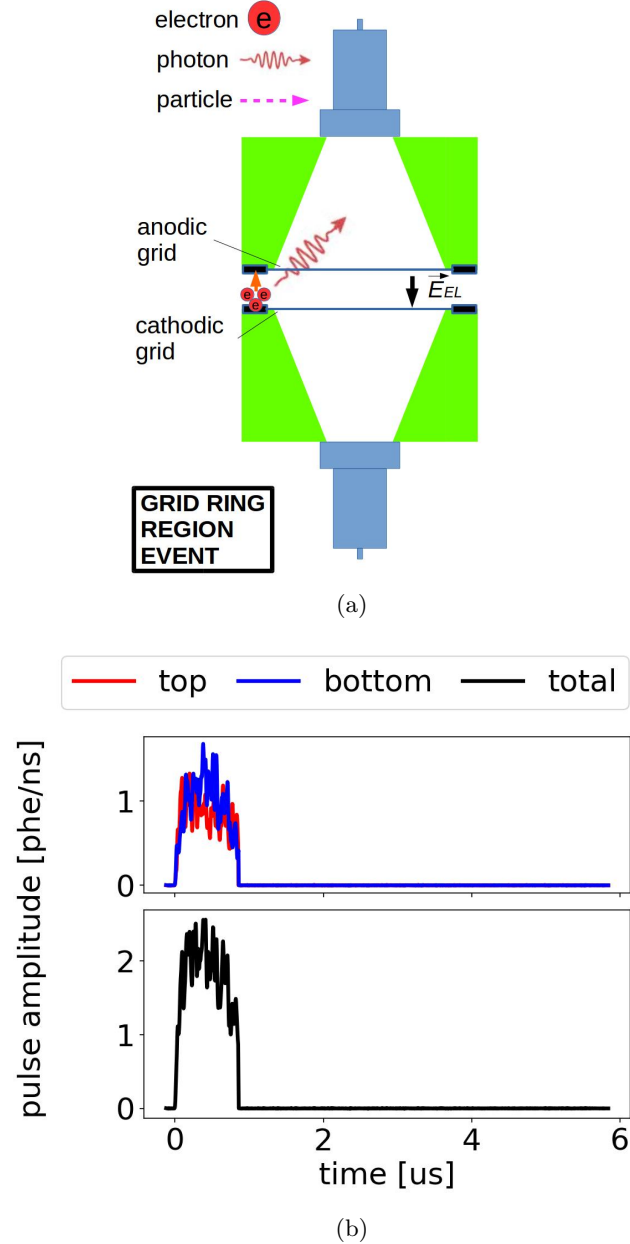


Figure 1.25: *Gas Test* signal: grid ring region event. (a) Cartoon of the process. (b) An example waveform. This might be an S1 S2 event in the EL region between the grid rings, when the primary scintillation light is not visible because the light collection efficiency is poor in this region. Data were taken at 2017-12-8 14:02, with grid voltages  $V_T$  and  $V_B$  at +6 kV and -6 kV, operating gas density at 0.137 mol L<sup>-1</sup>.

**Multiple scattering events** Multiple scattering events are those with more than one energy deposition location. The common source of these events are a high energy gamma radiation, since it can travel far distance in the detector. The multiple scattering events usually are combinations of the previous mentioned type of events. Two example waveform are shown in Fig. 1.26: the first one is a multiple scattering event in the anode cone region; the second one is a multiple scattering event in the anode cone region and the EL region.

### 1.8.3 Cosmic ray

Cosmic rays, originating outside Earth, are capable of producing showers of secondary particles that reach the *Gas Test* detector and giving rise to signals in the detector. Among all secondary particles that raise signals, muons are the most common one because of their abundance and high penetration length in earth atmosphere. Unlike alpha, beta, and gamma particle radiation, a cosmic ray muon has a longer ionization trajectory which travels crossing the whole detector.

The long ionization trajectory leads to a large quantity of primary scintillation light and free electron production, which results in a large light production. The minimum stop power of muon is  $1.255 \text{ MeV g}^{-1} \text{ cm}^2$  in xenon, from Ref. [21]. In xenon gas, the reported average energy to produce a primary scintillation photon ( $W_{\text{sci}}$ ) and electron-ion pair ( $W_{\text{ion}}$ ) are  $\sim 100 \text{ eV}$ <sup>2</sup> and  $22 \text{ eV}$ <sup>3</sup>, respectively. Therefore, with detector operating gas density at  $0.137 \text{ mol L}^{-1}$ , a muon event produce  $\sim 2 \times 10^2$  primary scintillation photons and  $\sim 10^3$  per centimeter length of muon trajectory. The large quantity of primary scintillation light and EL light production associated with free electrons results in large signal area detected for a muon event.

Therefore, a cosmic ray muon signal has a different appearance compared to other signals because of its long ionization trajectory and large quantity of primary scintillation light and electron-ion pair production. The appearance of muon signals also varies according to their different trajectories in the detector, which will be discussed below.

**EL region muon event** EL region muon events are those events that crosses the EL region, as well as the anode cone region and the cathode cone region. A cartoon and an example waveform are shown in Fig. 1.27. Like particle radiation events, at the very beginning of the signal, primary scintillation photons are produced in the first 500 ns. Simultaneously, during the first  $2.5 \mu\text{s}$ , the shown signal is dominated by EL photons, which decrease in time because the electrons in the EL region land on the anodic grid thus stopping EL photon production, illustrated in Fig. 1.27a (left). Since free electrons are generated all the way including the EL region, there is prompt EL light that masks the primary scintillation, causing difficulty to distinguish light from these two processes. At a higher absolute value of  $\Delta V_{\text{T-B}}$ , there is higher photon production per drifted electron, which results

---

<sup>2</sup> $W_{\text{sci}}$  is  $111(16) \text{ eV}$  in Ref. [22], and  $72(6) \text{ eV}$  in Ref. [23].

<sup>3</sup> $W_{\text{ion}}$  is  $22 \text{ eV}$  in Ref. [24–26].

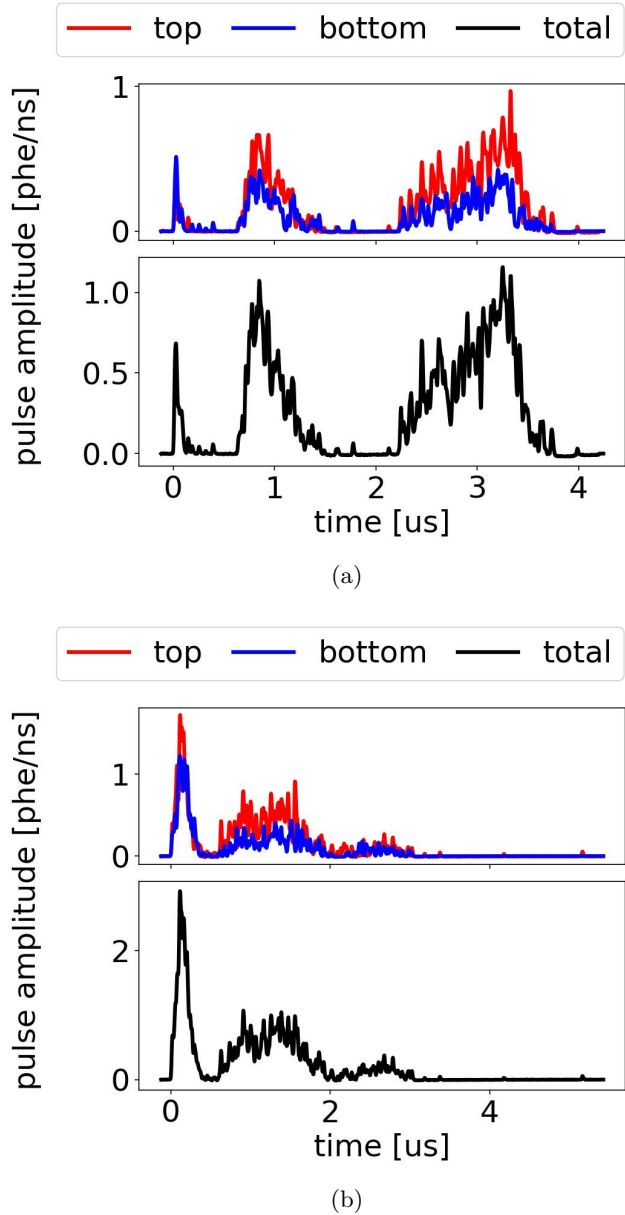


Figure 1.26: *Gas Test* signal: multiple scattering event. (a) An example waveform of a multiple scattering event in the anode cone region. (b) An example waveform of a multiple scattering event in the anode cone region and the EL region. Data were taken at 2017-12-8 14:02, with grid voltages  $V_T$  and  $V_B$  at +6 kV and -6 kV, operating gas density at  $0.137 \text{ mol L}^{-1}$ .

993 in an increase in the signal amplitude and signal area. This high signal amplitude can exceed the  
 994 dynamic digitization range of the DAQ and results in a clip on the waveform, like in Fig. 1.27b. After  
 995 all electrons in the EL region reach the anodic grid, the signal is dominated by electrons originally  
 996 produced in the anode cone drift to the anodic grid and EL photons are produced in the high electric  
 997 field around the anodic grid, illustrated in Fig. 1.27a (right), which is “long tail” part of the signal  
 998 in the range of  $2.5\ \mu\text{s}$  to  $10\ \mu\text{s}$  in Fig. 1.27b.

999 EL region muon events between grid rings are those events that crosses the EL region between  
 1000 the grid rings, without crossing the anode cone region. The cartoon of this process is shown in  
 1001 Fig. 1.28a. Similar to other EL region muon events, these events produces primary scintillation light  
 1002 and EL light between the grid rings. However, since the muon trajectory does not cross the anode  
 1003 cone region, there are no free electrons produced in such region, which leads to the absence of the  
 1004 “long tail” in the signal, as shown in Fig. 1.28b.

1005 **Anode cone muon event** Anode cone muon events are those events that crosses only the anode  
 1006 cone region. A cartoon and an example waveform are shown in Fig. 1.29. At the very beginning of  
 1007 the signal, primary scintillation photons are produce in the first 500 ns, the process and waveform  
 1008 of which are shown in Fig. ?? and Fig. 1.29c. Next, electrons originally produced in the anode cone  
 1009 drift to the anodic grid and EL photons are produced in the high electric field around the anodic  
 1010 grid, the process and waveform of which are shown in Fig. 1.29a and Fig. 1.29d.

1011 **Cathode cone muon event** Cathode cone muon events are those events that crosses only the  
 1012 cathode cone region. A cartoon and an example waveform are shown in Fig. 1.30. At the very  
 1013 beginning of the signal, primary scintillation photons are produce in the first 500 ns, the process and  
 1014 waveform of which are shown in Fig. 1.30a and Fig. 1.30b. Next, electrons originally produced in  
 1015 the cathode cone drift to the cathode PMT associated with few EL photons production in this low  
 1016 electric field cathode cone region.

#### 1017 1.8.4 Other miscellaneous sources

1018 **Electrical noise** Electrical noise are the disturbance in an electrical system during signal transfer.  
 1019 Electrical noise can come from both internal and external sources to the system, and can add to  
 1020 the systematic fluctuation of other signals from the *Gas Testdetector*. This systematic fluctuation  
 1021 is characterized by the baseline fluctuation, whose amplitude is  $\sim 0.36\ \text{mV}$ , which is very small  
 1022 compared to signal amplitude of the wanted signals.

1023 Electrical noise from the external electrical grounding of the infrastructures and the KNF pump,  
 1024 however, has an amplitude up to  $5\ \text{mV}$  and is capable of start a separate pulse recording sometimes;  
 1025 this type of electrical noise is called electrical noise signals. An example waveform of electrical noise  
 1026 signal is shown in Fig. 1.31. As shown in this figure, an electrical noise signal is likely to have the

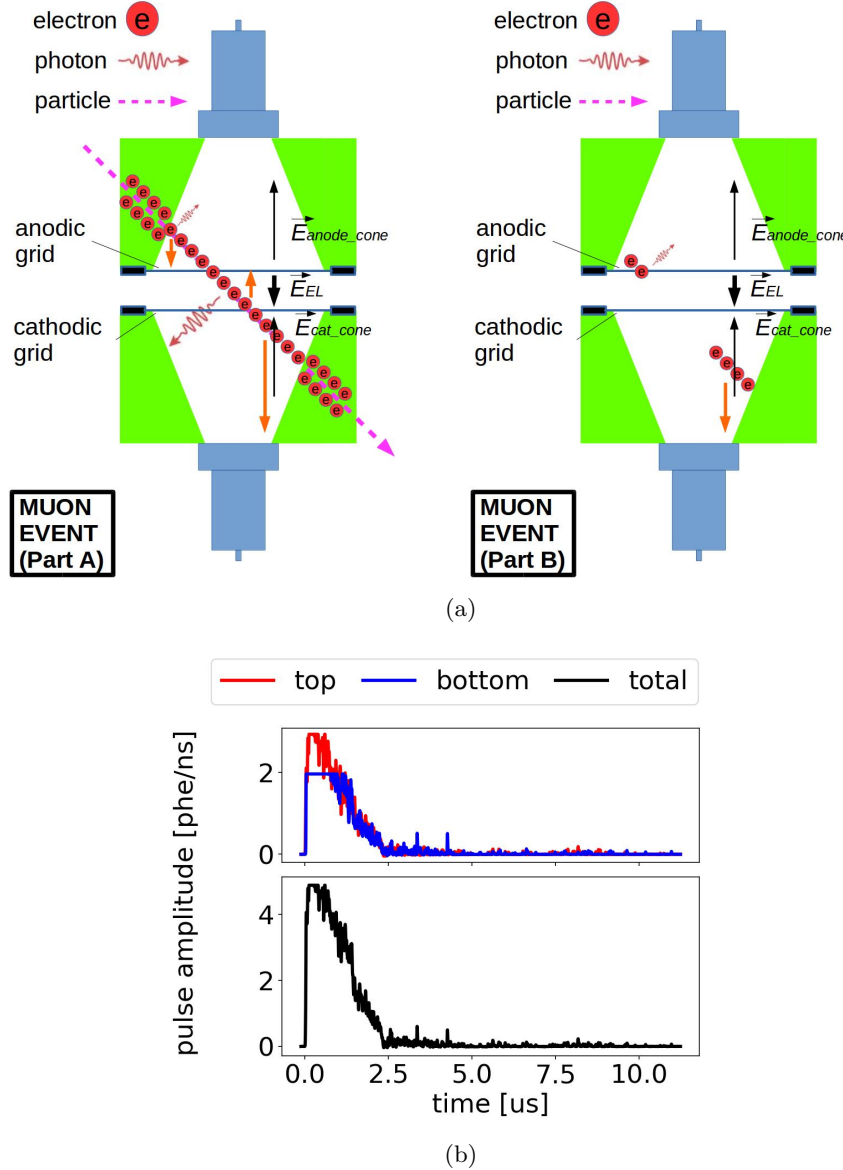


Figure 1.27: *Gas Test* signal: EL region muon event. (a) Cartoon of the process. Left: Primary scintillation light and ionization electrons are produced along the muon trajectory, and ionization electrons drift according to the direction of the electric field. EL light also start to be produced by the ionization electrons in the EL region (part A). Right: EL light is produced in the high electric field region around the anodic grid wires (part B). (b) An example waveform of an EL region muon event. The right-angled triangle shape waveform before  $2.5 \mu\text{s}$  is the EL light produced in the EL region (cartoon part A). The primary scintillation light is clipped off because of the PMT saturation. The “long tail” after  $2.5 \mu\text{s}$  is the EL light produced around the anodic grid wires (cartoon part B). Data were taken at 2017-12-8 14:02, with grid voltages  $V_T$  and  $V_B$  at  $+6 \text{ kV}$  and  $-6 \text{ kV}$ , operating gas density at  $0.137 \text{ mol L}^{-1}$ .

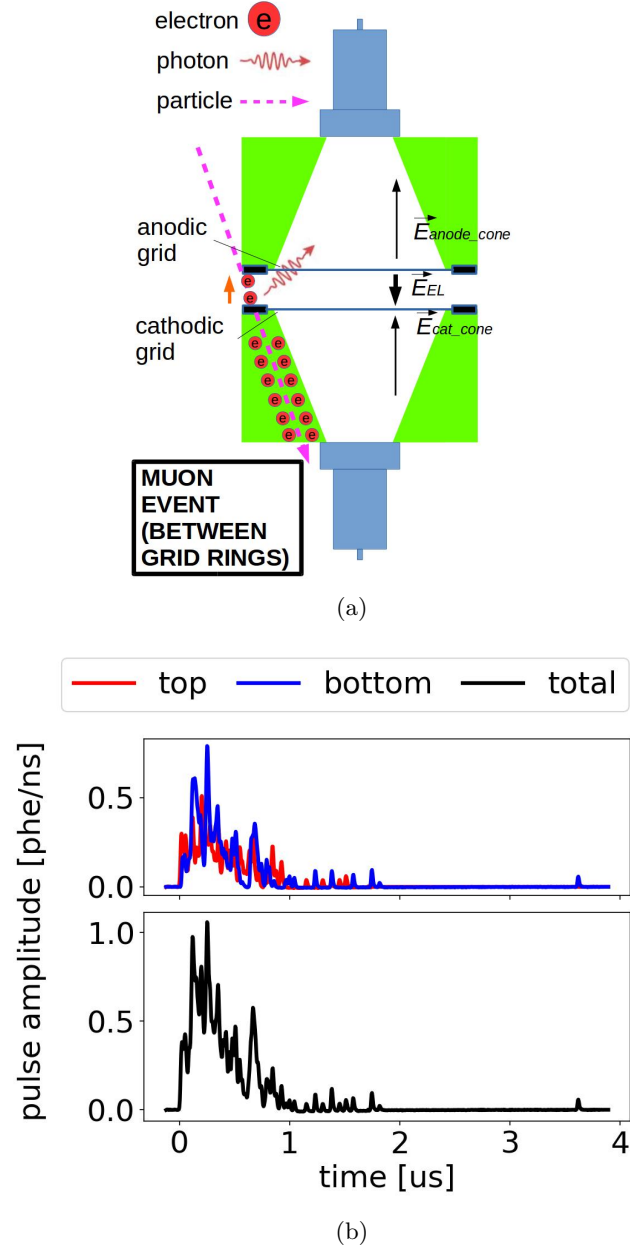


Figure 1.28: *Gas Test* signal: muon event between the grid rings. (a) Cartoon of the process. This process is similar to that of the EL region muon event except there are no electrons produced in the anode cone region. (b) An example waveform. The absence of “long tail” is because of the absence of electrons produced in the anode cone region. Data were taken at 2017-12-8 14:02, with grid voltages  $V_T$  and  $V_B$  at +6 kV and -6 kV, operating gas density at  $0.137 \text{ mol L}^{-1}$ .

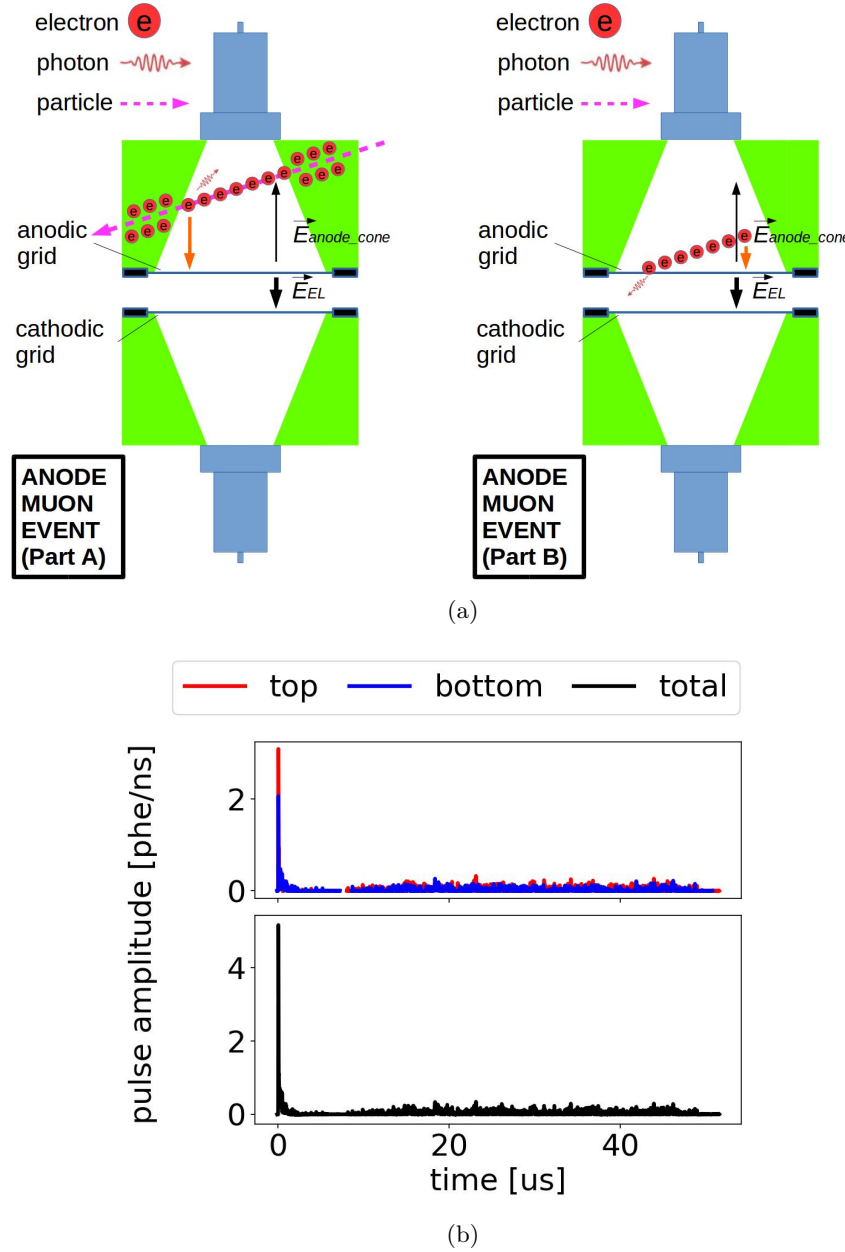


Figure 1.29: *Gas Test* signal: anode cone muon event. (a) Cartoon of the process. This process is similar to that of the EL region muon event except for there are no electrons produced in the EL region. (b) An example waveform of an anode muon cone event. The absence of the “right-angled triangle shape waveform” is because of the absence of electrons produced in the EL region. Data were taken at 2017-12-8 14:02, with grid voltages  $V_T$  and  $V_B$  at +6 kV and -6 kV, operating gas density at  $0.137 \text{ mol L}^{-1}$ .

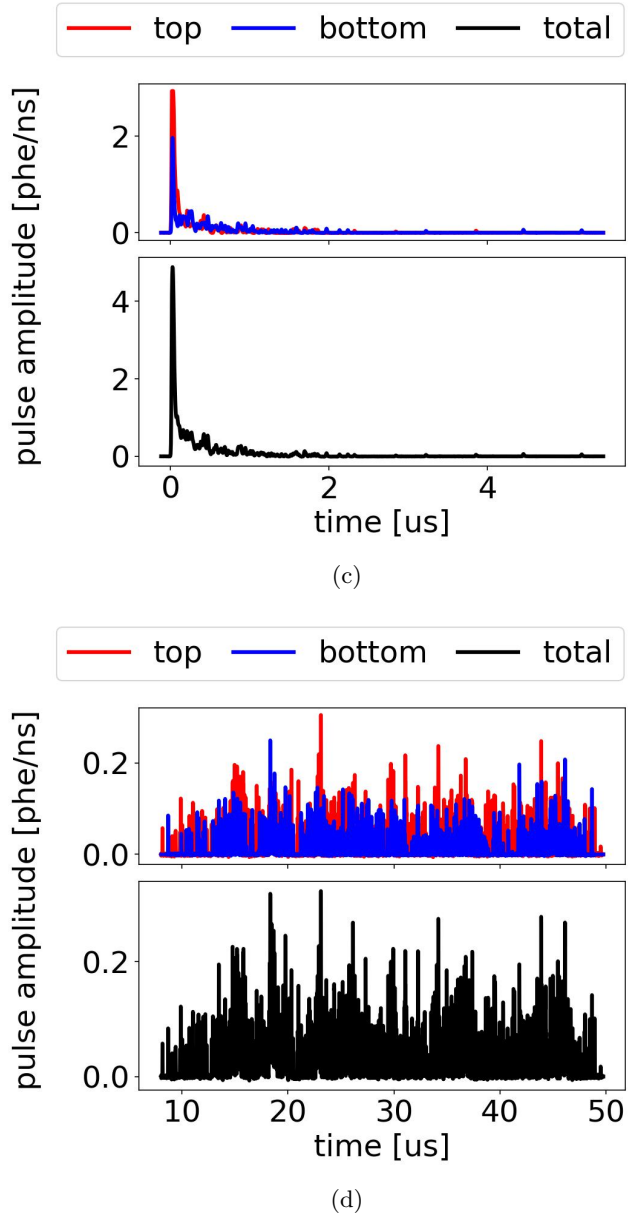


Figure 1.29: *Gas Test* signal: anode muon cone event (cont.). (c) An example waveform of an anode muon cone event, zoomed in the range of  $0 \mu\text{s}$  to  $5 \mu\text{s}$ , which shows the primary scintillation light (cartoon part A). (d) An example waveform of an anode cone muon event, zoomed in the range of  $6 \mu\text{s}$  to  $50 \mu\text{s}$ , which shows the EL light produced around the anodic grid wires (cartoon part B).

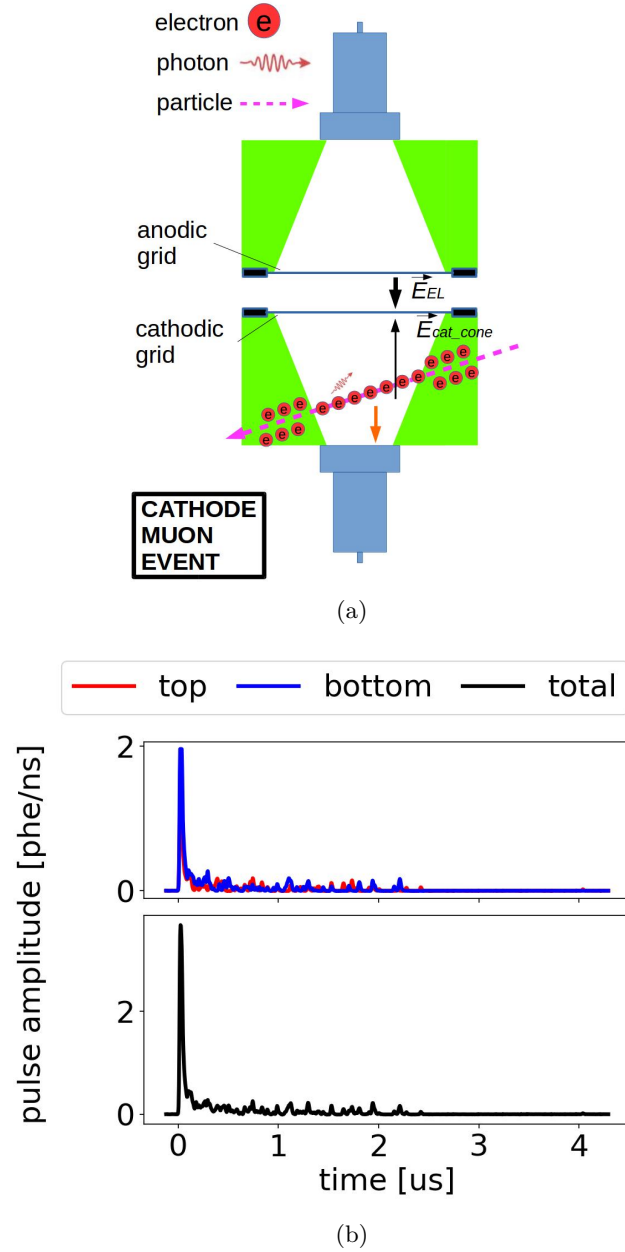


Figure 1.30: *Gas Test* signal: cathode cone muon event. (a) Cartoon of the process. This process is similar to that of the EL region muon event except for there are no electrons produced in the EL region or the anode cone region. (b) An example waveform of a cathode muon cone event. The absence of the “right-angled triangle shape waveform” and the “long tail” is because of the absence of electrons produced in the EL region and the anode cone region. Data were taken at 2017-12-8 14:02, with grid voltages  $V_T$  and  $V_B$  at +6 kV and -6 kV, operating gas density at  $0.137 \text{ mol L}^{-1}$ .

1027 waveforms in both PMTs overlapping. The waveform in each PMT is bipolar and symmetric; that  
 1028 is, the positive and negative maxima of the waveform amplitude are about the same. The bipolar  
 1029 and symmetric aspect of the waveform leads to a near-zero integral of the signal area, which don't  
 1030 give a meaningful waveform shape RQs because these RQ algorithms are designed for a unipolar  
 1031 signal. Therefore, to reduce the influence of these electrical noise signals, the KNF pump is turn off  
 1032 during all measurements and we improved on the electrical grounding of infrastructure. After this  
 1033 improvement, electrical noise signals occur at a rate of  $\sim 2$  Hz, which are further addressed by signal  
 1034 selections based on the bipolar feature of the noise signals.

1035 **PMT dark current** PMT dark current usually refers to the signal from the thermal electron  
 1036 emission from the photocathode and dynode surfaces, which are charges generated in the PMT  
 1037 when no photon ejects photoelectrons from the photocathode surface. The thermal electrons from  
 1038 the photocathode surface, like photoelectrons, if landing on the effective area of the first dynode, will  
 1039 be amplified by the PMT and produce a SPHE-like signal. Such SPHE-like signals of the PMT dark  
 1040 current are a major concern, since they are not distinguishable from SPHEs in signals of interest.  
 1041 The thermal electrons from other surfaces may also be amplified by the PMT dynode chain and  
 1042 produce signals that are distinguishably smaller than SPHE, thus drawing less concern.

1043 A random coincidence of SPHE-like signals (dark current is one of the most common sources of  
 1044 SPHE-like signals) between two PMTs, is called an accidental coincidence signal. The PMTs that  
 1045 are used in this study have a  $\sim 1$  kHz dark current rate. This rate leads to a  $\sim 3.4$  Hz rate of the  
 1046 accidental coincidence signals with regard to CWW of  $1.7\ \mu s$ .

1047 **should I talk about PMT afterpulsing?**

1048 **PTFE fluorescence** PTFE fluorescence is the phenomenon in which PTFE emits photons that  
 1049 it absorbed. This delay emission normally appears in forms of SPHEs following a high quantity  
 1050 of photon production, and increase the SPHE rate succeeding. The rate of after emission photons  
 1051 (fluorescence rate) roughly follows an exponential decay model:

$$\text{fluorescence rate} = f_{\text{FR}} A \frac{1}{\tau} \exp\left(-\frac{t}{\tau}\right) \quad (1.21)$$

1052 where  $\tau$  is the decay time constant;  $t$  is the time since the previous photon production;  $A$  is quantity of  
 1053 photons in the previous photon production that are absorb by the PTFE; and  $f_{\text{FR}}$  is the fluorescence  
 1054 ratio, which is the ratio of the number of photons emitted after by the PTFE material to the number  
 1055 of photons absorbed by the PTFE material.

1056 Measurements show that fluorescence rates, decay times  $\tau$ , and fluorescence ratio  $f_{\text{FR}}$  have a vari-  
 1057 ous range. This might be caused by different conditions of synthesis, as described in Ref. [Gachkovskii1969].  
 1058 This effect is also believed to cause the slow decay of electron signal in liquid xenon TPCs. A decay  
 1059 time of 2.3 ms is reported in Ref.[27]. A decay time of 10 ms is reported in internal review in LUX.

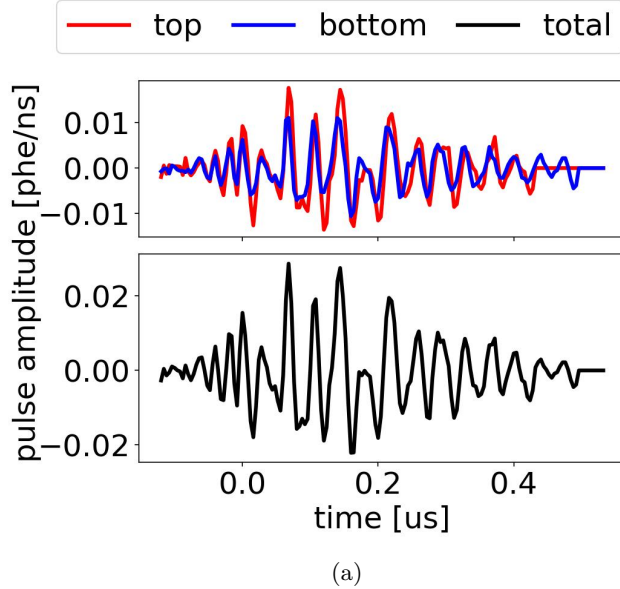


Figure 1.31: *Gas Test* signal: electronic noise signal. (a) An example waveform. Data were taken at 2017-12-8 14:02, with grid voltages  $V_T$  and  $V_B$  at +6 kV and -6 kV, operating gas density at  $0.137 \text{ mol L}^{-1}$ .

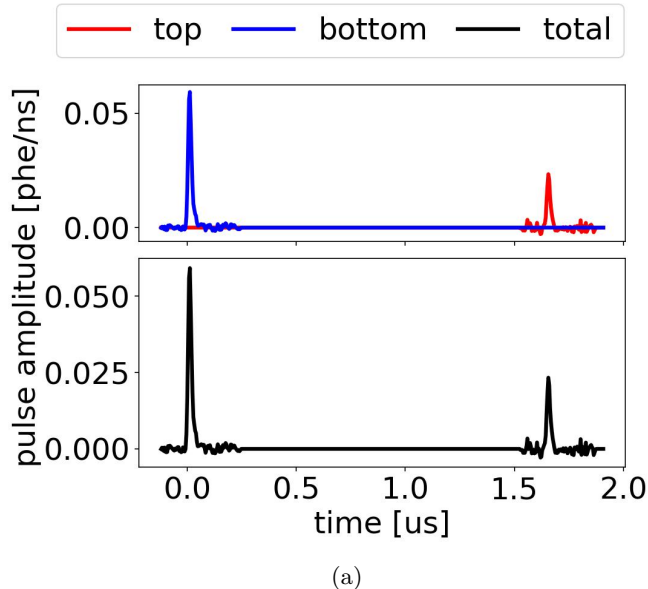


Figure 1.32: *Gas Test* signal: PMT dark current accidental coincidence. (a) An example waveform. Data were taken at 2017-12-8 14:02, with grid voltages  $V_T$  and  $V_B$  at +6 kV and -6 kV, operating gas density at  $0.137 \text{ mol L}^{-1}$ .

1060 To illustrate the large rate of SPHEs that follows a large-area signal, we look at 1-ms windows  
 1061 before and after a large photon production. In the succeeding 1-ms window after  $t = 0$ , which is the  
 1062 time when the selected large signal happened, as shown with the selected large signal in Fig. 1.33a,  
 1063 Fig. 1.33b, we see 33 SPHEs. In comparison, we see only 1 SPHE in the earlier 1-ms window, as  
 1064 shown in the same figure before  $t = 0$ . This increasing rate of SPHE increases the probability of  
 1065 accidental coincidence between two PMT channels, as shown in Fig. 1.33c; given the practical choice  
 1066 of our CCW, this random accidental coincidence, like PMT dark current, is a potential source of  
 1067 background that looks like electron emission signals.

1068 With these examples in mind, we can quantify the fluorescence process by looking at the delayed  
 1069 SPHE rate follow large-area signals over different characteristic timescales. The SPHE rate of this  
 1070 PTFE fluorescence increase if the ELD has a recent large photon production. Fig. 1.34 shows the  
 1071 photon rate after source signals: This photon fluorescence rate increases as the signal area of source  
 1072 signals increases; and this photon fluorescence rate decreases over time.

1073 An estimation of fluorescence rate, decay time  $\tau$ , and fluorescence ratio  $f_{\text{FR}}$  is carried out by  
 1074 studying the photon rate in the waveform after a signal production of larger than  $10^4$  phe in the range  
 1075 of  $200 \mu\text{s}$  to  $600 \mu\text{s}$  after the end time of signal. The choice of the smaller value of the succeeding  
 1076 window is to avoid the influence from the anode cone events correlating signals, whereas the choice  
 1077 of the later time of the succeeding window is to avoid the influence the background rate, which is  
 1078 mostly contributed by dark current. In the chosen signal ranges, the background rate is  $\sim 1 \text{ kHz}$  per  
 1079 PMT, mostly contributed by PMT dark current. This rate is small compared to fluorescence rate  
 1080 (median  $\sim 20 \text{ kHz}$ ) per PMT, thus negligible in this estimation. Therefore,

$$\text{photon rate} \approx \text{fluorescence rate} (+ \text{background rate (dark current, etc.)}) \quad (1.22)$$

$$\propto \frac{1}{\tau} \exp\left(-\frac{t}{\tau}\right) \quad (1.23)$$

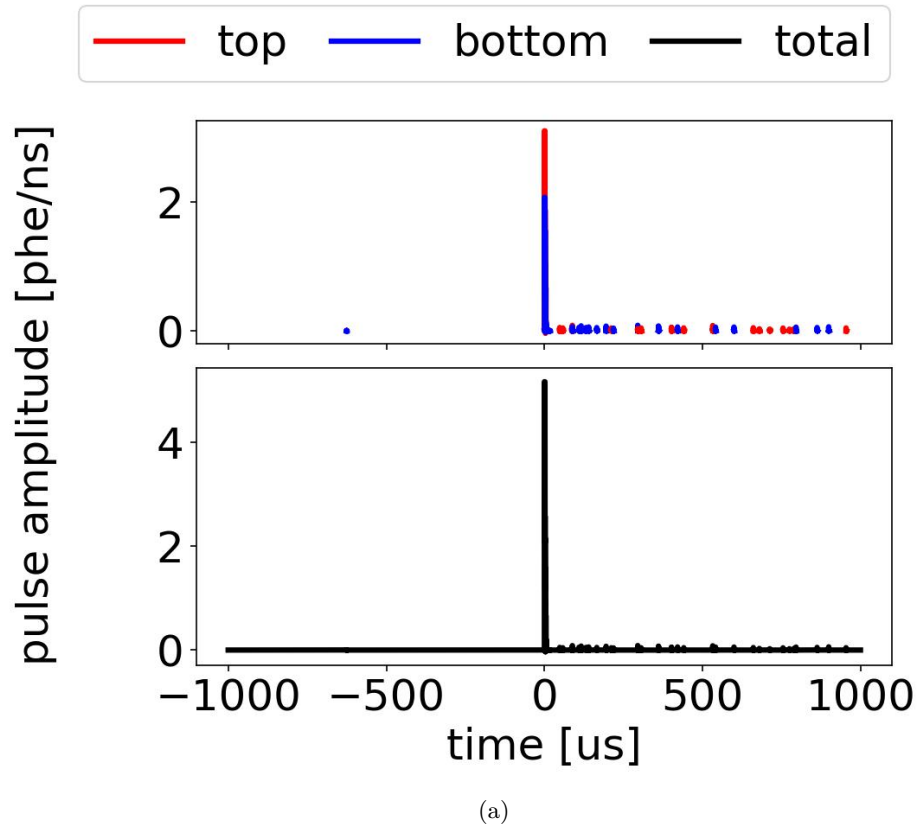
1081 To better estimate the photon rate profile and find the decay time  $\tau$ , we fit this exponential decay  
 1082 profile to binned data in the succeeding window. To combine multiple events to reduce the statistical  
 1083 error, individual events are normalized by their signal areas in the range of  $0 \mu\text{s}$  to  $1000 \mu\text{s}$  and then  
 1084 co-added by bin; the resulting graph is fitted, and shown in Fig. 1.35:  $\tau$  of  $(407 \pm 35) \mu\text{s}$ .

1085 The fluorescence ratio  $f_{\text{FR}}$  is defined as,

$$f_{\text{FR}} = \frac{\# \text{ photons reemitted}}{\# \text{ photons absorbed}} \quad (1.24)$$

1086 which is the ratio of the number of photons that are reemitted from the PTFE after a large-area  
 1087 event to the number of photons that are absorbed by the PTFE in a large-area event.

1088 The number of photons reemitted is estimated from the exponential decay profile defined above



(a)

Figure 1.33: *Gas Test* signal: PTFE fluorescence after an event with large photon production. (a) An example waveform 1000  $\mu\text{s}$  before and after a large-area signal. There are more SPHEs after an event with large photon production than before. The SPHE rate before this large-area event is representative of the average SPHE rate. Data were taken at 2017-12-8 14:02, with grid voltages  $V_T$  and  $V_B$  at +6 kV and -6 kV, operating gas density at 0.137 mol L $^{-1}$ .

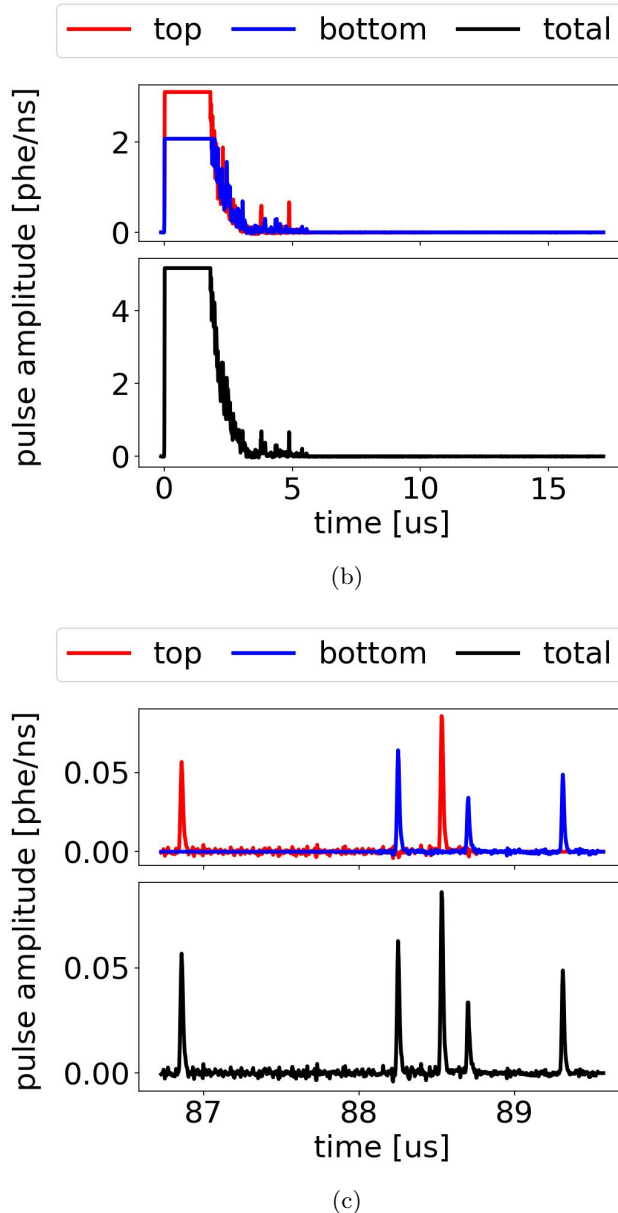


Figure 1.33: *Gas Test* signal: PTFE fluorescence after an event with large photon production (cont.). (b) An example waveform, zoomed in the range of  $0\ \mu\text{s}$  to  $17\ \mu\text{s}$ , which shows the signal with large photon production. (c) An example waveform, zoomed in the range of  $87\ \mu\text{s}$  to  $89\ \mu\text{s}$ , which shows PTFE fluorescence induced SPHEs accidental coincidence between the two PMTs. This accidental coincidence signal looks like an electron emission signal.

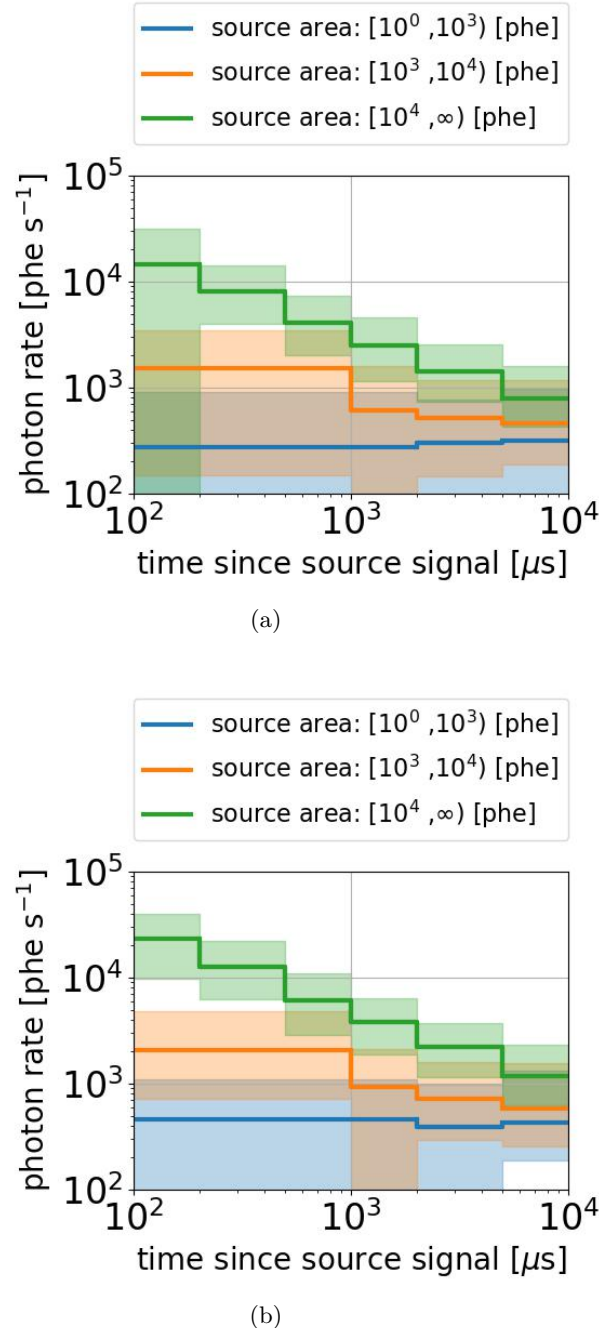


Figure 1.34: Photon fluorescence rate after photon production in the ELD: (a) top PMT; (b) bottom PMT. The solid lines show the medians. The color bands show the 25 % to 75 % bands. The choice of bin edges is made to get enough statistics in each bin.

1089 and the number of photons in the succeeding 200 ns to 600 ns window after the end of the large-  
 1090 area signal. From the estimated decay time, the ratio of the number of reemitted photons in the  
 1091 succeeding window ( $N_{\text{SW}}$ ) to the total number of reemitted photons is derived, noted as  $P_{\text{SW}}$ :

$$P_{\text{SW}} \approx \frac{N_{\text{SW}}}{\# \text{ photons reemitted}}. \quad (1.25)$$

1092 The number of reemitted photons in the succeeding window is estimated from the number of  
 1093 photons reemitted detected in the succeeding window ( $A_{\text{SW}}$ ) and the light collection efficiency for  
 1094 photons starting from PTFE surface:

$$A_{\text{SW}} \approx \text{LCE}_{\text{PTFE}} N_{\text{SW}}. \quad (1.26)$$

1095 where  $\text{LCE}_{\text{PTFE}}$  is the average light collection efficiency for photons starting from PTFE surface.

1096 On the other hand, the number of photons absorbed by PTFE is estimated from the total number  
 1097 of photons the source large-area signal ( $N_{\text{source}}$ ) and the light collection simulation of the fraction  
 1098 of photons that PTFE absorbed:

$$\# \text{ photons absorbed} \approx \text{LCF}_{\text{EL-PTFE}} N_{\text{source}} \quad (1.27)$$

1099 where  $\text{LCF}_{\text{EL-PTFE}}$  is the average fraction of photons absorbed by PTFE in the simulation with  
 1100 photons starting in the EL region, the location where the source signals happen.

1101 The total number of photons the source large-area signal ( $N_{\text{source}}$ ) is related to the detected  
 1102 signal area ( $A_{\text{source}}$ ) and light collection efficiency of the source signals in the EL region ( $\text{LCE}_{\text{EL}}$ ).

$$A_{\text{source}} \approx \text{LCE}_{\text{EL}} N_{\text{source}} \quad (1.28)$$

1103 Therefore, from the measure ratio of signal area in the succeeding window ( $A_{\text{SW}}$ ) to the source  
 1104 signal area ( $A_{\text{source}}$ ), the result of which is shown in Fig. 1.36, we can derive the fluorescence ratio  
 1105  $f_{\text{FR}}$ .  $P_{\text{SW}}$  is  $\sim 0.23$  with regard to the decay time  $\tau$ .  $\text{LCE}_{\text{PTFE}}$  is 2.85 % (top PMT: 1.35 %, bottom  
 1106 PMT: 1.50 %);  $\text{LCE}_{\text{EL}}$  is 1.70 % (top PMT: 0.85 %, bottom PMT: 0.85 %); and  $\text{LCF}_{\text{EL-PTFE}}$  is 79.3 %  
 1107 (top cone: 39.0 %, bottom cone: 40.3 %), which are estimated by using the same method as described  
 1108 in Section 1.6 using PTFE reflectivity of 0.4. With the ratio of  $A_{\text{SW}}$  to  $A_{\text{source}}$   $\sim 0.5 \times 10^{-3}$ ,  $f_{\text{FR}}$   
 1109 is  $\sim 1.6 \times 10^{-3}$ . This result has a big uncertainty (up to  $1 \times 10^{-3}$ ) due to statistic errors, and the  
 1110 systematic errors in the light collection efficiency and the absorption fraction, resulting from the  
 1111 uncertainty in the PTFE reflectivity value.

1112 **Cherenkov radiation** think about gamma particle induced cherenkov, and whether the calcula-  
 1113 tion is correct. Cherenkov radiation is the photon radiation process when a charged particle is

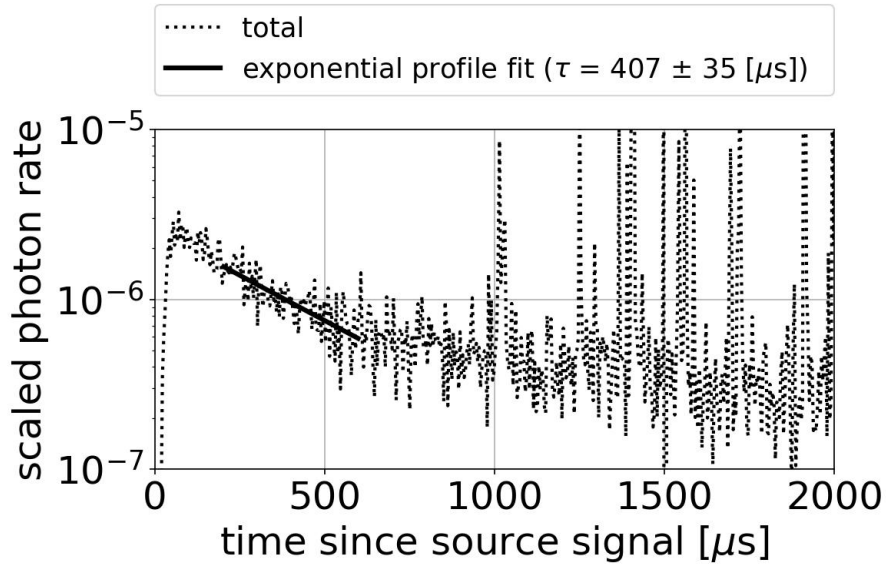


Figure 1.35: The average of scaled waveform in the range of  $0 \mu\text{s}$  to  $2000 \mu\text{s}$  since source signals. See text for details.

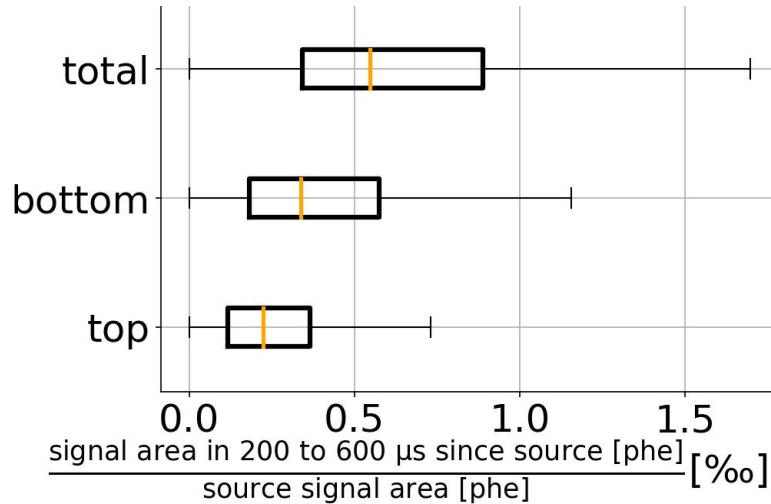


Figure 1.36: The ratio of the number of SPHEs in the range of  $200 \mu\text{s}$  to  $600 \mu\text{s}$  since source signals to the number of SPHEs in the source signal.

traveling through a medium with its speed higher than the speed of light in the medium. The charged particle could be an external charged particle or electrons that originate from energy loss of external particle in the medium. Because of the photon production in Cherenkov radiation process, especially when this process happens in the PTFE materials (and the PMT windows), it is considered to one of the sources of the signals in *Gas Test*. A cartoon for the physical process and an example waveform of extremely narrow pulse are shown in Fig. 1.37.

The quantity of photon production in Cherenkov radiation process is estimated by its theoretical spectrum following Frank–Tamm formula. A simplified approximation for Frank–Tamm formula from Ref. [Jackson1999] Eqn. 14.133 shows:

$$\frac{dI(\omega)}{dx} = \frac{e^2\omega}{c^2} \left[ 1 - \frac{1}{\beta^2\epsilon(\omega)} \right] \quad (1.29)$$

where  $\omega$  is the frequency of Cherenkov radiation,  $I(\omega)$  is the energy intensity of frequency  $\omega$ ,  $\epsilon(\omega)$  is the relative permittivity of the medium, and  $\beta$  is the speed of the charged particle.  $\omega$  satisfies that  $\beta^2\epsilon(\omega)$  is larger than one, so that the energy intensity is positive. The number intensity  $N(\omega)$  can be derived from Eqn. 1.29

$$\frac{dN(\omega)}{dx} = \frac{\alpha}{c} \left[ 1 - \frac{1}{\beta^2\epsilon(\omega)} \right] \quad (1.30)$$

where  $\alpha \equiv e^2/\hbar c \approx 1/137$  is the fine structure constant. The total quantities of photons ( $N$ ) is the integral over frequency and distance of Eqn. 1.30.

A portion of these Cherenkov radiation photons can be seen by the PMTs, since PTFE is partially transparent to these photons. The duration of Cherenkov radiation event light production is the duration of charged particle energy loss process, which is typically very short ( $\sim 1$  ns to  $10$  ns). The number of photons ( $A_{\text{Che}}$ ) detected by the PMTs for a typical 1 MeV electron is estimated using the following parameters:

$$A_{\text{Che}} \approx N_{\text{Che}} f_{\text{to-surface}} \exp(-d_{\text{to-surface}}/d_{\text{atten}}) \text{LCE}_{\text{PTFE}} \quad (1.31)$$

where  $N_{\text{Che}}$  is the number of produced Cherenkov radiation photons which the PMTs are sensitive to;  $f_{\text{to-surface}}$  is the fraction of Cherenkov radiation photons going toward the PTFE surface;  $d_{\text{to-surface}}$  is the distance from the location of Cherenkov radiation produce to the PTFE surface;  $d_{\text{atten}}$  is the attenuation length of PMT sensitive Cherenkov radiation photons; and  $\text{LCE}_{\text{PTFE}}$  is the light collection efficiency for photons exiting PTFE surfaces.

$N_{\text{Che}}$  is related to PMT sensitivity, we take the PMT sensitive photon wavelength in the range of 160 nm to 650 nm (the spectral response range for PMT R11410-10, as described in Ref. [1]).  $N_{\text{Che}}$  is also related the PTFE refractive index, and electron stopping distance, which are approximately 2 ( $\epsilon \sim 4$ ), and  $\sim 10^{-1}$  cm for a 1 MeV electron in PTFE, respectively. The attenuation distance of

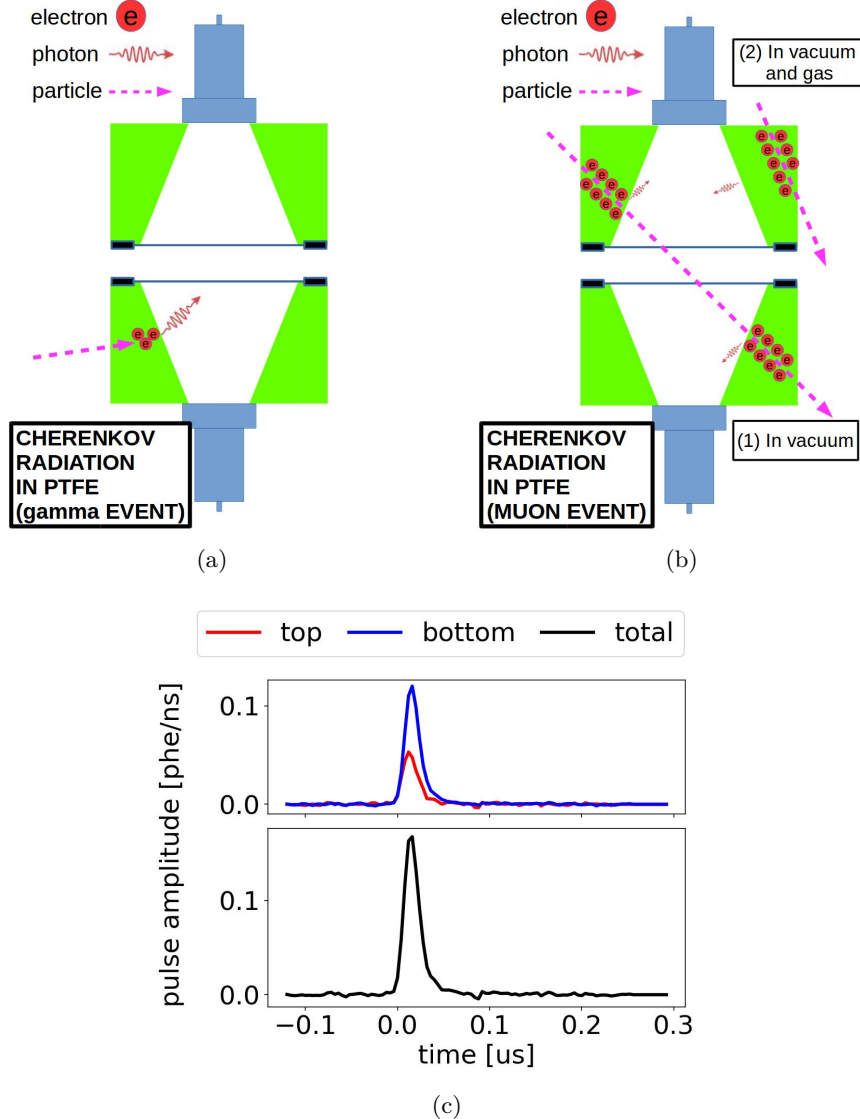


Figure 1.37: *Gas Test* signal: Cherenkov radiation in PTFE. (a) Cartoon of the process in which Cherenkov radiation is produced in PTFE. The Cherenkov radiation comes from the electrons created in a gamma particle event. (b) Cartoon of the process in which Cherenkov radiation is produced in PTFE after a muon particle crossing the detector. (1) If the detector is in vacuum, even though the muon particle crosses the cone regions, there is no primary scintillation or ionization inside the ELD active volume, and only Cherenkov radiation signals from this muon event in PTFE are observed. (2) A muon particle does not cross the cone regions. Cherenkov radiation signals from this muon in PTFE are observed. (c) An example waveform of a Cherenkov radiation event. Data were taken at 2017-12-8 14:02, with grid voltages  $V_T$  and  $V_B$  at +6 kV and -6 kV, operating gas density at  $0.137 \text{ mol L}^{-1}$ .

photons  $d_{\text{atten}}$  is  $\sim 7$  cm for a 1 MeV electron for PTFE, from Ref. [28]. The light collection efficiency LCE<sub>PTFE</sub> is in the range of 1.5 % to 15 %, as described in Section 1.6. Therefore, taking  $d_{\text{to-surface}}$  to be 0 cm to 1 cm, and taking  $f_{\text{to-surface}}$  to be 10 % to 50 %,  $N_{\text{Che}}$  is  $\sim 150$ , and the estimated number of Cherenkov photons detected by the PMTs is in the range of up to  $\sim 10$  phe. Even though this estimated number of photons is not very big, however it is large enough to be seen by both PMTs. For a muon, we can do a similar estimation with changing the stopping distance to the full length of muon trajectory in PTFE, which is  $\sim 5$  cm. Therefore, the estimated number of Cherenkov photons detected by the PMTs in a muon event is in the range of up to  $\sim 500$  phe. The exact number of detected Cherenkov photons is hard to predict precisely because of the complicated geometry of ELD. However, these estimations conclude that Cherenkov events are one of the visible background signals in our detector.

One of the most convincing evidence is the existence of Cherenkov radiation events is that short-duration signals are seen in the detector at vacuum condition. Fig. 1.38a shows the signal  $t_{01-99}$  duration vs. signal area plot from a dataset with grid voltages  $V_T$  and  $V_B$  at 0kV, operating gas density at vacuum. The black box shows the potential events which are considered to be associated with Cherenkov radiation process. Since the detector is at vacuum condition, it is lack of other photon production processes. These potential Cherenkov radiation events may source from both external charged particles and energy loss of external particles, likely an external higher energy photon (gamma radiation), or a cosmic ray muon. This process is described below: An external particle travels through the PTFE cones, lose its energy, ionizes molecules in PTFE and radiates photon along its trajectory. Since muon particles are usually more energetic than other external particles like gamma radiation, the Cherenkov radiation from muon events is usually larger. This is one explanation for the “hot spot” at  $(10^2, 10^2)$  in Fig. 1.38a. When the detector is filled with xenon gas, the muon particle can also ionize xenon gas atoms inside ELD active volume. This process produces scintillation photons and ionization electrons, and the EL process associated with ionization electrons usually increases signal duration. It explains the reason that this “hot spot” shifts between vacuum data and xenon gas data. Details for explanations of muon events in xenon gas data are in Section ???. The signals with their area in the range of 0 phe to  $10^2$  phe and signal duration in the range of 0 ns to  $2 \times 10^2$  ns in Fig. 1.38a are likely to be Cherenkov radiation events from muons that do not cross the ELD active region and external gamma radiation induced fast electrons in PTFE (and PMT window). The gamma radiation can scatter electrons in PTFE. These fast-moving scattered electrons can also produce Cherenkov radiation light. When the detector is filled with xenon gas, the same physical processes of Cherenkov radiation from muon and gamma radiation remain. Therefore, these processes explain why a similar population of Cherenkov radiation events exist in both vacuum data (Fig. 1.38a) and xenon gas data (Fig. 1.38b).

**Discharge** Discharges happen inside and outside the ELD could produce signals that can be seen by the PMTs. In sparking tests, we observe discharges on the high voltage feed throughs and cables,

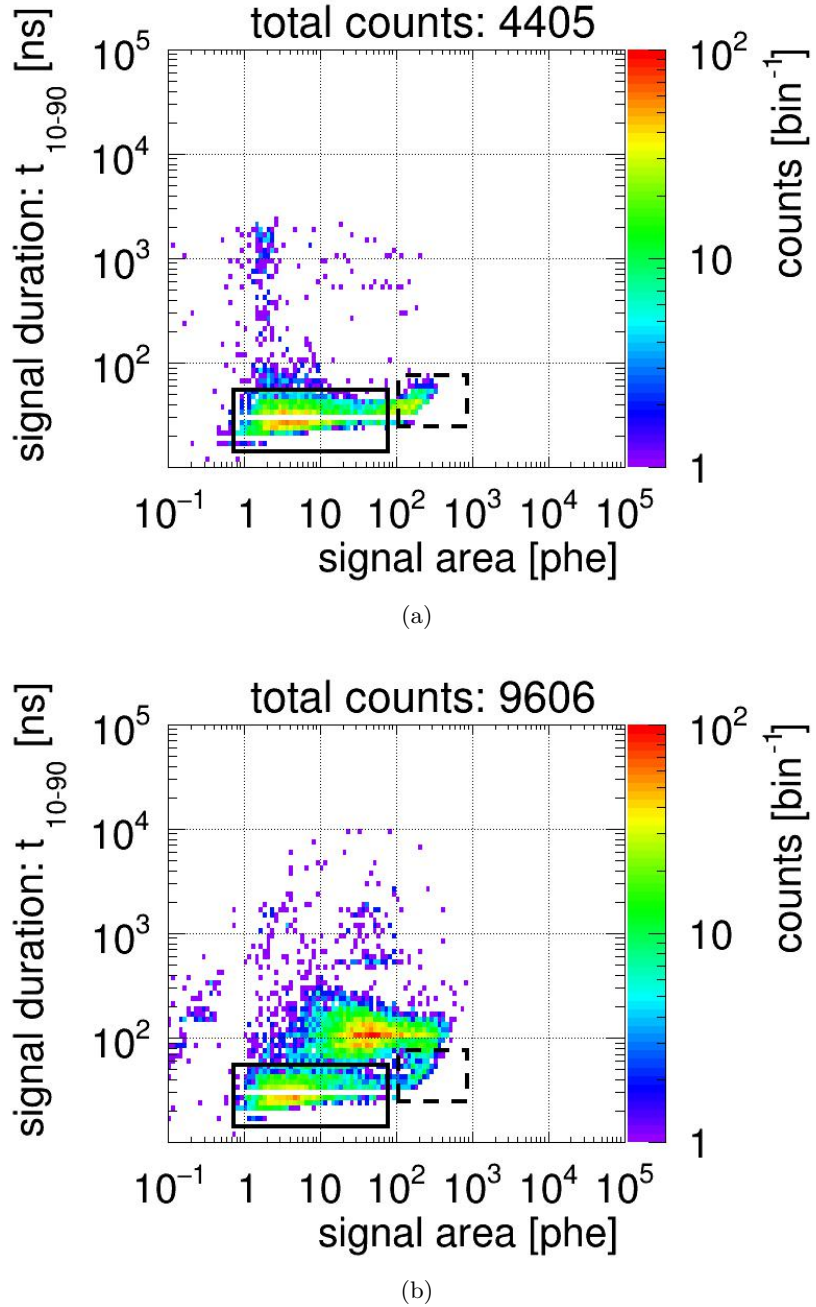


Figure 1.38: *Gas Test* signal  $t_{10-90}$  duration vs. signal area. (a) Vacuum data. Data were taken at 2018-03-12 11:41, with grid voltages  $V_T$  and  $V_B$  at 0 kV, operating gas density at vacuum. (b) Xenon gas data. Data were taken at 2017-12-8 13:12, with grid voltages  $V_T$  and  $V_B$  at 0 kV, operating gas density at  $0.137 \text{ mol L}^{-1}$ . The black solid line indicates the muon events which crosses the cone regions. The black dashed line indicates the muon events which do not cross the cone regions, and might also include gamma radiation events in PTFE.

1180 which are caused by the smoothness of the high voltage surfaces (especially metallic surfaces) are  
1181 imperfect. This imperfection creates a high field region, and initialized a high  
1182 ionization probability of the medium (especially gas medium) surrounding it and causes a discharge.  
1183 The quantity of light production of these discharges has a various range and usually are big. However,  
1184 depending on the location of the discharge, signals of the discharge have different appearances. The  
1185 discharges happening outside the ELD may end up having one or several SPHEs in each PMTs with  
1186 regard to the poor light collection at such location. However, the discharges happening inside the  
1187 ELD may look like electron emission signals.

## 1188 1.9 Signal selections

1189 This section discusses signal selections, also known as cuts, that are used in the *Gas Test* analysis.  
1190 The purpose of this analysis is searching for electron emission signals from tested grid wires, and  
1191 correctly estimating the rate of this process. For this purpose, signal selections on different parameter  
1192 spaces are carried out to identify background signals from electron emission signals. **For each signal**  
1193 **selection, the possibility of removing electron emission signalis evaluated.** The primary principle of  
1194 signal selections is to get a clean population distribution of electron emission signal to get a reliable  
1195 estimation of its rate. Other than that, since electron emission signals are in most situation rare in  
1196 the detector, signal selections of these electron emission signals are done conservatively; that is to  
1197 keep as many candidates for electron emission signals as possible.

1198 An electron emission signal should:

- 1199 • have the correct signal shape.  
1200 • be an uncorrelated signal from previous signals in time, and

1201 Based on the characteristics we summarize previously about electron emission signal and other  
1202 different signals in the detector, a list of selections to get electron emission signals are carried out  
1203 and discussed.

### 1204 1.9.1 Signal selections based on signal shape

1205 Signal shape is one of the most important signature for electron emission signals . It includes the  
1206 aspects of the signal area, the signal duration, and the SPHE rate at different time region during  
1207 the event.

#### 1208 Coincidence found

1209 **Definition** Both PMTs have signals that occur within a time difference smaller than CWW.

1210 **Purpose** This is to make sure that the signal of interest is unlikely to be from a dark current  
1211 signal in one PMT, or SPHE from other sources in one PMT (e.g. fluorescence light from PTFE,  
1212 discharges).

1213 The process of coincidence found and coincidence event building is discussed in the data processing  
1214 section in Section 1.4. An example of coincidence event building result is shown in Fig. 1.39a.  
1215 The signal area has a various distribution mostly in the range of  $10^{-1}$  phe to  $10^5$  phe, when the  
1216 signal  $t_{10-90}$  duration, and the TBA, top-bottom asymmetry, are mostly distributed in the range of  
1217  $10^1$  ns to  $10^5$  ns and  $-1$  to  $1$ . Several “hot spots” that are seen in the figure correspond to different  
1218 activities in the detector, which will be explained later in each separate section of signal selection.  
1219 Among these “hot spots”, the horizontal strap shape spot at signal area in the range of  $10^1$  phe to  
1220  $10^2$  phe, signal  $t_{10-90}$  duration in the range of  $10^3$  ns to  $10^4$  ns, is likely to contain the potential elec-  
1221 tron emission signals. The locations and the counts of different “hot spots”, including the “hot spot”  
1222 of electron emission signals, change as varying  $\Delta V_{T-B}$  and operating gas density, mainly because of  
1223 the changes of the duration and the intensity of the EL process.

1224 Coincidence found and coincidence event building are the fundamental part of this analysis.  
1225 Signal selections defined later are based on the classification of coincidence-found signals.

#### 1226 Not a noise-like signal

1227 **Definition** A coincidence-found signal has a positive signal area in all PMT channels, a higher  
1228 than 0.5 positive to negative amplitude ratio, and a positive signal  $t_{10-90}$  duration.

1229 **Purpose** This is to make sure the signal of interest is not an electrical noise signal, which usually  
1230 has a close to zero signal area, a close to unity positive to negative amplitude ratio, or a zero signal  
1231  $t_{10-90}$  duration, as described in Section 1.8.4. The effect of this selection is shown in Fig. 1.39b.  
1232 Noise-like signals, mostly at signal area in the range of  $<1$  phe, signal  $t_{10-90}$  duration in the range  
1233 of  $<10^3$  ns, are rejected.

#### 1234 Not a narrow (S1-like) signal

1235 **Definition** A coincidence-found signal has a signal  $t_{25-75}$  width (time difference between the time  
1236 of 25th percentile of the signal waveform and the time of 75th percentile of the signal waveform)  
1237 larger than 250 ns, and a signal  $t_{50}$  width (time difference between the signal start time and the time  
1238 of 50th percentile of the signal waveform) larger than 320 ns; in other words, the major width of the  
1239 coincidence-found signal is not narrow.

1240 **Purpose** This is to make sure the signal of interest is not a potential (1) Cherenkov radiation event,  
1241 or (2) primary scintillation light (S1) from an external particle (e.g. gamma radiation, muon), as  
1242 described in Section 1.8.4, Section 1.8.2, and Section 1.8.3. The effect of this selection is shown in

1243 Fig. 1.39c. The narrow signals can generally be separated to two categories, corresponding to the  
 1244 two “hot spots” in the figure. The first “hot spot” at signal area in the range of 1 phe to  $10^2$  phe,  
 1245 signal  $t_{10-90}$  duration in the range of  $<5 \times 10^1$  ns, may results from Cherenkov radiation events and  
 1246 primary scintillation light of low energy gamma radiation events. The second “hot spot” at signal  
 1247 area  $10^1$  phe to  $10^3$  phe, signal  $t_{10-90}$  duration in the range of  $5 \times 10^1$  ns to  $2 \times 10^2$  ns are likely from  
 1248 primary scintillation light of gamma radiation events and muon events.

1249 **Not a two-SPHE accidental coincidence signal**

1250 **Definition** A coincidence-found signal has a signal area larger than 2.5 phe, and at least one PMT  
 1251 has a signal  $t_{25-75}$  width larger than 35 ns, which is approximately twice the signal width of a SPHE.

1252 **Purpose** This is to make sure the signal of interest is not a accidental coincidence of two SPHEs,  
 1253 which are likely from PMT dark current and other SPHE sources (e.g. PTFE fluorescence, dis-  
 1254 charges), as described in Section 1.8.4, Section 1.8.4, and Section 1.8.4. The effect of this selection  
 1255 is shown in Fig. 1.39d. Two-SPHE accidental coincidence signals, mostly at signal area in the range  
 1256 of  $<2.5$  phe, signal  $t_{10-90}$  duration in the range of up to  $\sim 2 \times 10^3$  ns (this upper edge results from  
 1257 coincidence window width (CWW) in coincidence building), are rejected.

1258 **Not a top-heavy signal**

1259 **Definition** A coincidence-found signal does not have a ”top-heavy” TBA regarding its signal area.  
 1260 A signal area dependent cut on TBA is used rather than a fixed TBA value is to account for the  
 1261 statistically fluctuation of the TBA at low signal area region, because the counts of photons that  
 1262 the top and bottom PMT detected are low.

1263 A ”top-heavy” TBA is defined as assuming the photon counts in top PMT (T) has a binomial  
 1264 distribution of parameter p (success probability in a single trial) and N (number of trials), the  
 1265 survival function (SF) at  $T = T_{\text{detected}}$  is smaller than  $10^{-5}$ :

$$SF(T_{\text{detected}}) \equiv P(T > T_{\text{detected}}) = \sum_{T_{\text{detected}}}^{\infty} P(T) dT < 10^{-5} \quad (1.32)$$

$$P(T; p, N) = \binom{N}{T} p^T (1-p)^{N-T} \quad (1.33)$$

1266 where  $p = B_{\text{detected}} \times 1.025/N$ ;  $T_{\text{detected}}$ ,  $B_{\text{detected}}$  are the top and bottom PMT measured signal  
 1267 area in phe; N is a sufficiently large number, chosen to be  $10^6$ . A low SF ( $T_{\text{detected}}$ ) indicates a high  
 1268 TBA.

1269 **Purpose** This is to make sure the signal of interest is not from (1)an anode cone event, (2) an  
 1270 anode muon cone event, (3) a PMT saturation event, or (4) a signal which misses part of the

recording in the bottom PMT (likely because of PMT dead time), as described in Section 1.8.2, Section 1.8.3, and Section 1.2. The effect of this selection is shown in Fig. 1.39e. The four categories of background events, correspond to the four “hot spots” in the figure.

The “hot spot” at signal area in the range of  $10^2$  phe to  $10^3$  phe, signal  $t_{10-90}$  duration in the range of  $\sim 10^3$  ns to  $10^4$  ns, and TBA  $\sim 0.3$ , results from EL light in the anode cone gamma radiation events. This “hot spot” is a combination of two smaller “hot spots”. The “hot spot” on the left (signal area  $\sim 2 \times 10^2$  phe, signal  $t_{10-90}$  duration  $\sim 2 \times 10^3$  ns, and TBA  $\sim 0.3$ ) may result from xenon X-rays events with typical energy of 33 keV in the anode cone . A xenon X-ray event in average can create  $\sim 1.5 \times 10^3$  drifted electrons <sup>4</sup>, which produce EL light in the high electric field region around the anodic grid wires. The “hot spot” on the right corresponds to other higher energy gamma radiation.

The location of this “hot spot” in the figure moves as varying  $\Delta V_{T-B}$ . As  $\Delta V_{T-B}$  increases, the electric field strength around the anodic grid wires also increases, which causes higher quantity of EL light production and signal area. At a low  $\Delta V_{T-B}$ , the small area signals cannot be rejected by this selection. Therefore, another signal selection based on the time correlation between the signal of primary scintillation and the signal of EL of these events, is carried out, as described later in Section 1.9.2.

The “hot spot” at signal area  $\sim 10^4$  phe, signal  $t_{10-90}$  duration  $\sim 10^4$  ns, results from EL light in the anode cone muon events. Similar to anode cone event from gamma radiation, these events also free drifted electrons, which produce EL light in the high electric field region around the anodic grid wires. The duration of these muon events are much longer than that of gamma events is because the longer ionization track of a muon event causes the drifted electrons created in the muon event arrive the anodic grid and produce EL light in a wider time span, as described in Section 1.8.3. The location of this “hot spot” in the figure moves to high signal area as increasing  $\Delta V_{T-B}$ . Therefore, the same argument holds for the signal selection based on the time correlation is used to reject these signals.

The “hot spot” strap at signal area  $\sim 10^4$  phe, signal  $t_{10-90}$  duration  $\sim 10^3$  ns, and TBA  $\sim 0.1$  results from high energy particle and muon events which saturate the DAQ. Because the average SPHE amplitude in the bottom PMT is higher, it exceeds the upper limit of the DAQ dynamic range at a smaller counts of SPHE than the top PMT. Therefore, the reconstructed signal area in the bottom PMT is lower after it reaches the DAQ saturation limit, which leads to a higher signal TBA because of this DAQ saturation issue.

The “hot spot” at TBA  $\sim 1$  results from missing part of the recording in the bottom PMT ,which is most likely because of PMT dead time. In these signals, the top PMT records the full event, when the bottom PMT only records the beginning or the end of the event. This results in a close to unity signal TBA.

---

<sup>4</sup>The average energy to create an electron-ion pair in xenon gas ( $W_{\text{ion}}$ ) is 22 eV for a gamma particle, estimated from  $W_{\text{ion}}$  for an alpha particle and a beta particle in Ref. [24–26].

1307 **Not a bottom-heavy signal**

1308 **Definition** A coincidence-found signal does not have a "bottom-heavy" TBA regarding its signal  
1309 area.

1310 Similar to the "top-heavy" TBA, a "bottom-heavy" TBA is defined as assuming the photon  
1311 counts in bottom PMT (B) has a binomial distribution of parameter p (success probability in a  
1312 single trial) and N (number of trials), the survival function (SF) at  $B = B_{\text{detected}}$  is smaller than  
1313  $10^{-5}$ :

$$SF(B_{\text{detected}}) \equiv P(B > B_{\text{detected}}) = \sum_{B_{\text{detected}}}^{\infty} P(B) dB < 10^{-5} \quad (1.34)$$

$$P(B; p, N) = \binom{N}{B} p^B (1-p)^{N-B} \quad (1.35)$$

1314 where  $p = T_{\text{detected}}/0.825/N$ ;  $T_{\text{detected}}$ ,  $B_{\text{detected}}$  are the top and bottom PMT measured signal area  
1315 in phe; N is a sufficiently large number, chosen to be  $10^6$ . A low SF ( $B_{\text{detected}}$ ) indicates a low TBA.

1316 **Purpose** This is to make sure the signal of interest is not a signal which misses part of the recording  
1317 in the top PMT (likely because of PMT dead time), as described in Section 1.2, which is similar to  
1318 the situation described in Section 1.9.1.

1319 The effect of this selection is shown in Fig. 1.39f. Signals with TBA close to -1 are rejected  
1320 because they are likely to be a signal missing part of the recording in the top PMT.

1321 In reverse polarity operation when the top grid is cathodic and the bottom grid is anodic, the  
1322 roles of "top-heavy" and "bottom-heavy" signal selections switches from normal polarity operation.

1323 **Not a extremely long duration signal**

1324 **Definition** A coincidence-found signal has a signal  $t_{01-99}$  duration 4 times longer than the pre-  
1325 dicted EL duration from the estimated average EL region electric field and Eqn. 1.17.

1326 **Purpose** This is to make sure the signal of interest is not a muon event or a multiple scatter event,  
1327 as described in Section 1.8.3, and Section 1.8.2. The effect of this selection is shown in Fig. 1.39g.  
1328 The "hot spot" at signal area  $\sim 10^4$  phe, signal  $t_{10-90}$  duration  $\sim 3 \times 10^3$  ns, and TBA  $\sim 0$  results  
1329 from EL region muon events.

1330 **Not a right-angle triangle shape signal**

1331 may be remove this cut.

1332 **Definition** A coincidence-found signal does not have a large skewness of signal waveform and a  
1333 higher photon rate at the beginning of the signal than that at the end of the signal.

1334        The skewness statistics of a electron emission signal waveform is close to zero because the shape is  
 1335        close to a uniform distribution, when the skewness of a right-angle triangle shape is  $\sim 0.96$ . Therefore,  
 1336        this statistics is used to distinguish the right-angle triangle waveform. The skewness statistics  
 1337        between 5th percentile time and 95th percentile time ( $\text{skew}_{0595}$ ) and the skewness statistics between  
 1338        15th percentile time and 85th percentile time ( $\text{skew}_{1585}$ ) are used to effect from the outlier. A large  
 1339        skewness is defined as  $\text{skew}_{0595} > 0.2$  and  $\text{skew}_{1585} > 0.1$ .

1340        Since the skewness statistics are sometimes effected by outlier, another method is carried out  
 1341        based on comparing the photon rate the beginning of the signal and that at the end of the signal  
 1342        as a supplement. A higher photon rate at region A than region B is defined below. The detected  
 1343        signal area and duration of region A and region B is noted as  $A_{\text{detected}}$ ,  $B_{\text{detected}}$ ,  $t_A$ ,  $t_B$ . Assuming  
 1344        the photon counts in region A in a simulation ( $A_{\text{sim}}$ ) has a binomial distribution of parameter p  
 1345        (success probability in a single trial) and N (number of trials), the survival function (SF) at  $A_{\text{sim}} =$   
 1346         $A_{\text{detected}}$  is smaller than  $10^{-6}$ :

$$SF(A_{\text{detected}}) \equiv P(A_{\text{sim}} > A_{\text{detected}}) = \sum_{A_{\text{detected}}}^{\infty} P(A) dA < 10^{-6} \quad (1.36)$$

$$P(A; p, N) = \binom{N}{A} p^A (1-p)^{N-A} \quad (1.37)$$

1347        where  $p = 1.2 \times B_{\text{detected}} \times t_A / t_B / N$ ; N is a sufficiently large number, chosen to be  $10^6$ . A low SF  
 1348        ( $A_{\text{detected}}$ ) indicates a higher photon rate at region A than region B. If the photon rate between 5th  
 1349        percentile time and 15th percentile time, or between 300 ns and 800 ns since the recording start time  
 1350        of the event is higher than that of between 50th percentile time and 85th percentile time, we define  
 1351        the signal has the photon rate at the beginning is higher than that at the end.

1352        **Purpose** This is to make sure the signal of interest is not a EL region muon event, or a S1 S2  
 1353        event in the EL region, as described in Section 1.8.3, and Section 1.8.2. The muon events happening  
 1354        between the grid rings has a lower light production and light collection than those happing between  
 1355        the grid wires. These grid ring region events usually does have a "long tail" in the signal because the  
 1356        muon track does not pass the anode region creating free drifted electrons. These two reasons make  
 1357        it hard to distinguish muon events happening between the grid rings by a long signal duration or a  
 1358        large signal area as that between the grid wires. The effect of this selection is shown in Fig. 1.39h.  
 1359        Therefore, this pulse selection is used.

1360        **Not an S1 S2 like signal**

1361        **may be remove this cut.**

1362 **Definition** A coincidence-found signal does not have a low photon rate in the range of 300 ns to  
1363 800 ns since the recording start time of the signal.

1364 Since in this type of events, the photon rate is low between the S1 and S2 signal, we compare the  
1365 photon rate in the time region immediately after S1 to other time region to distinguish these events.  
1366 An S1 signal usually lasts less than 180 ns, therefore ending 300 ns after the recording start time  
1367 of the signal, because of the pre-delay recording described in Section ???. The compared region are  
1368 between 800 ns since the recording start time of the signal and 90th percentile time, between 25th  
1369 percentile time and 90th percentile time, between 50th percentile time and 75th percentile time, and  
1370 between 50th percentile time and 95th percentile time.

1371 **Purpose** This is to make sure the signal of interest is not from an S1 S2 event in the cathode  
1372 corner, as described in Section 1.8.2. The effect of this selection is shown in Fig. 1.39i.

1373 **Not a saturated signal**

1374 **Definition** A coincidence-found signal does not have any PMT saturated.

1375 **Purpose** This is to make sure the signal of interest is not from a particle or muon event that have  
1376 large signal area, unlike electron emission signal which usually does not produce large signal that  
1377 saturate any PMT. The effect of this selection is shown in Fig. 1.39j.

1378 **Not a long duration signal**

1379 **Definition** A coincidence-found signal has a signal  $t_{10-90}$  duration 1.5 times longer than the  
1380 predicted electron emission signal signal  $t_{10-90}$  duration from the estimated average EL region  
1381 electric field and Eqn. 1.17.

1382 **Purpose** This is to make sure the signal of interest is not a muon event or a multiple scatter event,  
1383 as described in Section 1.8.3, and Section 1.8.2. The effect of this selection is shown in Fig. 1.39k.

1384 **Not a short duration signal**

1385 **Definition** A coincidence-found signal has a signal  $t_{10-90}$  duration shorter than 0.64 times the  
1386 predicted electron emission signal duration from the estimated average EL region electric field and  
1387 Eqn. 1.17, and shorter than 5 sigma from the predicted electron emission signal signal  $t_{10-90}$  duration  
1388 duration.

1389 **Purpose** This is to make sure the signal of interest is not a grid ring region event (likely originating  
1390 from muon or particle), as described in Section 1.8.3, and Section 1.8.2. The effect of this selection  
1391 is shown in Fig. 1.39l. An event happening in the grid ring region has a low light collection therefore

1392 hard to be distinguished by its shape. However, it usually has a shorter duration, therefore can be  
1393 rejected by this pulse selection.

### 1394 1.9.2 Signal selections based on previous signals

1395 Previous signals may correlate with the later signals. There are two major types of correlation  
1396 signals. One type of correlation signals is between primary scintillation light and EL light from  
1397 the ionization electrons. In an anode cone region event, primary scintillation light are produced  
1398 immediately after a particle interaction, when the ionization electrons take time to drift to the  
1399 anodic grid to produce EL light, as described in Section 1.8.2 and Section 1.8.3. Therefore, we  
1400 can the correlation between primary scintillation light and EL light to determine these events. The  
1401 second type of correlation signals is fluorescence signals succeeding large-area signals, as described in  
1402 Section 1.8.4. Since the fluorescence signals may look like electron emission signals, the correlation  
1403 between the fluorescence signals and the large-area signals is the only method to distinguish these  
1404 fluorescence signals. Therefore, we use signal selections based on the previous signal area to reject  
1405 these background events.

1406 Moreover, previous signals also introduce PMT dead time issue, as described in Section 1.2.  
1407 PMT dead time issue causes an incomplete recording of the signals immediately following another  
1408 signal. To address this issue, we subtract a segment of time after each recorded pulse from the live  
1409 time of study and eliminate all signals that is recorded in this time period. Therefore, we use signal  
1410 selections based on the previous signal duration to reject these background events.

1411 These two signal selections previously mentioned may veto good candidate electron emission  
1412 signals . Therefore, the survival ratio of the candidate electron emission signals from these signal  
1413 selection is estimated.

#### 1414 Veto based on signal area of previous signal

1415 **Definition** A coincidence-found signal (1) is not following another pulse in any PMT with pulse  
1416 area larger than 3.5 phe within  $150\ \mu s$ , (2) is not following another pulse in any PMT with pulse  
1417 area larger than  $10^3$  phe within  $300\ \mu s$ , and (3) is not following another pulse in any PMT with pulse  
1418 area larger than  $10^4$  phe within  $1000\ \mu s$ .

1419 **Purpose** The 100-us veto is to make sure that the signal of interest is not the EL light from an  
1420 anode cone region event, as described in Section 1.8.2 and Section 1.8.3. Primary scintillation light  
1421 signal in an anode cone region event mostly has its pulse area larger than 3 phe in at least one  
1422 PMT. Therefore, this veto can reject the anode cone region event background. The 200-us veto and  
1423 the 1000-us veto are to make sure that the signal of interest is not fluorescence signals succeeding  
1424 large-area signals, as described in Section 1.8.4. With the segment of time cut off, the fluorescence  
1425 induced SPHE rate is below  $10^4$  Hz, therefore the rate of accidental coincidence with more than

1426 3 phe is below 4 Hz for the chosen CWW. The effect of this selection is shown in Fig. 1.39m. Even  
1427 though not shown in this figure, this selection is also effective in removing the “hot spot” at signal  
1428 area in the range of  $10^2$  phe to  $10^3$  phe, signal  $t_{10-90}$  duration in the range of  $\sim 10^3$  ns to  $10^4$  ns, and  
1429 TBA  $\sim 0.3$ , resulting from EL light in the anode cone gamma radiation events, which is shown in  
1430 Fig. 1.39e. This selection is necessary when  $\Delta V_{T-B}$  is small because the signal selection based on  
1431 TBA is less effective in such  $\Delta V_{T-B}$ , as discussed in Section 1.9.1 .

1432 **Veto based on signal area of previous signal**

1433 **Definition** A coincidence-found signal (1) is not following another pulse in any PMT within  $10\ \mu s$ ,  
1434 (2) is not following another pulse in any PMT with pulse duration longer than  $3\ \mu s$  within  $20\ \mu s$ , (3)  
1435 is not following another pulse in any PMT with pulse duration longer than  $10\ \mu s$  within  $40\ \mu s$ , and  
1436 (4) is not following another pulse in any PMT with pulse duration longer than  $30\ \mu s$  within  $200\ \mu s$ .

1437 **Purpose** This is to make sure the PMT dead time issue is addressed. The effect of this selection  
1438 is shown in Fig. ??.

1439 **Survival ratio of the candidate electron emission signals**

1440 These two cuts previously mentioned may veto good candidate electron emission signals . Therefore,  
1441 survival ratio of the candidate electron emission signals need to be estimated. The survival ratio is  
1442 estimated by how much is the fraction of a careful selection of coincidence pulses survive these cuts.  
1443 The careful selection of coincidence pulses also need to be uncorrelated from preceding pulses. The  
1444 careful selection is the coincidence pulses in  $t_{25-75}$  range 0 ns to 200 ns, pulse area range 25 phe to  
1445 250 phe. This selection is a conservative selection of S1 pulses that has few contaminations from other  
1446 sources. Since S1 is from the primary light production of external particle sources, this selection of  
1447 pulses are uncorrelated from preceding pulses. Thus, it can be used for estimating the survival ratio.  
1448 The survival ratio is called quiet fraction (QF). For normal operation, QF is in the range of 0.6 to  
1449 0.9. Details of this physical sources of S1 pulses will be discussed in the following Section. 1.9.1: S1  
1450 conservative population.

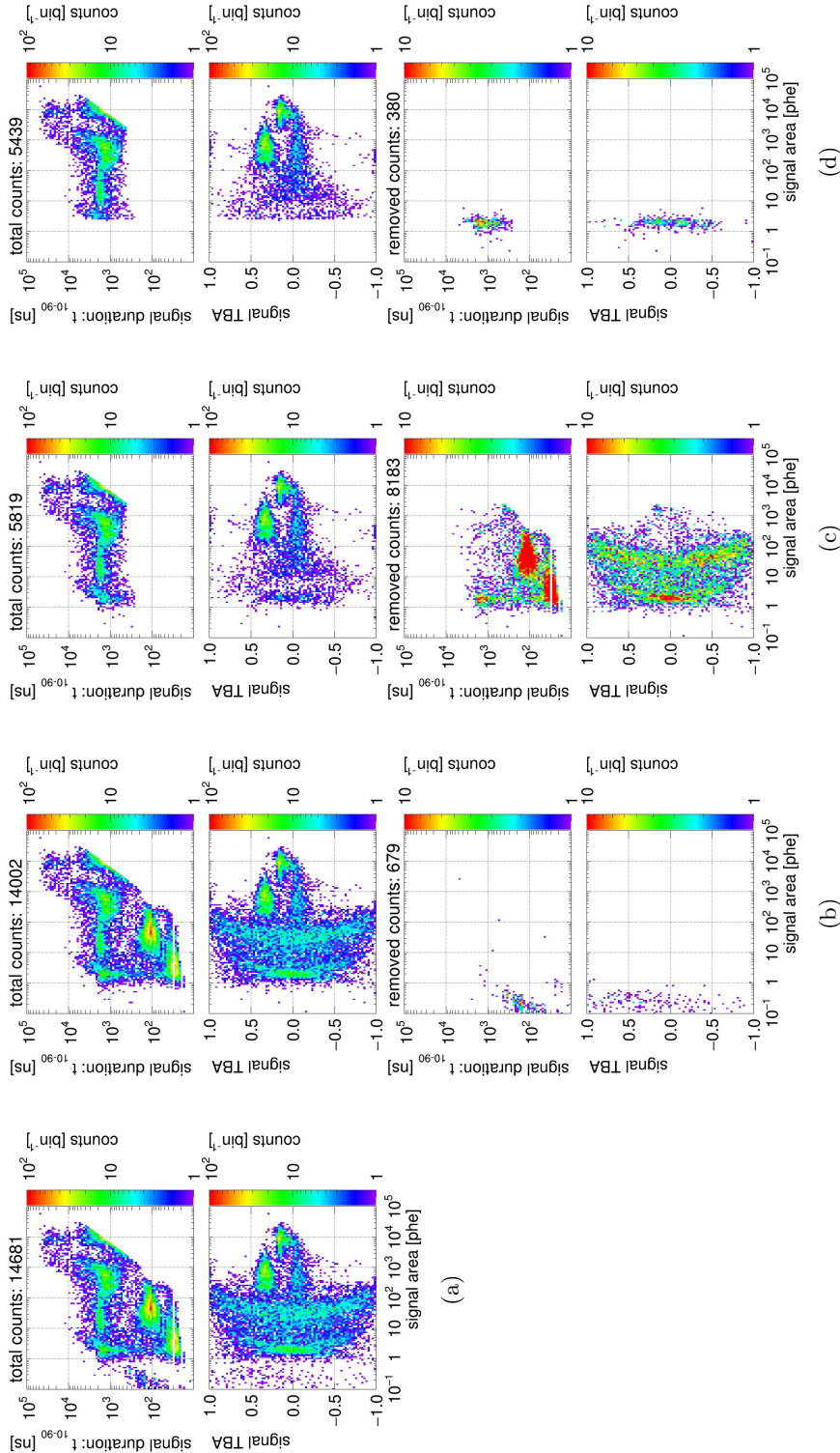


Figure 1.39: *Gas Test* signal selection (part 1): (row one) distribution of  $t_{10-90}$  duration vs area after signal selections; (row two) distribution of TBA vs area after signal selections; (row three) distribution of  $t_{10-90}$  duration vs area of removed signals; (row four) distribution of TBA vs area of removed signals; (a) coincidence event building; (b) applying signal selections up to “not a noise-like signal”; (c) applying signal selections up to “not a narrow (S1-like) signal”; (d) applying signal selections up to “not a two-SPHE accidental coincidence signal”. Data were taken at 2017-12-8 14:02, with grid voltages  $V_T$  and  $V_B$  at +6 kV and -6 kV, operating gas density at 0.137 mol L<sup>-1</sup>. The duration of data taking is 180.09 s.

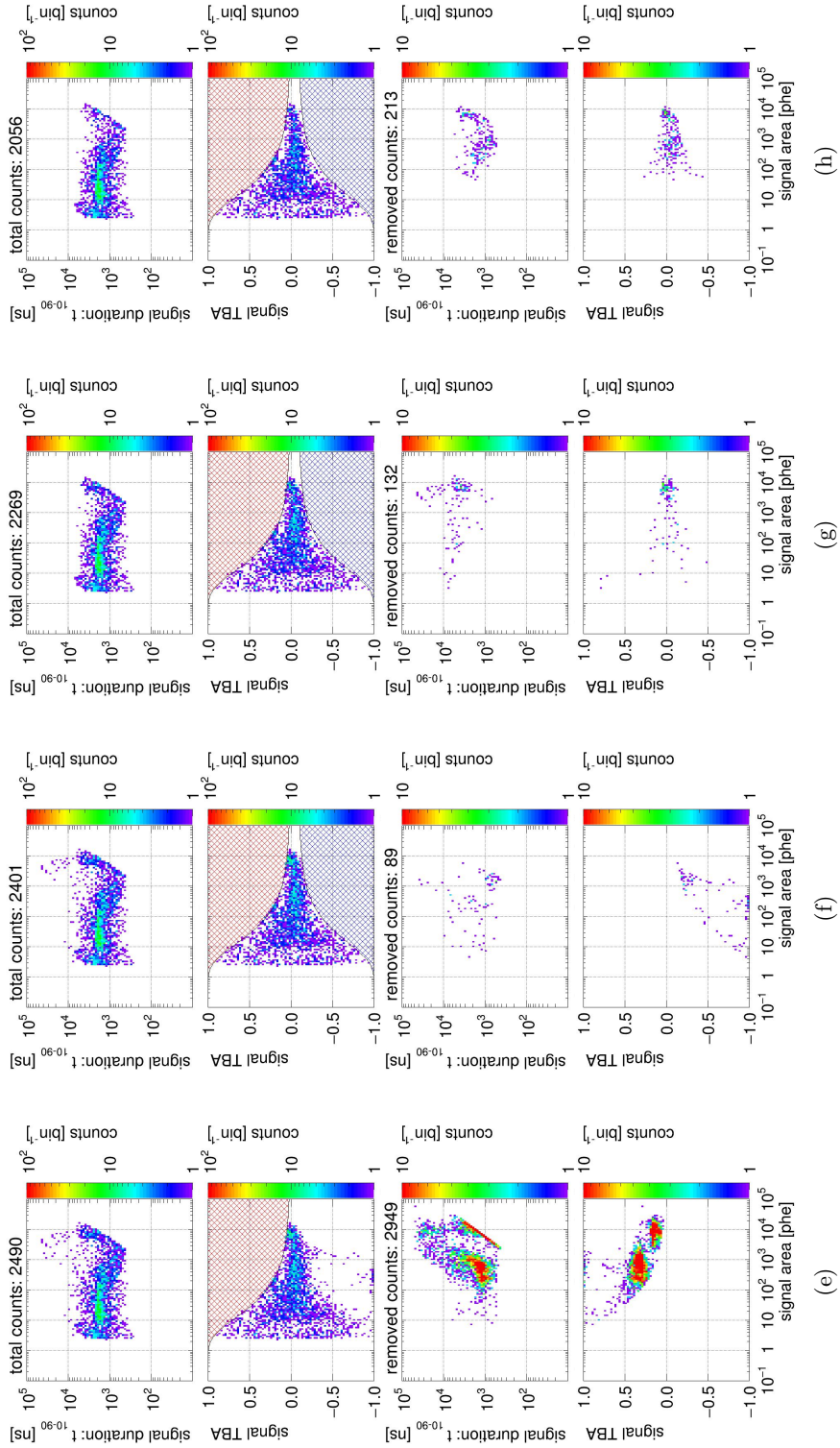


Figure 1.39: *Gas Test* signal selection (part 2): (row one) distribution of  $t_{10-90}$  duration vs area after signal selections; (row two) distribution of TBA vs area after signal selections; (row three) distribution of  $t_{10-90}$  duration vs area of removed signals; (row four) distribution of TBA vs area of removed signals; (e) applying signal selections up to “not a top-heavy signal”; (f) applying signal selections up to “not a bottom-heavy signal”; (g) applying signal selections up to “not a extremely long duration signal”; (h) applying signal selections up to “not a right-angled triangle shape signal”. The red hatched shaded area indicates the “top-heavy” region. The blue shaded area indicates the “bottom-heavy” region. Data were taken at 2017-12-8 14:02, with grid voltages  $V_T$  and  $V_B$  at +6 kV and -6 kV, operating gas density at 0.137 mol L<sup>-1</sup>. The duration of data taking is 180.09 s.

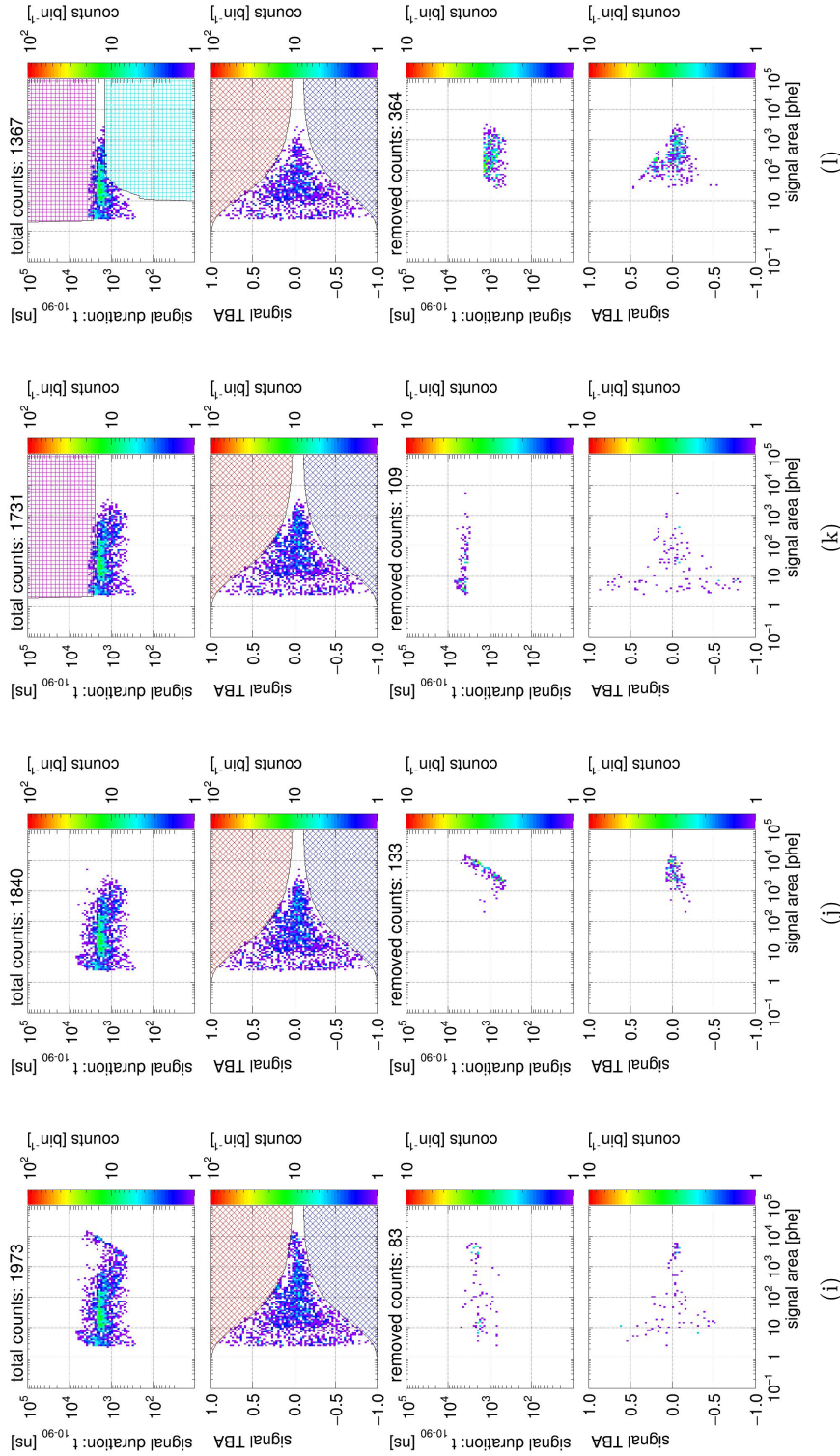


Figure 1.39: *Gas Test* signal selection (part 3): (row one) distribution of  $t_{10-90}$  duration vs area after signal selections; (row two) distribution of TBA vs area after signal selections; (row three) distribution of  $t_{10-90}$  duration vs area of removed signals; (row four) distribution of TBA vs area of removed signals; (i) applying signal selections up to “not an S1 S2 like signal”; (j) applying signal selections up to “not a saturated signal”; (k) applying signal selections up to “not a long duration signal”; (l) applying signal selections up to “not a short duration signal”. The red hatched shaded area indicates the “top-heavy” region. The blue shaded area indicates the “bottom-heavy” region. The magenta hatched shaded area indicates the “long duration” region. The cyan hatched shaded area indicates the “short duration” region. Data were taken at 2017-12-8 14:02, with grid voltages  $V_T$  and  $V_B$  at +6 kV and -6 kV, operating gas density at  $0.137 \text{ mol L}^{-1}$ . The duration of data taking is 180.09 s.

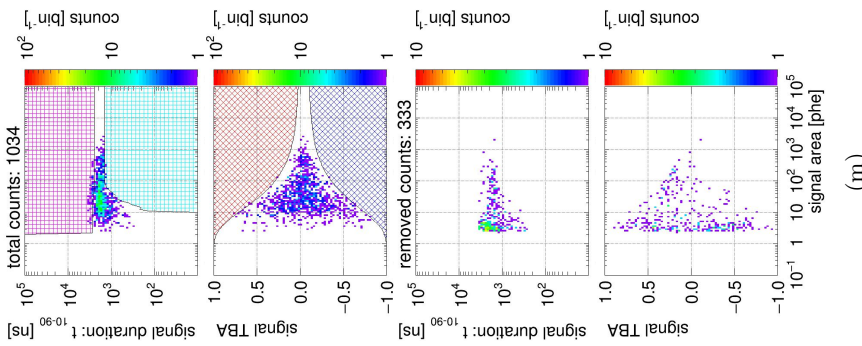


Figure 1.39: *Gas Test* signal selection (part 4): (row one) distribution of  $t_{10-90}$  duration vs area after signal selections; (row two) distribution of TBA vs area after signal selections; (row three) distribution of  $t_{10-90}$  duration vs area of removed signals; (row four) distribution of TBA vs area of removed signals; (m) applying signal selections up to “time veto selection 1”. The red hatched shaded area indicates the “top-heavy” region. The blue shaded area indicates the “bottom-heavy” region. The magenta hatched shaded area indicates the “long duration” region. The cyan hatched shaded area indicates the “short duration” region. Data were taken at 2017-12-8 14:02, with grid voltages  $V_T$  and  $V_B$  at +6 kV and -6 kV, operating gas density at 0.137 mol L<sup>-1</sup>. The duration of data taking is 180.09 s.

<sup>1451</sup> **1.9.3 Signal selections varying  $\Delta V_{T-B}$  and operating gas density**

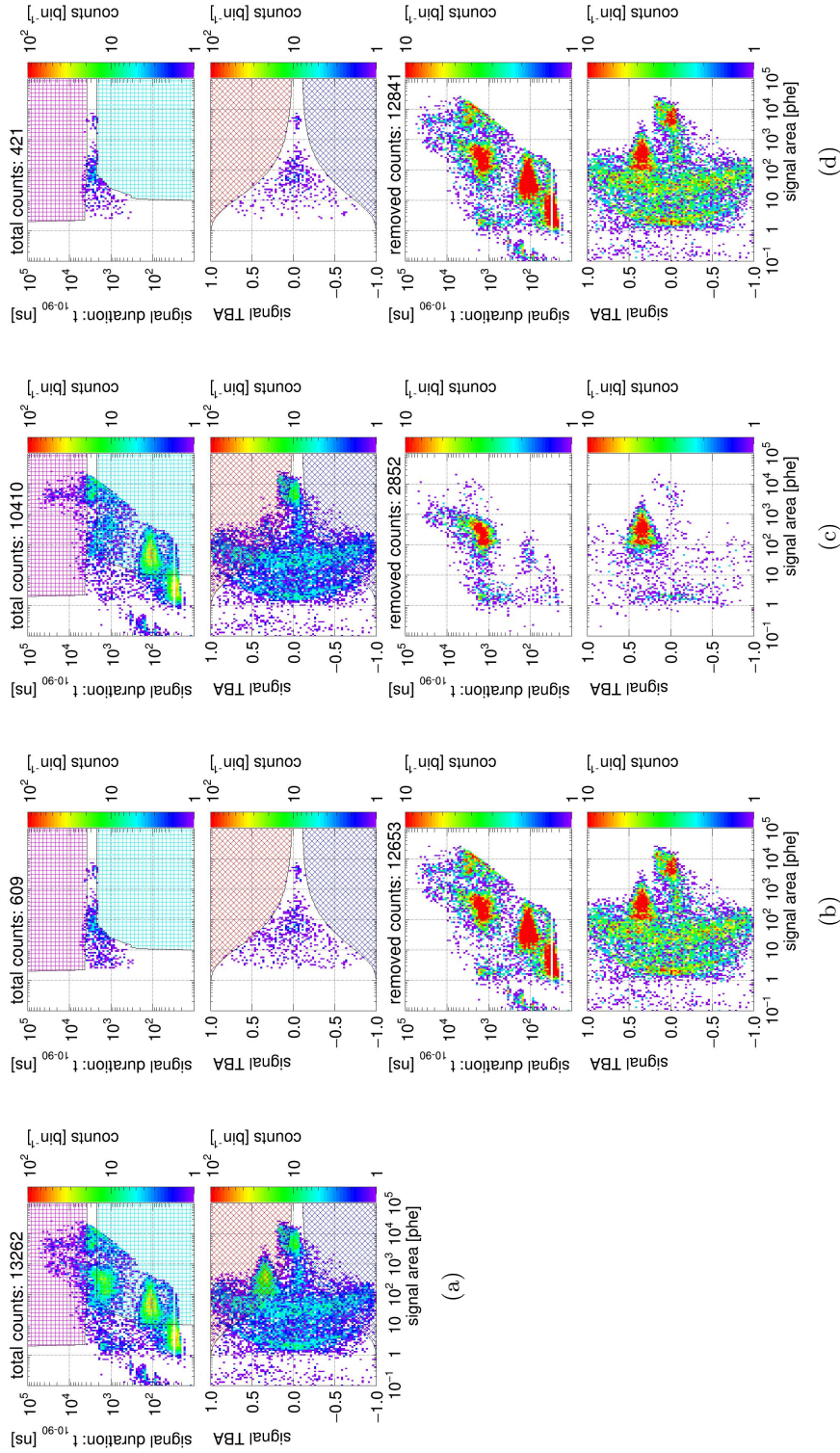


Figure 1.40: *Gas Test* signal selection with  $\Delta V_{T-B}$  at 8 kV, operating gas density at  $0.137 \text{ mol L}^{-1}$ : (row one) distribution of  $t_{10-90}$  duration vs area after signal selections; (row two) distribution of TBA vs area after signal selections; (row three) distribution of  $t_{10-90}$  duration vs area of removed signals; (row four) distribution of TBA vs area of removed signals; (a) coincidence event building; (b) applying signal selections based on signal shape; (c) applying signal selections based on the previous signals; (d) applying signal selections based on signal shape and based on the previous signals. The red hatched shaded area indicates the “top-heavy” region. The blue shaded area indicates the “bottom-heavy” region. The magenta hatched shaded area indicates the “long duration” region. The cyan hatched shaded area indicates the “short duration” region. Data were taken at 2017-12-8 13:43, with grid voltages  $V_T$  and  $V_B$  at +4 kV and -4 kV. The duration of data taking is 179.95 s.

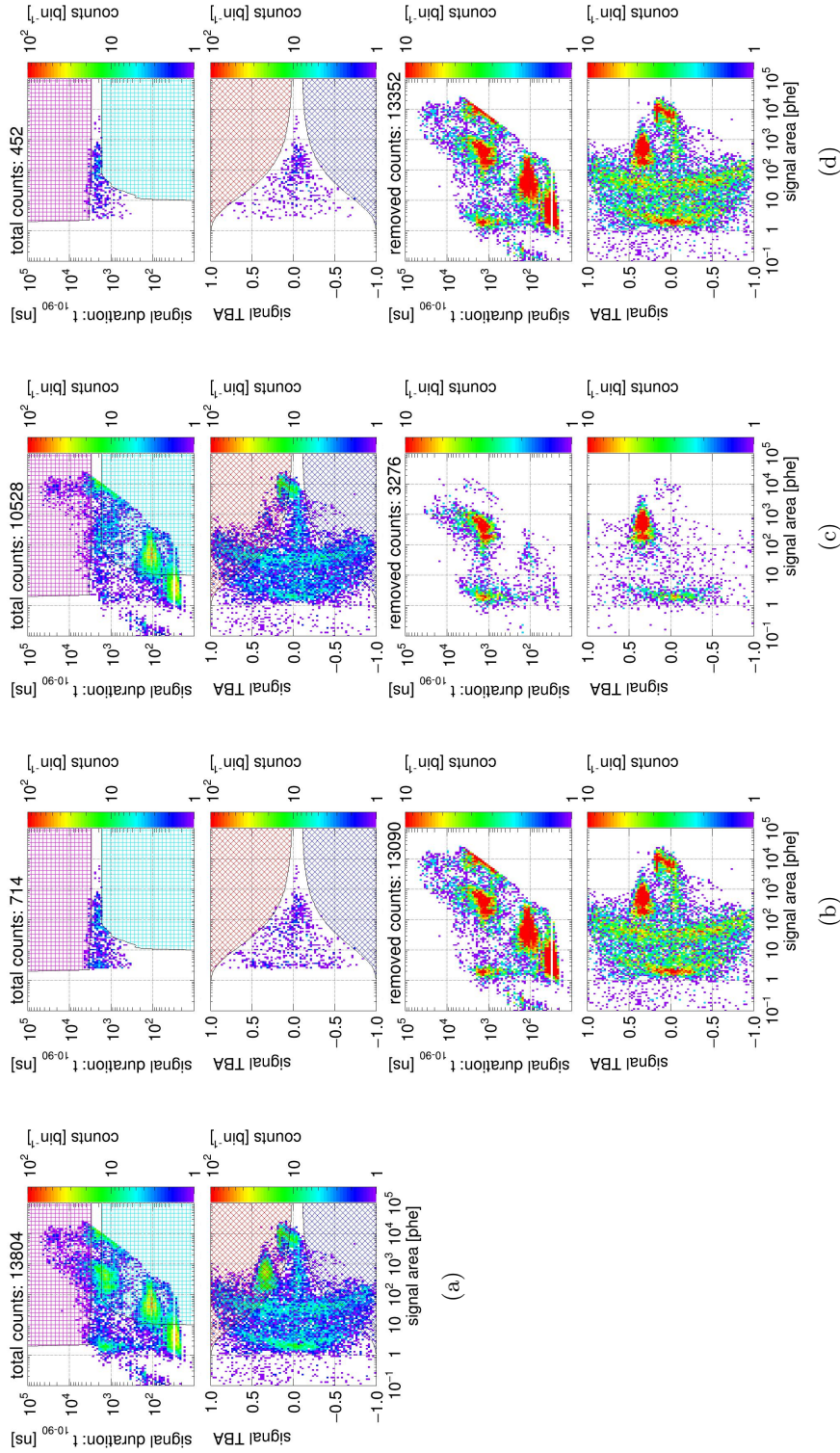


Figure 1.41: *Gas Test* signal selection with  $\Delta V_{T-B}$  at 10kV, operating gas density at  $0.137 \text{ mol L}^{-1}$ : (row one) distribution of  $t_{10-90}$  duration vs area after signal selections; (row two) distribution of TBA vs area after signal selections; (row three) distribution of  $t_{10-90}$  duration vs area of removed signals; (row four) distribution of TBA vs area of removed signals; (a) coincidence event building; (b) applying signal selections based on signal shape; (c) applying signal selections based on the previous signals; (d) applying signal selections based on signal shape and based on the previous signals. The red hatched shaded area indicates the “top-heavy” region. The blue shaded area indicates the “bottom-heavy” region. The magenta hatched shaded area indicates the “long duration” region. The cyan hatched shaded area indicates the “short duration” region. Data were taken at 2017-12-8 13:52, with grid voltages  $V_T$  and  $V_B$  at  $+5 \text{ kV}$  and  $-5 \text{ kV}$ . The duration of data taking is 180.11 s.

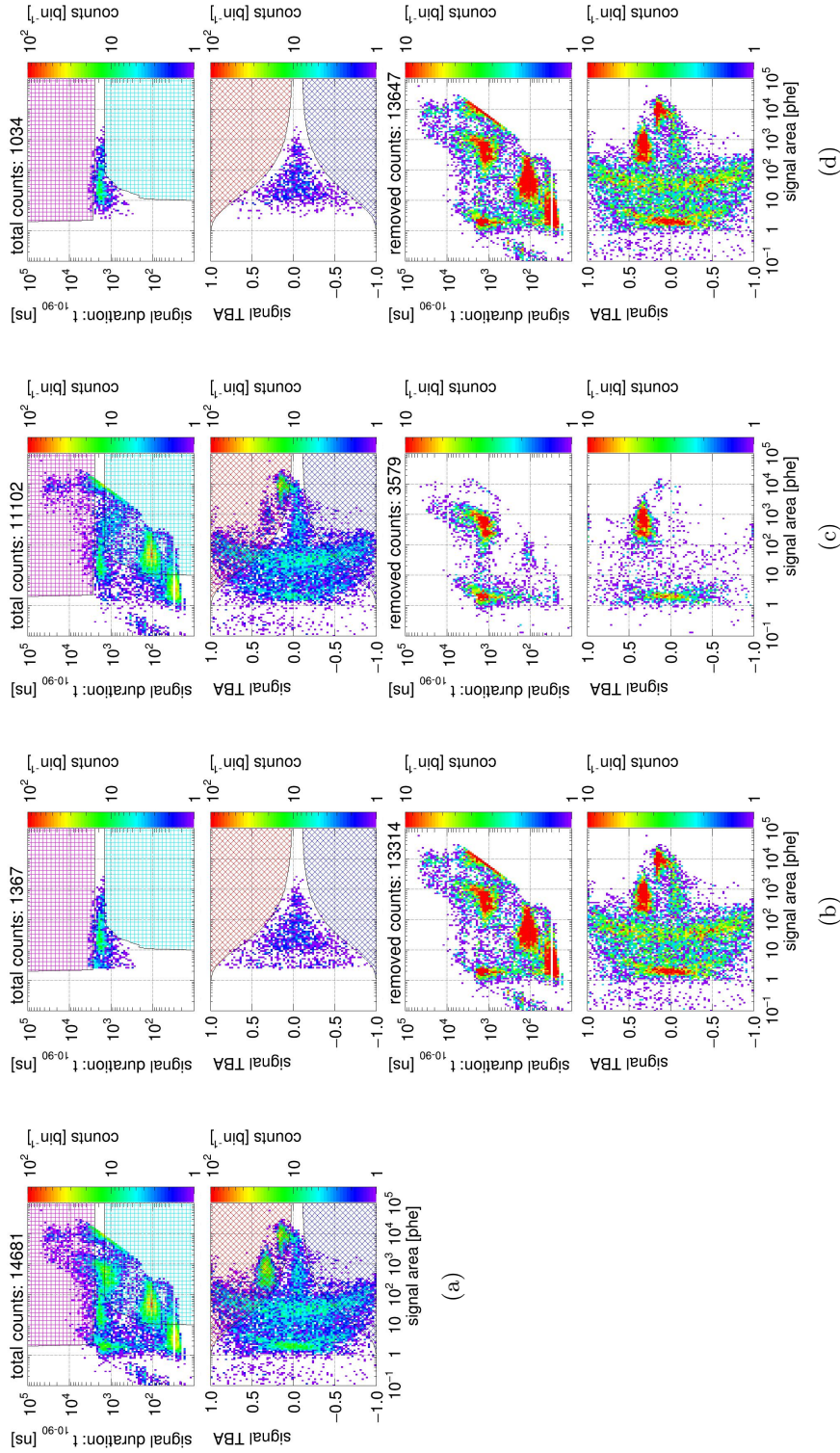


Figure 1.42: *Gas Test* signal selection with  $\Delta V_{T-B}$  at 12kV, operating gas density at  $0.137 \text{ mol L}^{-1}$ : (row one) distribution of  $t_{10-90}$  duration vs area after signal selections; (row two) distribution of TBA vs area after signal selections; (row three) distribution of  $t_{10-90}$  duration vs area of removed signals; (row four) distribution of TBA vs area of removed signals; (a) coincidence event building; (b) applying signal selections based on signal shape; (c) applying signal selections based on the previous signals; (d) applying signal selections based on signal shape and based on the previous signals. The red hatched shaded area indicates the “top-heavy” region. The blue shaded area indicates the “bottom-heavy” region. The magenta hatched shaded area indicates the “long duration” region. The cyan hatched shaded area indicates the “short duration” region. Data were taken at 2017-12-8 14:02, with grid voltages  $V_T$  and  $V_B$  at  $+6 \text{ kV}$  and  $-6 \text{ kV}$ . The duration of data taking is 180.09s.

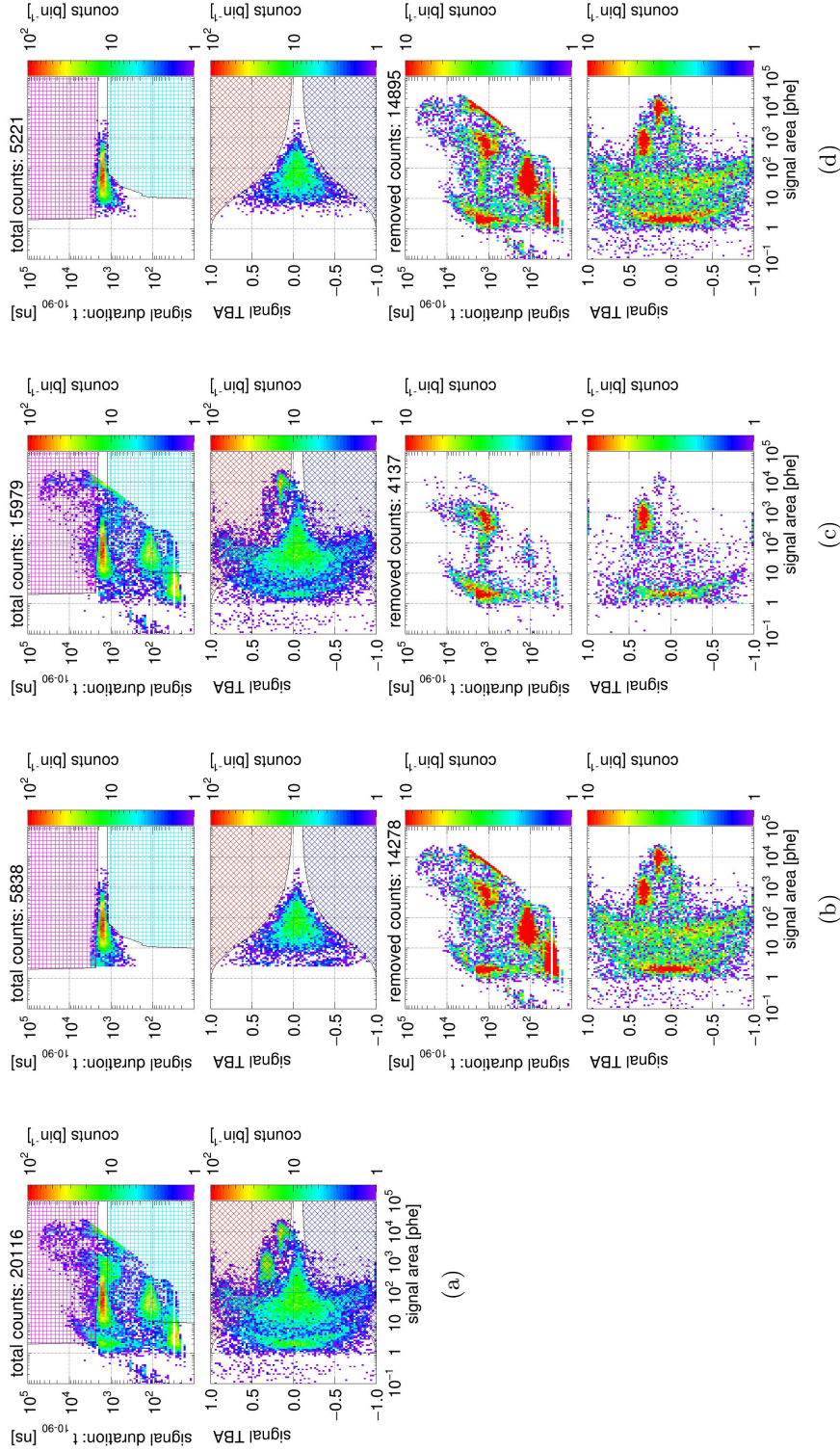


Figure 1.43: *Gas Test* signal selection with  $\Delta V_{T-B}$  at 14kV, operating gas density at  $0.137 \text{ mol L}^{-1}$ : (row one) distribution of  $t_{10-90}$  duration vs area after signal selections; (row two) distribution of TBA vs area after signal selections; (row three) distribution of  $t_{10-90}$  duration vs area of removed signals; (row four) distribution of TBA vs area of removed signals; (a) coincidence event building; (b) applying signal selections based on signal shape; (c) applying signal selections based on the previous signals; (d) applying signal selections based on signal shape and based on the previous signals. The red hatched shaded area indicates the “top-heavy” region. The blue shaded area indicates the “bottom-heavy” region. The magenta hatched shaded area indicates the “long duration” region. The cyan hatched shaded area indicates the “short duration” region. Data were taken at 2017-12-8 14:21, with grid voltages  $V_T$  and  $V_B$  at  $+7\text{kV}$  and  $-7\text{kV}$ . The duration of data taking is 180.01 s.

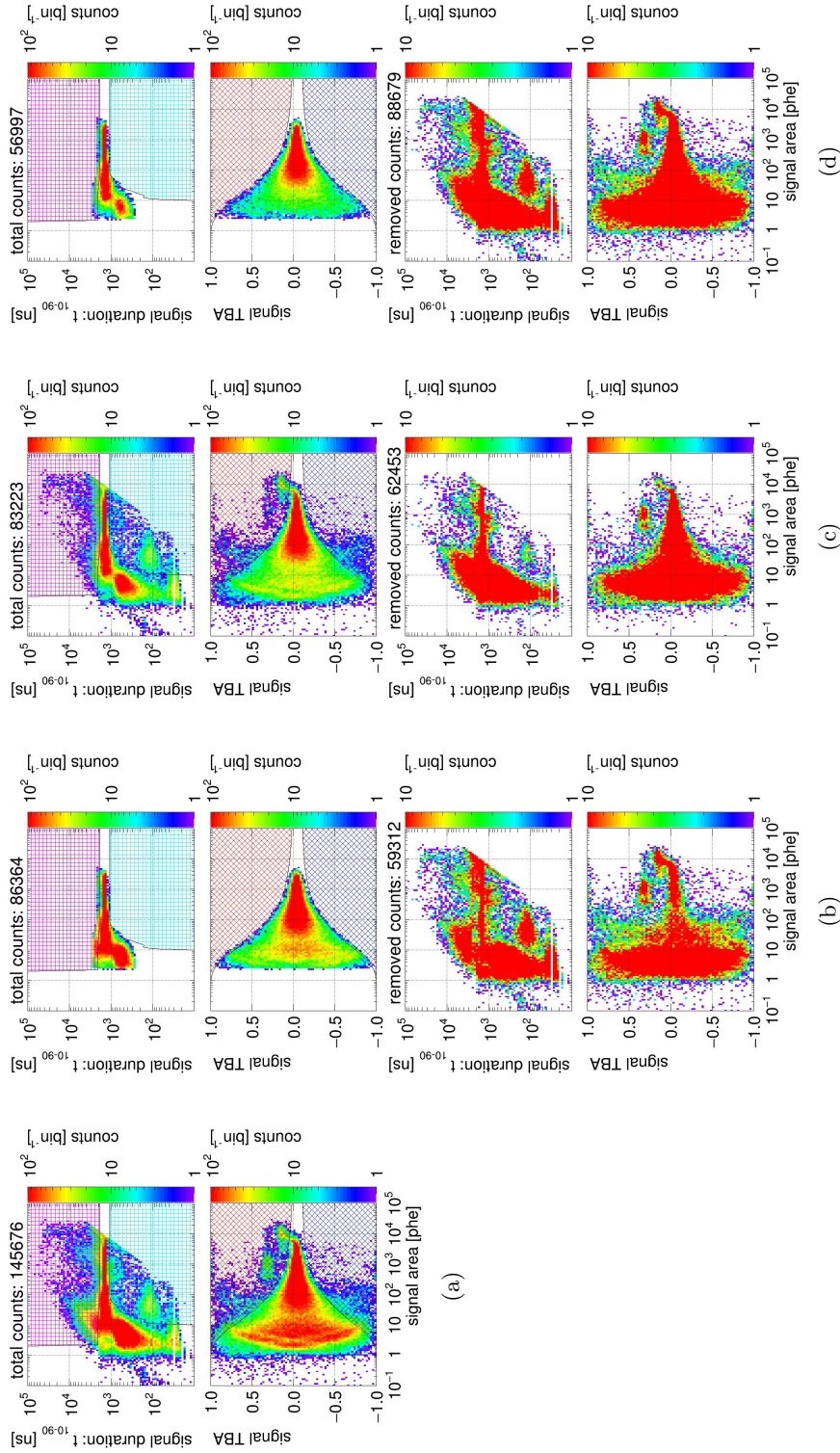


Figure 1.44: *Gas Test* signal selection with  $\Delta V_{T-B}$  at 16kV, operating gas density at  $0.137 \text{ mol L}^{-1}$ : (row one) distribution of  $t_{10-90}$  duration vs area after signal selections; (row two) distribution of TBA vs area after signal selections; (row three) distribution of  $t_{10-90}$  duration vs area of removed signals; (row four) distribution of TBA vs area of removed signals; (a) coincidence event building; (b) applying signal selections based on signal shape; (c) applying signal selections based on the previous signals; (d) applying signal selections based on signal shape and based on the previous signals. The red hatched shaded area indicates the “top-heavy” region. The blue shaded area indicates the “bottom-heavy” region. The magenta hatched shaded area indicates the “long duration” region. The cyan hatched shaded area indicates the “short duration” region. Data were taken at 2017-12-8 14:42, with grid voltages  $V_T$  and  $V_B$  at +8kV and -8kV. The duration of data taking is 180.10s.

1452 a figure with  $\Delta V_{T-B} = -8\text{kV}$  a figure with  $\Delta V_{T-B} = 12\text{kV}$ , at 2 bar

## 1453 1.10 Evaluation

### 1454 1.10.1 Simulations

1455 Simulations for electron emission signal is

1456 Detailed discussions of the calculation of the electric field is in Appendix ??.

1457 The evaluation of these cuts are estimated by simulations. Cut efficiency is used to indicate the  
1458 quality of the cuts. With evaluating the ratio between the simulated electron emission signal passing  
1459 cut and the total counts of simulations, the cut efficiency is estimated as

$$\text{cut efficiency} \approx \frac{\# \text{ pulses pass cut}}{\# \text{ simulations}} \quad (1.38)$$

1460 Higher cut efficiency indicates that we are capable of preserving more electron emission signals.  
1461 Cut efficiency are evaluated with different detector operation conditions, such as gas density and  
1462 grids operation voltage. Since the simulated electron emission signal that I used to evaluate the  
1463 cuts have a few discrepancies from the real electron emission signal, the cut efficiency will be not be  
1464 exactly accurate. Even though this estimate is only an approximation, the overall cut efficiency are  
1465 not wildly off.

### 1466 1.10.2 Summary

1467 To summarize the cuts that I used, to be an electron emission signal candidate, a pulse should satisfy  
1468 these conditions. It should

- 1469 • contain coincidence pulse in both PMTs,
- 1470 • uncorrelated from preceding pulses,
  - 1471 – not have any preceding pulse in the previous  $100\ \mu\text{s}$ ,
  - 1472 – not have any preceding large pulse in the previous 10 ms,
- 1473 • have the correct pulse shape,
  - 1474 – not noise like,
  - 1475 – not have pulse heavily concentrated only in one of the PMTs,
  - 1476 – have longer than single PHE pulse area or positive pulse duration in at least one PMT,
  - 1477 – not “Cherenkov radiation” like,

- 1478           – not S1 like,
- 1479           – not muon like,
- 1480           – not S1 S2 like,
- 1481           –  $t_{10-90}$  (signal  $t_{10-90}$  duration) matches prediction from electron drift time between the  
1482           top and bottom grids,
- 1483       ● not saturate any PMT (this is required for analysis with condition that gas pressure higher  
1484           than 1 bara).

1485 **Appendix A**

1486 ***Gas Test* RQ documentation**

1487 This chapter summarizes the definitions of the RQs that are used for analysis in *Gas Test* analysis.

RQ name	shape	type	unit	default
‘aft_tXX’	array (L,)	float32	ns	nan
	Time difference between the start time of the pulse and the integrated pulse area reach XX% of the total area of pulse. XX=05,25,75,95.			
‘aft_t0’, ‘aft_t1’, ‘aft_t2’.	array (L,)	float32	ns	nan
	equivalent to ‘aft_t01’, ‘aft_t50’, ‘aft_t99’.			
‘arearq’	scalar	string		‘waveareas_trim_end’
	RQ used to compute coincidence pulse area.			
‘AmpThreshold’	scalar	float32	mV	2.5
	The threshold value for computing ‘above_threshold’ RQs.			
‘baselines’	array (L,)	float32	mV	nan
	Pulse baseline voltage.			
‘channels’	array (L,)	uint32		
	Pulse channel number.			
‘coin_pulse_amplitudes’	array (N,C)	float32	mV	nan
	Coincidence pulse amplitudes in each channel.			
‘coin_pulse_amplitudes_neg’	array (N,C)	float32	mV	nan
	Coincidence pulse negative amplitudes in each channel.			
‘coin_pulse_areas’	array (N,C)	float32	mV ns	nan
	Coincidence pulse areas in each channel.			

Continued on next page

RQ name	shape	type	unit	default
‘coin_pulse_areas_neg’	array (N,C)	float32	mV ns	nan
	Coincidence pulse negative areas in each channel.			
‘coin_pulse_areas_norm’	array (N,C)	float32	phe	nan
	Coincidence pulse area in each channel.			
‘coin_pulse_areas_post_TTus’	array (N,C)	float32	phe	0
	Pulse area of TT us after the stop time of a coincidence pulse. TT=100,50,20,10.			
‘coin_pulse_areas_pre_TTus’	array (N,C)	float32	phe	0
	Pulse area of TT us before the start time of a coincidence pulse. TT=100,50,20,10.			
‘coin_pulse_areas_section1’	array (N,C)	float32	phe	0
	Pulse area of a coincidence pulse of section1, which is defined by ‘pulse1_start’ and ‘pulse1_stop’.			
‘coin_pulse_areas_section2’	array (N,C)	float32	phe	0
	Pulse area of a coincidence pulse of section2, which is defined by ‘pulse2_start’ and ‘pulse2_stop’.			
‘coin_pulse_areas_sum’	array (N,)	float32	phe	nan
	Coincidence pulse total area.			
‘coin_pulse_areas_tXX’	array (N,)	float32	ns	nan
	Time difference between the start time of the coincidence pulse and the integrated coincidence pulse area reach XX% of the total area of the coincidence pulse. XX=01,05,10,15,25,50,75,85,90,95,99.			
‘coin_pulse_areas_tXXYY’	array (N,)	float32	ns	nan
	'coin_pulse_areas_tYY'-'coin_pulse_areas_tXX'			
‘coin_pulse_chs’	array (N,10)	int32		-1
	First 10 individual pulse channels in the coincidence pulse.			
‘coin_pulse_ids’	array (N,10)	int32		-1
	First 10 individual pulse ids in the coincidence pulse.			
‘coin_pulse_lastpulse_areas’	array (N,C)	float32	mV ns	nan
	Pulse area of the last pulse before a coincidence pulse in each channel.			
‘coin_pulse_lastpulse_ids’	array (N,C)	int32		-1

Continued on next page

RQ name	shape	type	unit	default
	Pulse id of the last pulse before a coincidence pulse in each channel.			
'coin_pulse_lastpulse_lens'	array (N,C)	float64	ns	nan
	Pulse length of the last pulse before a coincidence pulse in each channel.			
'coin_pulse_lastpulse_times'	array (N,C)	float64	ns	nan
	Start time of the last pulse before a coincidence pulse in each channel (since LZ_EPOCH_DATETIME).			
'coin_pulse_lens'	array (N,)	float64	ns	nan
	Coincidence pulse length.			
'coin_pulse_amplitudes_' peaktime	array (N,)	float64	ns	nan
	Time difference between the start time of the coincidence pulse and normalized coincidence pulse reach maximum amplitude.			
'coin_pulse_amplitudes_' peaktime_smooth	array (N,)	float64	ns	nan
	Time difference between the start time of the coincidence pulse and smoothed normalized coincidence pulse reach maximum amplitude.			
'coin_pulse_times'	array (N,)	float64	ns	nan
	Coincidence pulse start time (since LZ_EPOCH_DATETIME).			
'coin_pulse_waveforms'	list (N,C,W)	float32	mV	0
	Waveforms of a coincidence pulse in each channel.			
'coin_pulse_waveforms_norm'	list (N,C,W)	float32		0
	Waveforms of a coincidence pulse in each channel normalize by single photo electron size.			
'coin_pulse_waveforms_sum'	list (N,W)	float32		0
	Sum of waveforms of a coincidence pulse in all channels normalize by single photo electron size.			
'coin_pulse_wtime_tXXYY'	array (N,)	float32	ns	nan
	Pulse height( $h_i$ ) weighted average of time( $t_i$ ) between 'coin_pulse_areas_tXX' and 'coin_pulse_areas_tYY'. XXYY=1585, 0595. $\bar{t} = \sum h_i t_i / \sum h_i$ .			
'coin_pulse_wtimeN_tXXYY'	array (N,)	float32	ns <sup>N</sup>	nan
	$\sum h_i (t_i - \bar{t})^N / \sum h_i$ . XXYY=1585, 0595. N=2,3,4.			
'disp'	scalar	string		

Continued on next page

RQ name	shape	type	unit	default
	Display string ‘a:va;g:vg’. (ex: ‘a:+6.5;g:-6.5.’)			
‘duration’	array (F,)	float64	s	
	Duration of a file.			
‘dv’	scalar	float32	kV	
	Voltage difference between the top grid and the bottom grid.			
‘evtnum’	scalar	int64		
	Number of all computed pulses.			
‘firstvals’	array (L,)	float32	mV	
	Value of the first sample of the pulse.			
‘hft_t1’	array (L,)	float32	ns	
	Time difference between the start time of the pulse and the pulse amplitude reach maximum.			
‘in_coin_pulse’	array (L,)	bool		false
	Whether a pulse is in a coincidence pulse.			
‘neg_area_fraction’	array (L,)	float32		nan
	Ratio of negative pulse area and the sum of positive and negative pulse area.			
‘number_of_channels’	scalar	int32		4
	Number of channels.			
‘pos_area_above_threshold’	array (L,)	float32	mV ns	
	Pulse area above a certain threshold (default: 2.5 mV).			
‘pos_len_above_threshold’	array (L,)	float32	ns	
	Pulse length above a certain threshold (default: 2.5 mV).			
‘pos_len_above_threshold_- percentile_XX’	array (L,)	float32	ns	
	Time difference between the start of coincidence pulse of XX percent of all samples above a certain threshold. XX=05,50,95.			
‘pos_len_above_threshold_- trim_end’	array (L,)	float32	ns	
	Pulse length above a certain threshold excluding the ‘suppress_last_NSamples’ period.			
‘posareas’	array (L,)	float32	mV ns	
	Pulse positive area.			
‘pos_area_pulse1’	array (L,)	float32	mV ns	
	Pulse positive area of section1, which is defined by ‘pulse1_start’ and ‘pulse1_stop’.			
‘pos_area_pulse2’	array (L,)	float32	mV ns	

Continued on next page

RQ name	shape	type	unit	default
	Pulse positive area of section1, which is defined by ‘pulse2_start’ and ‘pulse2_stop’.			
‘pos_area_p1_p2’	array (L,)	float32	mV ns	
	‘pos_area_pulse2’ - ‘pos_area_pulse1’			
‘post_baseline’	array (L,)	float32	mV	
	Pulse baseline computed from the end of the pulse.			
‘post_pulse_length’	scalar	float64	ns	1800
	Pulse length not used in the end of a waveform for coincidence pulse searching.			
‘pre_baseline’	array (L,)	float32	mV	
	Pulse baseline computed from the beginning of the pulse.			
‘pre_pulse_length’	scalar	float64	ns	0
	Pulse length not used in the beginning of a waveform for coincidence pulse searching.			
‘procid’	scalar	string		
	Process id. (ex: [12345])			
‘prompt_frac_TTns’	array (L,)	float32		
	Ratio between the pulse area of the first TT ns and the total pulse area. TT=250,500,750,1000			
‘pulse1_start’	scalar	float64	sample	0
	Start time of pulse section 1.			
‘pulse1_stop’	scalar	float64	sample	75
	Stop time of pulse section 1.			
‘pulse2_start’	scalar	float64	sample	0
	Start time of pulse section 2.			
‘pulse2_stop’	scalar	float64	sample	200
	Stop time of pulse section 2.			
‘random_pulse_areas_post_TTus’	array (M,C)	float32	phe	0
	Pulse area of TT us after a random time. TT=100,50,20,10.			
‘random_pulse_areas_pre_TTus’	array (M,C)	float32	phe	0
	Pulse area of TT us before a random time. TT=100,50,20,10.			
‘random_pulse_times’	array (M,C)	float64	ns	nan
	A random time.			
‘rmsratio’	array (L,)	float32		

Continued on next page

RQ name	shape	type	unit	default
	Ratio between Root mean square (rms) of the waveform and the waveform amplitude.			
'sample_size'	scalar	float64	ns	4
	Sample size of a waveform.			
'skimfactor'	scalar	int64		1
	Ratio between the number of all computed pulses and the number of all recorded pulses.			
'sphe_size'	array (C,)	float64	mV ns	inf
	Pulse area of a single photo electron in each channel.			
'suppress_last_NSamples'	scalar	int32		450
	Number of samples not recorded in the end of a waveform.			
'times'	array (L,)	float64	ns	
	Pulse start time (since LZ_EPOCH_DATETIME).			
'trigvals'	array (L,)	float32	mV	nan
	Pulse trigger voltage.			
'usechannels'	array	int32		[0,2]
	Active channels.			
'va'	scalar	float32	kV	
	Voltage of the top grid.			
'vg'	scalar	float32	kV	
	Voltage of the bottom grid.			
'waveamplitudes'	array (L,)	float32	mV	
	Pulse amplitude.			
'waveareas'	array (L,)	float32	mV ns	
	Pulse area.			
'waveareas_trim_end'	array (L,)	float32	mV ns	nan
	Pulse area suppressing last 'suppress_last_NSamples' samples to 0.			
'waveforms'	list (L,)	float32	mV	nan
	Waveform.			
'wavelens'	array (L,W)	float32	ns	
	Pulse length.			
'window_width'	scalar	float64	ns	1500

Continued on next page

RQ name	shape	type	unit	default
	Window size of coincidence pulse searching. It is also called coincidence window width(CWW).			
'wtime'	array (L,)	float32	ns	nan
	Pulse height( $h_i$ ) weighted average of time( $t_i$ ). $\bar{t} = \sum h_i t_i / \sum h_i$ .			
'wtimeN'	array (L,)	float32	ns <sup>N</sup>	nan
	$\sum h_i (t_i - \bar{t})^N / \sum h_i$ . N=2,3,4.			
<p>L: number of all computed pulses.      N: number of coincidence pulses.      M: number of random pulses.      C: number of channels.      W: number of samples in a waveform.      F: number of files in a dataset.      LZ_EPOCH_DATETIME: 2015, Jan, 1st, 00 : 00 : 00.      phe: average photo electron area.</p>				

Table A.1: Gas Test RQ documentation

<sup>1489</sup> **Appendix B**

<sup>1490</sup> **Abbreviations**

<sup>1491</sup> This chapter summarizes the abbreviations that occur in this thesis.

<sup>1492</sup> #: the counts of

<sup>1493</sup> ~: approximately

<sup>1494</sup> ADC: Analog-to-Digital Converter

<sup>1495</sup> avg.: average

<sup>1496</sup> BBN: Big Bang Nucleosynthesis

<sup>1497</sup> CCD: Charge-couple device

<sup>1498</sup> CDF: Cumulative Distribution Function

<sup>1499</sup> CMB: Cosmic Microwave Background

<sup>1500</sup> config.: configuration

<sup>1501</sup> cont.: continued

<sup>1502</sup> CSDA range: Continuous Slowing Down Approximation range

<sup>1503</sup> CWW: Coincidence Window Width

<sup>1504</sup> CV: Coefficient of Variation

<sup>1505</sup> DAQ: Data AcQuisition

<sup>1506</sup> DM: Dark Matter

<sup>1507</sup> dur.: duration

<sup>1508</sup> EL: ElectroLuminescence

<sup>1509</sup> ELD: ElectroLuminescence Detector

<sup>1510</sup> ER: Electron Recoil (event)

<sup>1511</sup> LUX: Large Underground Xenon experiment

<sup>1512</sup> LZ: LUX-ZEPLIN experiment

<sup>1513</sup> max.: maximum

<sup>1514</sup> min.: minimum

<sup>1515</sup> MFC: Mass Flow Controller

- 1516 NR: Nuclear Recoil (event)  
1517 PDE: Photon detection efficiency (also called light collection efficiency)  
1518 PDF: Probability Distribution Function  
1519 PMF: Probability Mass Function  
1520 PEEK: PolyEther Ether Ketone  
1521 PHD(phd): counts of PHotoelectrons Detected  
1522 PHE(phe): SPHE pulse area or counts of (single) PHotoElectrons. In other literatures, it is  
1523 sometime called PE(pe).  
1524 PMT: Photomultiplier Tube  
1525 PPB(ppb): parts per billion atoms/molecules  
1526 PTFE: PolyteTraFluoroEthylene  
1527 R&D: Research and Development  
1528 refl.: reflectivity  
1529 RQ: Reduce Quantity of a pulse  
1530 S1: primary Scintillation light  
1531 S2: secondary Scintillation light  
1532 S, SF: Survival Function  
1533 SS: Stainless Steel  
1534 QE: Quantum Efficiency (of a PMT)  
1535 QF: Quiet Fraction  
1536 SLAC: SLAC national accelerator laboratory  
1537 TBA: Top-Bottom Asymmetry  
1538 TPC: Time Projection Chamber (detector)  
1539 vs.: versus  
1540 WIMP: Weak Interaction Massive Particle  
1541 XML: eXtensible Markup Language  
1542  $\Lambda$ CDM: Lambda Cold Dark Matter

1543    

# Bibliography

- 1544 [1] Hamamatsu Photonics, *Photomultiplier Tubes*, (2006) [http://www.hamamatsu.com/resources/pdf/etd/PMT\\_handbook\\_v3aE.pdf](http://www.hamamatsu.com/resources/pdf/etd/PMT_handbook_v3aE.pdf).
- 1545
- 1546 [2] SAES, *PS3-MT3-R/N SPECIFICATIONS*, (2002) [http://www.saespuregas.com/Library/documents/ps3spec\\_512.pdf](http://www.saespuregas.com/Library/documents/ps3spec_512.pdf).
- 1547
- 1548 [3] KNF Neuberger Incorporated Companies, *Diaphragm-Gas Sampling Pumps with double diaphragm System*, <https://www.knfsusa.com/products/oem-products/product/products/diaphragm-gas-pumps-and-compressors/double-diaphragm-pumps/>.
- 1549
- 1550
- 1551 [4] Alicat Scientific, *Operating Manual - MFCs*, [http://www.alicat.com/documents/manuals/Gas\\_Flow\\_Controller\\_Manual.pdf](http://www.alicat.com/documents/manuals/Gas_Flow_Controller_Manual.pdf).
- 1552
- 1553 [5] T Shutt, *Light guide software for photon propagation (unpublished)*, (2018)
- 1554 [6] C. Silva, “Study of the reflectance distributions of fluoropolymers and other rough surfaces with interest to scintillation detectors”, (2009).
- 1555
- 1556 [7] B. Feuerbacher and B. Fitton, “Experimental Investigation of Photoemission from Satellite Surface Materials”, *Journal of Applied Physics* **43**, 1563 (1972).
- 1557
- 1558 [8] J. W. Keto, R. E. Gleason, and G. K. Walters, “Production Mechanisms and Radiative Lifetimes of Argon and Xenon Molecules Emitting in the Ultraviolet”, *Physical Review Letters* **33**, 1365 (1974).
- 1559
- 1560
- 1561 [9] A. Hitachi et al., “Effect of ionization density on the time dependence of luminescence from liquid argon and xenon”, *Physical Review B* **27**, 5279 (1983).
- 1562
- 1563 [10] C. M. B. Monteiro et al., “Secondary scintillation yield in pure xenon”, *Journal of Instrumentation* **2**, P05001 (2007).
- 1564
- 1565 [11] V. Chepel and H. Araújo, “Liquid noble gas detectors for low energy particle physics”, *Journal of Instrumentation* **8**, R04001 (2013).
- 1566
- 1567 [12] J. C. Bowe, “Drift velocity of electrons in nitrogen, helium, neon, argon, krypton, and xenon”, *Phys. Rev.* **117** (1960).
- 1568

- 1569 [13] C. Geuzaine and J.-F. Remacle, “Gmsh: A 3-D finite element mesh generator with built-in pre-  
1570 and post-processing facilities”, *International Journal for Numerical Methods in Engineering*  
1571 **79**, 1309 (2009).
- 1572 [14] CSC – Scientific Computing Ltd., *ELMER–a finite element solver for multiphysics*, (1999)  
1573 <https://www.csc.fi/web/elmer>.
- 1574 [15] S. Kotila and J. Haataja, “CSC Report on Scientific Computing 1999–2000”, CSC – Scientific  
1575 Computing Ltd., Finland (1999).
- 1576 [16] S. Biagi, “Monte Carlo simulation of electron drift and diffusion in counting gases under  
1577 the influence of electric and magnetic fields”, *Nuclear Instruments and Methods in Physics*  
1578 *Research Section A: Accelerators, Spectrometers, Detectors and Associated Equipment* **421**,  
1579 234 (1999).
- 1580 [17] R. Veenhof, “Garfield, recent developments”, *Nuclear Instruments and Methods in Physics*  
1581 *Research Section A: Accelerators, Spectrometers, Detectors and Associated Equipment* **419**,  
1582 726 (1998).
- 1583 [18] W. Blum, W. Riegler, and L. Rolandi, *Particle Detection with Drift Chambers* (Springer, 2008),  
1584 p. 448.
- 1585 [19] COMSOL Inc., *COMSOL Multiphysics Reference Manual, version 5.3*, (2018) <https://www.comsol.com/>.
- 1587 [20] US Environmental Protection Agency, “EPA Assessment of Risks from Radon in Homes”,  
1588 (2017).
- 1589 [21] D. E. Groom, N. V. Mokhov, and S. I. Striganov, “MUON STOPPING POWER AND RANGE  
1590 TABLES 10 MeV–100 TeV”, *Atomic Data and Nuclear Data Tables* **78**, 183 (2001).
- 1591 [22] S. J. C. do Carmo et al., “Absolute primary scintillation yield of gaseous xenon under low drift  
1592 electric fields for 5.9 keV X-rays”, *Journal of Instrumentation* **3**, P07004 (2008).
- 1593 [23] L. M. P. Fernandes et al., “Primary and secondary scintillation measurements in a Xenon Gas  
1594 Proportional Scintillation Counter”, *Journal of Instrumentation* **5**, P09006 (2010).
- 1595 [24] U Fano, “Penetration of Protons, Alpha Particles, and Mesons”, *Annual Review of Nuclear  
1596 Science* **13**, 1 (1963).
- 1597 [25] S. P. Ahlen, “Theoretical and experimental aspects of the energy loss of relativistic heavily  
1598 ionizing particles”, *Reviews of Modern Physics* **52**, 121 (1980).
- 1599 [26] V. Álvarez et al., “Initial results of NEXT-DEMO, a large-scale prototype of the NEXT-100  
1600 experiment”, *Journal of Instrumentation* **8**, P04002 (2013).
- 1601 [27] P. Sorensen and K. Kamdin, “Two distinct components of the delayed single electron noise in  
1602 liquid xenon emission detectors”, *Journal of Instrumentation* **13**, P02032 (2018).

- <sup>1603</sup> [28] A.~Kramida, Yu.~Ralchenko, and J.~Reader, *No Title*, (2018)